University of Miskolc

Faculty of Mechanical Engineering
Institute of Energy Engineering and Chemical Machinery
Department of Fluid and Heat Engineering

Vortex-induced vibrations at low Reynolds numbers

Dániel Dorogi

PhD Dissertation

István Sályi Doctoral School
Main Topic Group: Fundamental Sciences in Mechanical Engineering
Topic Group: Transport Processes and Machines

Head of Doctoral School:
Gabriella Vadászné Bognár
Doctor of Science, Full Professor

Head of Main Topic Group:
István Páczelt
Member of the Hungarian Academy of Sciences, Professor Emeritus

Head of the Topic Group:
Tibor Czibere
Member of the Hungarian Academy of Sciences, Professor Emeritus

Scientific Supervisor:
László Baranyi
Dr. habil, Full Professor

Miskolc
2020

Acknowledgments

This dissertation summarizes the results of my PhD research work carried out at the Institute of Energy Engineering and Chemical Machinery, University of Miskolc. The topic of my dissertation links directly to Prof. László Baranyi's research field, who deals with the numerical investigation of the flow around a circular cylinder undergoing forced vibrations. First of all, I would like to express my deep gratitude to my supervisor Prof. László Baranyi whose guidance, support and encouragement has been invaluable throughout this study. In the past few years I could gain from him a lot of special knowledge regarding for example to Computational Fluid Dynamics, Fluid-Structure Interaction or academic writing for which I am very grateful.

During my PhD studies I have had the chance to participate in joint researches with Dr. Efstathios Konstantinidis. I would like to thank Dr. Konstantinidis for the exciting discussions on the physical aspects of vortex-induced vibration problems. I very much appreciate the useful knowledge in analytical modeling, and also for the guidance in figure preparation or signal processing.

I would like to offer my special thanks to Robin Nagano Lee whose professional guidelines helped me a lot to obtain important knowledge in academic writing. I am very grateful for her reviewing efforts which allowed us to publish articles in leading journals.

I wish to express my sincere thanks to Dr. Péter Bencs, Director of the Institute, Institute of Energy Engineering and Chemical Machinery, for the technical support, and for permitting me to carry out this research work.

I would also like to thank all my colleagues at the Institute of Energy Engineering and Chemical Machinery for their cooperation during my scientific work.

Last but not the least, I would like to thank my parents, all my family members and friends, who have supported me throughout my PhD studies.

This research was supported by the European Union and the Hungarian State, co-financed by the European Regional Development Fund in the framework of the GINOP-2.3.4-15-2016-00004 project, aimed to promote the cooperation between the higher education and the industry.

Last updated: April 20, 2020

Abstract

Fluid flow around bluff bodies have been thoroughly investigated in the past few decades due to their high engineering importance. This phenomenon plays an important role for example in offshore risers, high slender buildings, chimney stacks, heat exchangers, etc. The vortices shedding from the bluff body superimpose a periodic load on the structure, which can cause high-amplitude oscillations. This effect is referred to as *vortex-induced vibrations* (VIV).

In this PhD dissertation the vortex-induced vibration of a circular cylinder is investigated by means of two-dimensional CFD computations at low Reynolds numbers. The governing equations of the fluid and solid motions are solved using an in-house code based on the finite difference method. Some details of the CFD approach are provided in Chapter 2. After the independence studies, a step-by-step validation is carried out to compare the currently obtained results against the literature data (see Chapter 3). Good agreement was found for all test cases.

In Chapter 4 two-degree-of-freedom vortex-induced vibrations are investigated at different nondimensional natural frequency values K. It was found that plotting the data set belonging to different K values against $U^*\mathrm{St}$ makes comparison easier than using the Reynolds number as an independent parameter. Here U^* is the reduced velocity and St is the Strouhal number for a stationary cylinder. For the dimensionless natural frequency values between $K \cong 12.3$ and 34.7, the root-mean-square (rms) values of the streamwise vibration component and fluid force coefficient $x_{0'}$ and $C_{x'}$ display local peak values at $U^*\mathrm{St} \cong 0.47$. In addition, at around $U^*\mathrm{St} = 0.5$ $C_{x'}$ approaches zero, at the same point where the phase difference of the streamwise fluid force relative to the x component of the motion changes abruptly from 0° to 180°. The pressure component of the streamwise fluid force coefficient seems to be responsible for the sudden change.

The results from the two-degree-of-freedom VIV computations at distinct K values reveal also that the non-dimensional natural frequency influences significantly the cylinder path. For the values of $K < 36.6$ only distorted figure-eight motions are found. However, in the range of $K \cong 36.6$–43.7 orbital trajectories (i.e. the raindrop-shaped paths) occur in a thin $U^*\mathrm{St}$ domain, which extends with K. For orbital paths two high-intensity peaks are observed in the frequency spectra of the x vibration component. Due to the multi-frequency vibration, the raindrop-shaped trajectory is asymmetric. P+S vortex structures are identified for these paths, which confirms the asymmetrical nature of the orbit. The time-mean values of the transverse fluid force jump abruptly between two solutions. The pre- and post-jump analysis reveals that these solutions are mirror images of each other.

In Chapter 5 single-degree-of-freedom VIV computations are carried out, where the cylinder is allowed to move only streamwise with the free stream. The investigations at various Reynolds numbers (Re $= 100, 180$ and 250), and different mass ratio values ($m^* = 2, 5, 10$ and 20) show that streamwise-only vortex-induced vibrations are possible at low Reynolds numbers. A single excitation region is identified, which corresponds to the second response branch reported in the literature for moderately high Re. The dimensionless vibration amplitude $\hat{x}_0$ plotted against U^* for one particular combination of Re and m^* increases up to its peak value, then it decreases. The non-dimensional vibration frequency f_x^* behaves oppositely. Although the peak value of $\hat{x}_0$ appears to be independent of m^*, varying the Reynolds number the maximum vibration amplitude shows a significant increase. It was also shown that the magnitude of the streamwise fluid force coefficient approaches zero at the point, where the vibration frequency coincides with the cylinder's natural frequency. Since the amplitude of cylinder oscillation is non-zero at this point, the streamwise fluid force has strongly non-harmonic nature. Unlike the phase angle between C_x and x_0, which is restricted to the values of $0°$ and $180°$, the phase difference of the transverse fluid force relative to the cylinder displacement increases gradually with U^*. This effect is attributed to the switch in the timing of vortex shedding.

Finally, in Chapter 6 transverse-only vortex-induced vibrations are investigated at the Reynolds number and mass ratio values of Re = 300 and $m^* = 10$, respectively, for different structural damping ratios between $\zeta = 0\%$ and 5%. Up until now, researchers have reported an upper branch only at high Reynolds numbers and low $m^*\zeta$ values. However, in this study we have observed three-branch behavior (initial, upper and lower branches) at Re = 300 for $\zeta \leq 1\%$. The upper branch is bounded by two gradual phase changes: at the boundary adjacent to the initial branch, the time-averaged phase difference of the vortex force, and at that to the lower branch, the time-averaged phase difference of the transverse fluid force relative to the cylinder displacement changes between $0°$ and $180°$. Unbounded variations and phase slips are observed in the time-dependent phase differences, which explains the gradual changes in their time-mean values. In the upper branch $2P_O$ and P+S modes, while in the initial and lower branches 2S vortex structures are identified. The second harmonic frequency component plays an important role in the spectra of transverse fluid force, which is closely related to the observed P+S vortex structure. Increasing the structural damping over $\zeta = 1\%$, only initial and lower branches are found.

Kivonat

A tompa testek körüli áramlási folyamatok vizsgálatával – a téma nagy mérnöki fontossága miatt – számos tanulmány foglalkozik. A jelenség fontos szerepet játszik például a szélterhelésnek kitett karcsú épületeknél, a vízfelszín alatti vezetékeknél vagy a hőcserélőknél. Ismeretes, hogy a tompa testekről leváló örvények periódikus terhelést jelentenek a szerkezetre nézve, amelynek következtében a test nagyamplitúdójú rezgőmozgásba jöhet. E jelenséget angol nyelven „vortex-induced vibration"-nek nevezik.

A jelen PhD disszertáció egy párhuzamos áramlásba helyezett, szabadrezgésre képes (rugalmasan felfüggesztett) körhenger körüli áramlási folyamatok kétdimenziós numerikus áramlástani vizsgálatával foglalkozik. A folyadékáramlást és a henger mozgását leíró egyenleteket egy a tanszéken kifejlesztett számítógépes programkód segítségével oldom meg, amely a véges differenciák módszerét alkalmazza. A számítási eljárás részleteit a 2. fejezetben ismertetem. Ezt követően függetlenségi vizsgálatokat végzek, majd az eredményeket összehasonlítom az irodalomban rendelkezésre álló adatokkal (lásd 3. fejezet).

A dolgozat 4. fejezetében az örvényleválás által gerjesztett kétszabadságfokú rezgőmozgásokat vizsgálom különböző K dimenziótlan sajátfrekvenciák esetén. Azt tapasztaltam, hogy az $U^*\mathrm{St}$ paramétert használva független változóként – ahol U^* a redukált sebesség és St a Strouhal-szám –, a különböző K értékek esetén számított görbék egy viszonylag szűk tartományba hozhatók, amely nagymértékben javította az adatsorok összehasonlíthatóságát. A hosszirányú rezgéskomponens és erőtényező rms értéke ($x_{0'}$ és $C_{x'}$) az $U^*\mathrm{St} \cong 0{,}47$ értéknél lokális maximumot mutat, illetve $C_{x'}$ az $U^*\mathrm{St} \cong 0{,}5$ helyen zérushoz tart. A C_x és x_0 időfüggvényeinek segítségével kimutattam, hogy $U^*\mathrm{St} < 0{,}5$ esetén a két jel fázisban van. Az $U^*\mathrm{St} \cong 0{,}5$ elérésekor x_0 és C_x hirtelen ellenfázisba kerül, amely az $U^*\mathrm{St} > 0{,}5$ tartományban fennáll. A számításokból arra következtettem, hogy $C_{x'}$ zérussá válását, illetve az x_0 és C_x közti hirtelen fázisugrást a hosszirányú erőtényező nyomásból származó komponense okozza.

Számítási eredményeim azt mutatják, hogy a dimenziótlan sajátfrekvencia növelése jelentős hatással van a henger pályagörbéjére. Megállapítottam, hogy míg $K < 36{,}6$ esetén a henger minden esetben torzított nyolcas alakú görbét ír le, addig a $K \cong 36{,}6$–$43{,}7$ intervallumon belül, keskeny $U^*\mathrm{St}$ tartományban esőcsepp alakú orbitális mozgásgörbe is jelentkezik. Bebizonyítottam, hogy K értékének növelésével az orbitális pálya $U^*\mathrm{St}$ tartománya kiszélesedik. Tapasztalataim alapján elmondható, hogy az esőcsepp alakú pályagörbe aszimmetrikus viselkedést mutat, amelyet az x irányú rezgéskomponens frekvenciaspektrumában megjelenő két jelentős intenzitású frekvenciacsúcs okozza. A pályagörbe aszimmetrikus voltát alátámasztja, hogy a henger mögött P+S típusú örvényszerkezet jelenik meg. A felhajtóerő-tényező $\overline{C}_y$ időátlaga (abszolút értékben) nagymértékben megnő orbitális hengermozgás esetén; továbbá $\overline{C}_y$ két megoldás között ugrásszerűen változik. A határciklusokat $[(C_x, C_y)$ vagy $(x_0, y_0)]$ egy ugrás két oldalán ábrázolva azt tapasztaltam, hogy a görbék egymásnak tükörképei. Ebből az következik, hogy $\overline{C}_y$ két megoldása szimmetrikus.

Az 5. fejezetben egyszabadságfokú hosszirányú szabadrezgés numerikus vizsgálatával foglalkozok különböző Reynolds-számok ($\mathrm{Re} = 100, 180$ és 250) és tömegarányok ($m^* = 2, 5, 10$ és 20) esetén. Számítási eredményeim azt mutatják, hogy a hosszirányú szabadrezgés létrejötte lehetséges kis Reynolds-számok esetén. Egyágú rezgésképet azo-

nosítottam, amely megfelel a szakirodalomban a közepesen nagy Re esetén bemutatott második ággal, mivel minden egyes paraméterkombinációnál (Re, U^*, m^*) alternáló örvényleválást figyeltem meg. Az $\hat{x}_0$ dimenziótlan rezgési amplitúdó a redukált sebesség függvényében, csúcsértékének eléréséig növekvő-, majd azt követően csökkenő tendenciát mutat. Ezzel szemben az f_x^* dimenziótlan rezgési frekvencia ellentétes viselkedést mutat: f_x^* változásában, kezdetben csökkenő, a minimum érték elérése utána pedig növekvő jelleg figyelhető meg. Az utóbbi két megállapítás minden vizsgált Re és m^* érték esetén igaznak bizonyult. Számítások segítségével bebizonyítottam, hogy $\hat{x}_0$ csúcsértéke független a tömegaránytól, azonban a Reynolds-szám változására érzékeny: Re növelésével $\hat{x}_0$ maximális értéke növekvő tendenciát mutat. Megállapítottam, hogy a hosszirányú erőtényező amplitúdója zérushoz tart ott, ahol a rezgési frekvenciája megegyezik a henger sajátfrekvenciájával. A rezgési amplitúdó nemzérus ebben a pontban, amely megfigyelés megmagyarázza a C_x frekvenciaspektrumában a magasabb rendű (második) felharmonikus megjelenését. Számítási eredményeim továbbá azt mutatják, hogy a C_x és x_0 közti fázisszög $\Phi_x = 0°$-ról $180°$-ra ugrásszerűen változik abban a pontban, ahol a rezgési frekvencia közel azonos a rendszer sajátfrekvenciájával. Ezzel szemben a C_y és x_0 közti fázisszög monoton növekedést mutat, amely az örvényleválás időzítésének eltolódásával van szoros összefüggésben.

Végezetül, a dolgozat 6. fejezetében a keresztirányú rezgőmozgásból származó eredményeimet ismertetem. Kimutattam, hogy az eddig kizárólag nagy Reynolds-számú áramlások, illetve kis tömegű és csillapítási tényezőjű rezgőrendszerek esetén azonosított háromágú rezgéskép (az alap-, felső- és alsóág együttese) kis Reynolds-számok és csillapítási tényezők ($\mathrm{Re} = 300$ és $\zeta \leq 1\%$) esetén is megjelenik. A felsőágat két fokozatos fázisváltozás határolja: az alapággal szomszédos határon az örvényerőnek-, valamint az alsóággal szomszédos határvonalon a keresztirányú erőtényezőnek a henger elmozdulásához viszonyított időátlagolt fázisszöge változik $0°$ és $180°$ között. A fokozatos változást az időben változó fázisszögekben észlelt határ nélküli növekedések és fáziscsúszások okozzák. A felsőágon $2\mathrm{P_O}$ és P+S, valamint az alap és alsóágakon 2S típusú örvényszerkezetet találtam. A rezgési frekvencia második felharmonikusa jelentős szerepet játszik a keresztirányú erőtényező frekvenciaspektrumában, amely összefüggésbe hozható a P+S örvényszerkezet megjelenésével. A dimenziótlan csillapítási tényezőt $\zeta = 1\%$ felett változtatva kétágú rezgéskép jelenik meg; ebben a tartományban a felsőág eltűnik a rezgésképből.

Recommendation of the supervisor

This dissertation deals with an area of flow-induced vibration (FIV). When a bluff body is placed in a uniform stream, vortices are shed periodically from the body. This periodic vortex shedding induces periodic forces on the body that can lead to large amplitude vibrations, especially when the vortex shedding frequency is near to the eigenfrequency of the system and the structural damping is small. This led to the collapse of the Tacoma Narrows Bridge and to the shutdown of the Monju fast-breeder nuclear power plant in Japan. FIV-related problems can occur with tall, slender buildings or bridges in the wind or in underwater structures, or can cause noisy operation of heat exchangers. This is the background of Dániel Dorogi's research.

Some of the research questions of his dissertation are as follows. (1) What are the effects of the dimensionless natural frequency of an elastically-supported system on cylinder vibration for two-degree-of-freedom (2DoF) cylinder vibration? (2) How does the asymmetric vortex structure influence the cylinder path? (3) Can streamwise-only (1DoF) vortex-induced vibration (VIV) occur at low Reynolds numbers? (4) What are the effects of Reynolds number and mass ratio on the cylinder response? (5) Can three-branch cylinder response occur for transverse-only (1DoF) VIV at low Reynolds numbers? (6) What is the effect of structural damping on the cylinder response for transverse-only VIV?

These research questions are the focus of the very careful literature survey and systematic numerical investigations carried out by Dániel. He extended the code I had developed for forced cylinder vibration. He paid special attention to carrying out independence studies to determine the optimal computational parameters, and to validating his results against data available in the literature. He has carried out a great deal of systematic computations in order to address his research questions. I find this dissertation to be well-structured, logically built and carefully written. It clearly presents the questions, answers them directly, and discusses his findings using results from the literature. High-quality figures help the reader to comprehend data that can be quite complex. The discussion of the effect of different parameters on the flow, the cylinder response and force coefficients is well done and is based on mathematical and physical reasoning.

Dániel has worked hard throughout his studies on writing up his results for publication. At this point, three journal articles based upon his dissertation topic have been published, two of which were published in prestigious international journals (both ranked in the top 10% of all journals related to the field and assessed in the Scimago system (D1 journals)). In addition, he has presented his work and published conference papers in several conferences, including specialized conferences abroad. He has recently submitted two more manuscripts to D1 journals that are under review at present.

Dániel's skills and attributes serve him well in academia. He is hard-working, precise, and keeps himself up to date, regularly monitoring the newest results related to his field. He is capable of setting goals for himself and identifying gaps in the research. He is a professional MATLAB user and is proficient in developing codes in FORTRAN. He takes his teaching duties seriously; he is a dedicated teacher with a talent for explanation and his presentation skills are well above average. He has been involved in joint research (even internationally) and has worked within several projects, as well. This dissertation is proof that Dániel Dorogi is a talented researcher who is capable of carrying out high level research independently.

Miskolc, April 20, 2020

László Baranyi
Professor

Contents

Declaration

I, the undersigned **Dániel Dorogi** aware of my criminal responsibility hereby declare that the submitted PhD dissertation is the result of my own work, the literary references are clear and complete.

Miskolc, April 20, 2020

Dániel Dorogi
PhD candidate

Nomenclature

Roman Symbols

b	structural damping [kg s^{-1}]
C_A	added mass coefficient [–]
C_x	streamwise fluid force coefficient, $2\tilde{F}_x/(\rho U_\infty^2 d)$ [–]
C_{xp}	pressure streamwise fluid force coefficient [–]
C_{xv}	viscous streamwise fluid force coefficient [–]
C_y	transverse fluid force coefficient, $2\tilde{F}_y/(\rho U_\infty^2 d)$ [–]
C_{yp}	pressure transverse fluid force coefficient [–]
C_{yv}	viscous transverse fluid force coefficient [–]
C_V	vortex force coefficient, $2\tilde{F}_V/(\rho U_\infty^2 d)$ [–]
D	dilation, non-dimensionalized by U_∞/d
d	cylinder diameter, length scale [m]
$\tilde{F}_p$	potential added mass force per unit length of the cylinder [N m^{-1}]
$\tilde{F}_x$	streamwise fluid force per unit length of the cylinder [N m^{-1}]
$\tilde{F}_y$	transverse fluid force per unit length of the cylinder [N m^{-1}]
$\tilde{F}_V$	vortex force per unit length of the cylinder [N m^{-1}]
f_N	cylinder's natural frequency in vacuum, $1/(2\pi)\sqrt{k/m}$ [s^{-1}]
$f_{N,a}$	cylinder's natural frequency in still fluid, $1/(2\pi)\sqrt{k/(m+m_A)}$ [s^{-1}]
f_v	vortex shedding frequency for a stationary cylinder [s^{-1}]
f_x^*, f_y^*	vibration frequencies in x and y directions, non-dimensionalized by U_∞/d
$f_{C_y}^*$	frequency of transverse fluid force, non-dimensionalized by U_∞/d
$f_{C_V}^*$	frequency of vortex force, non-dimensionalized by U_∞/d
K	nondimensional natural frequency, $f_N d^2/\nu$ [–]
k	spring constant [kg s^{-2}]
m	cylinder mass per unit length [kg m^{-1}]
m_A	added mass of fluid per unit length of the cylinder, $C_A \rho d^2 \pi/4$ [kg m^{-1}]
m^*	mass ratio, $m^* = 4m/(d^2\pi\rho)$ [–]

p	pressure, non-dimensionalized by ρU_∞^2
R	radius, non-dimensionalized by d
Re	Reynolds number, $U_\infty d/\nu$ [–]
St	dimensionless vortex shedding frequency for a stationary cylinder, Strouhal number, $f_v d/U_\infty$ [–]
t	time, non-dimensionalized by d/U_∞
U^*	reduced velocity based on the cylinder's natural frequency in vacuum, $U_\infty/(f_N d)$ [–]
U_A^*	reduced velocity based on the cylinder's natural frequency in still fluid, $U_\infty/(f_{N,a} d)$ [–]
U_∞	free stream velocity, velocity scale [m s^{-1}]
u, v	velocity components in x and y directions, non-dimensionalized by U_∞
x, y	Cartesian coordinates, non-dimensionalized by d
x_0, y_0	cylinder displacements in x and y directions, non-dimensionalized by d

Greek Symbols

ζ	structural damping ratio, $b/(2\sqrt{km})$ [–]
ν	kinematic viscosity of the fluid [m^2 s^{-1}]
ξ_{max}, η_{max}	number of grid points in peripheral and radial direction, respectively [–]
ρ	fluid density [kg m^{-3}]
$\varPhi_x$	phase difference of C_x relative to the displacement [–]
$\varPhi_y$	phase difference of C_y relative to the displacement [–]
$\varPhi_V$	phase difference of C_V relative to the displacement [–]
φ_{xp}	phase difference of C_{xp} relative to the displacement [–]
φ_{xv}	phase difference of C_{xv} relative to the displacement [–]

Subscripts and superscripts

max	peak value
n	component in the direction normal to the cylinder surface
pot	potential flow
x	streamwise
y	transverse
$1, 2$	on the cylinder surface, at the outer boundary of the domain, respectively
0	cylinder response

Abbreviations

C	refers to the coalescence of the positive and negative vortices in the cylinder wake

CFD	Computational Fluid Dynamics
DoF	Degree of Freedom
PSD	Power Spectral Density
P	refers to vortex pair shedding from the cylinder in each motion cycle
S	refers to single vortex shedding from the cylinder in each motion cycle
VIV	Vortex-Induced Vibration

Chapter 1

Introduction

In this chapter, first a selective literature review is given, which links directly to the present dissertation (Section 1.1). Since there are numerous experimental and computational studies in the field of flow around an oscillating cylinder, a comprehensive review is not possible due to the space limits. My aim is to create the body of knowledge, which is essential for the correct understanding of the present objectives and the discussion of the results. The literature survey covers

(a) the fluid flow around a stationary circular cylinder (Section 1.1.1);

(b) the flow around a cylinder undergoing forced/controlled oscillations (Section 1.1.2);

(c) the most important results concerning the single-degree-of-freedom vortex-induced vibrations (VIV), where the body is restricted to move only in transverse[1] or streamwise[2] direction (Sections 1.1.3 and 1.1.4) and

(d) some results on two-degree-of-freedom VIV, where the cylinder is allowed to move in the two directions (Section 1.1.5).

From the literature review I address research questions, which determine the objectives of this PhD dissertation. The research questions with the objectives are presented in Section 1.2.

1.1 Literature review

Fluid flow around a circular cylinder exposed to wind or wave is widely investigated due to its practical importance. It plays a significant role for example in offshore risers, chimney stacks, towers, bridge piles and heat exchangers. The periodic vortex shedding from the body can induce high amplitude oscillations, which can cause serious damage to the structure. This phenomenon played an important role in the collapse of the Tacoma Narrows Bridge in 1940. Damage to the thermometer cases at the Monju fast-breeder nuclear power plant in 1995 leading to a major shutdown of the entire facility was also due to periodic vortex shedding (Nishihara et al. [1]). However, mechanical energy transferred between the fluid and the moving body can also be beneficial. Possibilities of energy harvesting have been studied for example by Bernitsas et al. [2, 3] and Mehmood et al. [4].

[1] Direction perpendicular to the free stream. The phrase *cross-flow* is also used with the same meaning.
[2] Direction parallel with the free stream. The phrase *inline* is also used with the same meaning.

1.1.1 Flow around a stationary circular cylinder

The origin of this research field can be dated back to the late 19^{th} century, to the experiments of Vincenc Strouhal. His study published in 1878 [5] was the first pioneering study in which the vortex shedding frequency f_v measured in the wake of a circular cylinder was presented. The non-dimensional vortex shedding frequency, the well-known Strouhal number which was named after him, is defined as

$$\mathrm{St} = \frac{f_v d}{U_\infty}, \tag{1.1}$$

where d is the cylinder diameter, and U_∞ is the free stream velocity. Since then, several studies focused on describing the Strouhal number as function of the Reynolds number

$$\mathrm{Re} = \frac{U_\infty d}{\nu}, \tag{1.2}$$

where ν is the kinematic viscosity of the fluid. Rayleigh [6, 7] suggested to express St(Re) in terms of a Taylor's expansion as:

$$\mathrm{St} = A + \frac{B}{\mathrm{Re}} + \frac{C}{\mathrm{Re}^2} + \ldots. \tag{1.3}$$

Roshko [8] plotted $f_v d^2/\nu$ as function of the Reynolds number and fitted a linear curve on the measured data points:

$$\frac{f_v d^2}{\nu} = B + A\mathrm{Re}, \tag{1.4}$$

where A and B are the coefficients of the linear least-square fit. Taking into account that $f_v d^2/\nu$ [3] is the product of the Strouhal and Reynolds numbers, $f_v d^2/\nu = \mathrm{StRe}$, the following formula can be written:

$$\mathrm{St} = A + \frac{B}{\mathrm{Re}}. \tag{1.5}$$

Note that this expression is the truncated form of the Taylor's expansion suggested by [6] and [7] [see Eq. (1.3)]. Tritton [9] applying a quadratic least-square fit obtained the following formula:

$$\mathrm{St} = A\mathrm{Re} + B + \frac{C}{\mathrm{Re}}, \tag{1.6}$$

where A, B and C are the coefficients of the least-square fit. Williamson [10] carried out experiments at the low-Reynolds number domain ($49 < \mathrm{Re} < 250$), and computed the coefficient values arise in Eqs. (1.5) and (1.6). Note that curve-fitting was applied on the data points obtained in the range of $49 < \mathrm{Re} < 180$, because St(Re) showed a discontinuity at around $\mathrm{Re} = 180$. Williamson [10] found that the error-of-fit[4] for Eq. (1.5) is 0.0021 (when $A = 0.2175$ and $B = -5.1064$), while for Eq. (1.6) it is only 0.0005 (using $A = 1.6 \times 10^{-4}, B = 0.1816$ and $C = -3.3265$). For this reason, the three-term fit suggested by Tritton [9] was found to be more accurate than the two-term expression proposed by Roshko [8].

Williamson and Brown [11] based on the effective wake width obtained the expression as follows:

[3] Nowadays, this parameter is referred to as the Roshko number $\mathrm{Ro} = f_v d^2/\nu$.

[4] "The absolute value of the error averaged over all the data points." (see [10], p. 1075).

$$\mathrm{St} = A + \frac{B}{\sqrt{\mathrm{Re}}} + \frac{C}{\mathrm{Re}}. \tag{1.7}$$

Using the data published in [10] they obtained $A = 0.285, B = -1.3897$ and $C = 1.8061$ coefficients. The error-of-fit for this estimation is 0.0002, which is less than the values using Eqs. (1.5) and (1.6). Henderson [12] carried out Direct Numerical Simulations (DNS) in an extended Reynolds number range of Re = 47–1000. Williamson and Brown [11] tested Eq. (1.7) on the DNS results at high Re, where the flow is three-dimensional. They found that the error-of-fit is 0.0005 (when $A = 0.2731, B = -1.1129$ and $C = 0.4821$), which is comparable to that obtained in the domain of $49 < \mathrm{Re} < 180$.

Kovásznay [13] carried out time-resolved measurements using the *hot-wire anemometry*. The Reynolds number was varied from zero (corresponding to fluid at rest) up to $\mathrm{Re} \cong 10^4$. His early experimental results showed that the onset of vortex shedding (where the Kármán vortex street started to develop) occurs at $\mathrm{Re} \cong 40$. This value agrees well with the *Computational Fluid Dynamics* (CFD) results of Thompson and Le Gal [14] ($\mathrm{Re} \cong 47$), and Baranyi and Lewis [15] ($\mathrm{Re} \cong 47.2$). Kovásznay [13] showed also that the periodic vortex shedding remains stable below $\mathrm{Re} \cong 160$. This Reynolds number value compares well with $\mathrm{Re} \cong 180$, where Williamson [10] observed a three-dimensional flow structure, which resulted in a discontinuity in the St(Re) curve. Barkley and Henderson [16] using linear stability analysis found that the flow is fully two-dimensional (2D) up to $\mathrm{Re} \cong 188.5$. They identified three-dimensional instabilities at $\mathrm{Re} \cong 188.5$ and 259, which Williamson [10] named as *Mode A* and *Mode B*. Thus, the application of a 2D computational code above $\mathrm{Re} = 188.5$ is not justified for a stationary cylinder. This is the reason why 2D computations (for a stationary cylinder) are carried out only at low Reynolds numbers (mainly below $\mathrm{Re} = 200$).

Posdziech and Grundmann [17] using 2D computations investigated the low-Re regime. They analyzed the effects of grid resolution and the extension of the computational domain on the time-mean and root-mean-square values of the aerodynamic force coefficients (lift and drag), and on the Strouhal number. In addition, they created different empirical formulæ describing the relationship between the Strouhal and Reynolds numbers. Their most accurate formula can be written as follows:

$$\mathrm{St} = A + B\mathrm{Re}^{C}. \tag{1.8}$$

Using $A = 0.2844, B = -0.8706$ and $C = -0.4304$ the error-of-fit is 0.00038. Note that this expression will be applied in later sections.

The experimental studies mentioned above are frequently applied for the validation of the CFD results. Ye et al. [18] and Lai and Peskin [19] used the immersed boundary method to solve the governing equations of the fluid flow. Baranyi and Shirakashi [20] applied the finite difference method, and compared the Strouhal number and the time-mean values of the drag coefficient against experimental data. Lima E Silva et al. [21] combined the finite difference method with the virtual boundary method, and computed the flow around a circular cylinder. Bolló [22] carried out systematic computations in the range of $\mathrm{Re} < 200$ using the finite volume method. She applied the Strouhal number, and the time-mean and root-mean-square values of lift and drag coefficients for comparisons.

Another important direction of research in this field is the investigation of aerodynamic forces acting on the cylinder. For results in this area see Norberg [23] and Sumer and Fredsoe [24].

1.1.2 Forced cylinder vibrations

As mentioned in Section 1.1.1, two-dimensional computations of the flow around a stationary cylinder are limited to the Reynolds number range of $\mathrm{Re} < 188.5$, due to the occurrence of the Mode A instability [16]. For vibrating cylinders, however, the experiments by Bearman and Obasaju [25] and Koide et al. [26], and the numerical simulations by Poncet [27] showed that the synchronization between vortex shedding and cylinder motion enhances the two-dimensionality of the flow compared to the case of a stationary cylinder. The upper limit of the two-dimensionality region has not yet been determined because of the large number of influencing parameters.

As mentioned earlier, the vortices shedding from the cylinder mean periodic load on the structure. In the case when the vortex shedding frequency is close to the natural frequency of the system f_N, high amplitude vibration can occur. This phenomenon is always referred to as lock-in or synchronization. The terminology *vortex-induced vibration* (VIV)[5] is often used referring to oscillations caused by the vortex shedding. VIV is widely modeled using the forced/controlled oscillation approach, where the cylinder is oscillated mechanically. This approach is a simplifying model, and is often chosen because no equations are needed to be solved for the cylinder motion.

A large number of papers deal with forced oscillation in one-degree-of-freedom (1DoF) cylinder motion, where the body is restricted to move only in transverse direction. Williamson and Roshko [28] carried out forced vibration experiments in the range of Re = 300–1000. They created a so-called wake mode map (known as the *Williamson-Roshko map*), where they organized the different vortex structures in the amplitude-wavelength plane. It can be seen from their results that a 2P vortex structure (two pairs of vortices are shed from the cylinder in each motion cycle) plays an important role in the fundamental lock-in domain for high Reynolds numbers (Re $>$ 300). In addition, Williamson and Roshko [28] identified a P+S asymmetric mode (a vortex pair and a single vortex) only at very high vibration amplitudes ($\hat{y}_0 = 1$–2, where $\hat{y}_0$ is oscillation amplitude nondimensionalized by the cylinder diameter). They found that decreasing the Reynolds number below Re = 300, the 2P mode in the fundamental synchronization range is replaced by the P+S vortex structure. The forced vibration CFD results of Meneghini and Bearman [29] and Blackburn and Henderson [30] confirmed this finding: they did not observe the 2P mode of vortex shedding but they found the P+S vortex structure. Leontini et al. [31] carried out systematic forced vibration computations at Re $\leq$ 300. Similar to the experiments of Williamson and Roshko [28], Leontini et al. [31] investigated the effects of forcing frequency and amplitude, and created wake mode maps at Re = 100 and 300. At Re = 100 the P+S mode occurred only at very high vibration amplitudes (over $\hat{y}_0 = 0.9$) and, however, at Re = 300 they did identify the P+S vortex structure around $\hat{y}_0 = 0.55$, and near the fundamental lock-in domain.

Blackburn and Henderson [30] defined the mechanical energy transfer between the fluid and the transversely oscillating cylinder as

$$E = \int_0^T C_y \dot{y}_0 \mathrm{d}t, \tag{1.9}$$

where t is the dimensionless time, $\dot{y}_0$ is the non-dimensional velocity of the cylinder, C_y is the transverse fluid force coefficient, and T is the period of cylinder oscillation. In case $E > 0$, energy is transferred from the fluid to the cylinder, which is always the case for self-excited motions. In this sense, E is useful to localize the domains, where vortex-induced vibrations are possible to occur. Baranyi and Daróczy [32] investigated the effects of vibration amplitude and frequency, and Reynolds number on the mechanical energy transfer. They found $E > 0$ values near the boundary of the fundamental lock-in domain, when the dimensionless oscillation amplitude was below $\hat{y}_0 = 0.6$.

Nishihara et al. [1] showed that the failure of the thermometer cases at the Monju nuclear power plant was caused by vibrations streamwise with the free stream. Despite, researches on fluid flow around a circular cylinder forced to oscillate only in streamwise

[5]For synonyms of the term “vortex-induced vibration”, “self-excited motion” or “free vibration” is commonly used.

direction are much scarce than investigations concerning a transversely oscillated cylinder. The investigations carried out by Al-Mdallal et al. [33] and Mureithi et al. [34] are the most well-known studies in this field. Tanida et al. [35] carried out experiments in the range of $40 \leq \mathrm{Re} \leq 150$ at the dimensionless oscillation amplitude value of $\hat{x}_0 = 0.14$. They showed that the phase difference of streamwise fluid force relative to the cylinder displacement is negative, yielding negative mechanical energy transfer [$E < 0$, defined similarly to Eq. (1.9)]. The recent CFD studies by Konstantinidis and Bouris [36] ($\hat{x}_0 = 0.1, \mathrm{Re} = 150$) and Kim and Choi [37] ($\hat{x}_0 = 0.05, \mathrm{Re} = 100$) showed similar features to Tanida et al. [35]'s experimental results: E was negative in all the computation points. Contrary to $E > 0$, negative mechanical energy transfer indicates that self-excited vibration of the cylinder in streamwise direction is not feasible in the low-Reynolds number range. Nevertheless, the question arises whether streamwise-only vortex-induced vibration of a circular cylinder can occur for low Reynolds numbers (maybe at lower oscillation amplitudes).

In reality, the cylinder oscillates always in two directions at the same time (streamwise and transverse), which leads to two-degree-of-freedom cylinder motion. Two types of cylinder paths are observed in the free vibration experiments: (a) when the frequency of cylinder oscillation in streamwise direction is double that in transverse direction ($f_x^* = 2f_y^*$), yielding a figure-eight type path[6] [38–41], and (b) when the vibration frequencies in the two directions are identical ($f_x^* = f_y^*$), which results in orbital paths [42–44]. The experimental or numerical studies for forced figure-eight cylinder motions include Jeon and Gharib [45], Baranyi [46], and Peppa et al. [47]. Baranyi [46] found that the orientation of the path strongly influences the force coefficients and the mechanical energy transfer. When the cylinder orbit is anticlockwise on the upper loop of figure-eight, $E > 0$ over the large part of the parameter domain, in contrast with the clockwise orbit where E is mainly negative. There is relatively little research carried out for flow around a circular cylinder following orbital paths [48, 49]. Baranyi [50] showed results of numerical simulation of low-Reynolds number flow ($\mathrm{Re} = 120$–180) past a circular cylinder following an elliptical path. He systematically changed the transverse oscillation amplitude while keeping the in-line amplitude constant. When plotting the results against transverse oscillation amplitude, jumps have been found in the time-mean and root-mean-square values of the force coefficients, and in the mechanical energy transfer between the fluid and cylinder.

1.1.3 Transverse vortex-induced vibrations

Another approach to the investigation of vortex-induced vibrations (VIV) involves an elastically supported cylinder model, where the cylinder oscillates due to the fluctuating transverse and streamwise fluid forces acting on the body. A large number of studies have dealt with this model, including Bishop and Hassan [51], Bearman [52, 53], Sarpkaya [54, 55], Williamson and Govardhan [39], and Blevins [56].

Although in reality the cylinder is allowed to move in two degrees of freedom (both streamwise with and transverse to the main stream), transverse-only vibration is often used to model VIV. Feng [57], Brika and Laneville [58] and Khalak and Williamson [59] showed that the cylinder response (amplitude and frequency values) highly depends on the mass-damping parameter $m^*\zeta$. Here m^* is the mass ratio (cylinder mass divided by the mass of the displaced fluid) and ζ is the structural damping ratio:

$$m^* = \frac{4m}{\rho d^2 \pi}, \qquad \zeta = \frac{b}{2\sqrt{km}}, \tag{1.10a, b}$$

where m is the mass per unit length of the cylinder, ρ is the fluid density, and b and k are the structural damping and spring constant values, respectively. The oscillation amplitude shows higher values at distinct region, which domains are usually referred to as "response

[6] For synonym of the term "figure-eight path", "Lissajous curve" is commonly used.

branches" [39] for transverse-only VIV. Feng [57] and Brika and Laneville [58] investigated high-$m^*\zeta$ cases. Plotting the amplitude of cylinder oscillation against reduced velocity

$$U_A^* = \frac{U_\infty}{f_{N,a} d}, \tag{1.12}$$

where $f_{N,a}$ is the natural frequency of the cylinder in sill fluid, they found two response branches, namely the initial and lower branches, where the initial branch was associated with the peak oscillation amplitude. In addition, Brika and Laneville [58] showed that the transition between the initial and lower branches is hysteretic, due to the abrupt change in the vortex structure. Using the notations introduced by Williamson and Roshko [28], Brika and Laneville [58] observed a 2S mode (two single vortices are shed from the cylinder in each motion cycle) in the initial branch, while a 2P mode in the lower branch.

Khalak and Williamson [59] identified three response branches (initial, upper and lower branches) for very low mass-damping values, where the peak vibration amplitude was associated with the upper branch. They found hysteresis in the initial↔upper branch transition range, where the vortex structure switches from 2S to 2P mode. The transition between the upper and lower branches is found to be intermittent, since the wake mode does not show changes (2P mode is observed both in the upper and lower branches). Govardhan and Williamson [60] investigated also low mass-damping cases using experimental techniques. Following Lighthill [61], Govardhan and Williamson [60] decomposed the transverse fluid force into the vortex force and potential added mass force components. The phase differences for transverse fluid force and vortex force relative to the cylinder displacement $\varPhi_y$ and $\varPhi_V$ were calculated using the Hilbert transform of the corresponding signals. They showed that $\varPhi_V$ jumps between approximately $0°$ and $180°$ in the initial↔upper branch transition range, where the vortex structure switches from 2S to 2P mode. In this range the cylinder displacement remained in-phase with the transverse fluid force. However, in the transition domain between the upper and lower branches (where no significant changes were identified in the wake mode) $\varPhi_y$ was found to jump from $0°$ to $180°$, and the vortex force remained out-of-phase with the cylinder displacement.

Klamo et al. [62] investigated the effects of structural damping ratio and Reynolds number on the cylinder response. They showed that increasing ζ, the high-amplitude three-branch response switches to two-branch response, where the oscillation amplitude is significantly lower. Soti et al. [63] carried out a systematic experimental study for different ζ values. In addition to the cylinder response, they analyzed the power transfer between the oscillating cylinder and the surrounding fluid. They identified three-branch response for a wide damping ratio range; they showed the occurrence of the upper branch even at low oscillation amplitudes (down to $\hat{y}_0 = 0.2$). Bernitsas et al. [2] and Lee and Bernitsas [64] investigated the possibilities of energy harvesting from vortex-induced vibrations. Bernitsas et al. [2] based on harmonic approximations derived an analytical formula for the calculation of power transfer. Their expression shows that zero mechanical power is transferred from the fluid to the cylinder when $\varPhi_y$ (or $\varPhi_V$) equals to $0°$ or $180°$, i.e. for undamped vibrations. Their formula reveals also that increasing the structural damping ratio the power transfer can be increased, which finding agrees well with the experimental results of [63].

Klamo et al. [62] and Govardhan and Williamson [65] showed that the Reynolds number influences the cylinder response significantly. Most of the experiments are carried out in the Reynolds number range of $\mathrm{Re} = O(10^3\text{-}10^4)$. However, numerical simulations, due to the high computational time demand are usually carried out in the low-Reynolds number range [$\mathrm{Re} = O(10^2)$]. Another issue can be the three-dimensionality of the flow structure (see details in Sections 1.1.1 and 1.1.2).

The computational results available in the literature show that oscillation amplitudes for low Reynolds numbers are significantly lower (maximum $y_{0'} \cong 0.55$, see Navrose and Mittal [66]) compared to high-Re experiments (can exceed $y_{0'} \cong 0.8$, see Govardhan and Williamson [60]). Anagnostopoulos and Bearman [67] obtained similar characteristics using measurement techniques in the range of Re = 90–150. Leontini et al. [68] using CFD simulations found two-branch cylinder response at the parameter combination of Re = 200, $m^* = 10$ and $\zeta = 1\%$. The vortex structures are markedly different from those observed at high Reynolds numbers: 2S and C(2S) wake modes were found in the initial and lower branches, respectively. Here C refers to the coalescence of the positive and negative vortices in the cylinder wake. Navrose and Mittal [66] carried out numerical simulations at Re = 100 and $\zeta = 0\%$ using different mass ratios in the range of $m^* = 30$–150. They found a thin reduced velocity range in the middle of the lower branch, where the oscillation amplitude was very low and the vibration frequency did not synchronize with the cylinder's natural frequency. They also showed that the width of this low-amplitude domain extends with m^*.

In reality the Reynolds number and the reduced velocity are not independent parameters. Assuming that the natural frequency of the cylinder is constant, the following linear relationship exists between Re and U^*:

$$\mathrm{Re} = KU^*. \tag{1.13}$$

Here $U^* = U_\infty/(f_N d)$ is the reduced velocity, where f_N is the cylinder's natural frequency is vacuum, and $K = f_N d^2/\nu$ is the dimensionless natural frequency. Willden and Graham [69] investigated the effect of mass ratio between $m^* = 1$ and 50 using $K = 20$. They identified primary, secondary and tertiary responses. The primary response occurred around lock-in, where the oscillation amplitude reached its maximum value. In the secondary response (found only for $m^* > 5$) the non-dimensional vortex shedding frequency was close to the dimensionless vortex shedding frequency for a stationary cylinder, and the oscillation frequency approached the natural frequency of the body. In the tertiary response (identified only for $m^* < 10$) nearly constant vibration amplitude could be maintained. Bahmani and Akbari [70] investigated numerically the separate effects of mass and structural damping ratios for $K = 17.9$. They found that increasing m^* or ζ has almost the same effect: both the oscillation amplitude and the lock-in domain size decrease.

The numerical studies investigating vortex-induced vibrations at low Reynolds numbers have not reported an upper branch even for undamped systems [66, 68]. However, Evangelinos and Karniadakis [71] showed that the P+S vortex pattern may also be associated with the upper branch, which is rarely identified in VIV cases. Singh and Mittal [72] investigated two-degrees-of-freedom vortex-induced vibrations numerically and found P+S vortex pattern above Re = 300. As mentioned in Section 1.1.2, Leontini et al. [31] using transverse-only forced vibrations showed that the P+S vortex structure appears near the fundamental lock-in domain.

1.1.4 Streamwise vortex-induced vibrations

Besides self-excited motions transverse to the main flow, the fluctuating fluid forces can induce vibrations along the direction of the free stream, i.e. in the streamwise (or inline) direction. In the literature streamwise-only VIV received less attention, most likely because the lower amplitudes of cylinder oscillation. In the early review paper about vortex shedding and its applications, King [73] discussed some relevant results on streamwise-only vortex-induced vibrations. He showed that the maximum vibration amplitude (a peak-to-peak value) is about 0.2 times of the cylinder diameter. This value is very low compared to the transverse-only VIV cases, where the peak oscillation amplitude can easily be ten times higher.

For streamwise-only VIV cases the regions within which the vibration amplitude shows higher values are often referred to as "instability regions" [73] or "excitation regions" [74]. Note that, the terminology "response branch" is also used, but its physical meaning is different from that used in transverse-only free vibrations (see Section 1.1.3). The early experimental study carried out by King [73] and Aguirre [75] revealed that two excitation regions exist in streamwise VIV. The first branch occurs below the reduced velocity value of $U_A^* \cong 2.5$, which is associated with a symmetrical shedding of vortices simultaneously from both sides of the cylinder. The second branch occurs at $U_A^* > 2.5$, and is associated with an alternating vortex shedding mode, which type of wake mode Williamson and Roshko [28] denoted as 2S mode. These characteristics of self-excited in-line vibrations was confirmed by further experimental studies [76–78]. The value of $U_A^* \cong 2.5$ corresponds approximately to the point, where the natural frequency of the system coincides with the double of the vortex shedding frequency from a stationary cylinder; $f_{N,a} \cong 2f_v$ or $U_A^{*-1} \cong 2\mathrm{St}$ (assuming $\mathrm{St} = 0.2$). Since the Strouhal number [defined by Eq. (1.1)] is the function of the Reynolds number, especially in the low-Re regime, $U_A^* \cong 2.5$ should be replaced as $U_A^* = 1/(2\mathrm{St})$.

The effects of mass ratio m^* and structural damping coefficient ζ on the streamwise response has not yet been thoroughly investigated. Aguirre [75] concluded from his experiments that mass and damping affected the cylinder response in different ways. He noted that the mass ratio did not affect the normalized oscillation amplitude and the stiffness of the mechanical system did influence the normalized response frequency. Okajima et al. [76] in their experiments investigated the effect of "reduced mass-damping", which is proportional to the mass-damping parameter $m^*\zeta$ used in many transverse VIV cases [57–59]. Okajima et al. [76] found that as they increased the reduced mass-damping, the vibration amplitude in both excitation regions decreased. Note that this effect was due to the increasing value of structural damping, because the mass ratio was fixed in their study.

The above mentioned studies carried out experiments at moderately high Reynolds numbers, i.e. above $\mathrm{Re} = 10^3$. Tanida et al. [35], Konstantinidis and Bouris [36] and Kim and Choi [37] found that vortex-induced streamwise vibrations of a circular cylinder may not occur at low Reynolds numbers (see further discussion in Section 1.1.2). They obtained their results using the forced vibration model, and they considered constant oscillation amplitudes above $\hat{x}_0 = 0.05$. However, self-excited streamwise vibration of a circular cylinder is plausible but at lower oscillation amplitudes; at $\hat{x}_0 < 0.05$. The research question whether inline VIV is possible to occur at low Reynolds numbers has not yet been addressed. To the best knowledge of the author, the study carried out by Bourguet and Lo Jacono [79] is the solely one, where the streamwise vortex-induced vibration of a rotating cylinder is investigated at $\mathrm{Re} = 100$. The oscillation amplitude for a non-rotating cylinder is negligible compared to cases when the body was rotating.

1.1.5 Two-degree-of-freedom VIV

In most engineering applications the cylinder is allowed to move in two degrees of freedom (2DoF), both streamwise with and transverse to the main stream. In general, mass ratios (m_x^* and m_y^*) and natural frequencies (f_{Nx} and f_{Ny}) are different in the two directions. Moe and Wu [80] investigated 2DoF vortex-induced vibrations at $m_x^*/m_y^* = 2$ and $f_{Nx}/f_{Ny} = 2.18$. The vortex shedding was found to synchronize with the cylinder motion in a wide range of reduced velocity $U^* = U_\infty/(f_{Ny}d)$. However, response branches observed for transverse-only vibrations, were not found. Sarpkaya [54] carried out investigations for $f_{Nx}/f_{Ny} = 1-2$ and $m_x^* \neq m_y^*$. He showed that the oscillation amplitudes for $f_{Nx}/f_{Ny} = 1$ increased by 19% compared to those obtained for transverse-only VIV. Sarpkaya [54] found no evidence for distinct cylinder response branches. In the experiments of Dahl et al. [81] $f_{Nx}/f_{Ny} = 1 - 1.9$ was considered, where the mass ratios differed in each directions. They showed that the maximum vibration amplitude shifted to higher reduced velocity values when the natural frequency ratio was increased. At $f_{Nx}/f_{Ny} = 1.9$ two amplitude peaks were observed, which was in agreement with the results of [54]. Dahl et al. [82] carried out both experimental and numerical studies in the range of $f_{Nx}/f_{Ny} = 1 - 2$

with $m_x^* \neq m_y^*$. They showed that when increasing the natural frequency ratio, the third harmonic frequency component of transverse fluid force becomes significant. Considering $m_x^* = m_y^*$, Bao et al. [83] and Wang et al. [84] investigated numerically the effect of natural frequency ratio at Re = 150 and 500, respectively. Both studies reported the occurrence of the third harmonic frequency component in the frequency spectra of transverse fluid force. Jauvtis and Williamson [85] analyzed the effect of mass ratio at the limiting case of $f_{Nx} = f_{Ny} = f_N$ and $m_x^* = m_y^* = m^*$. They found that the streamwise vibration component has only a tiny effect on the transverse oscillation component in the medium mass ratio range $6 < m^* < 25$. In contrast, for $m^* < 6$ the existence of a high-amplitude super-upper branch was reported, where the 2T type of vortex structure (two triple vortices are shed from the cylinder) was observed. The third harmonic component of transverse fluid force was also found, which the authors attributed to the 2T mode of vortex shedding. Sanchis [86] carried out experiments in the range of $f_{Nx}/f_{Ny} < 1$. He found that the response amplitudes were quite similar to those at $f_{Nx} = f_{Ny}$.

As discussed in Section 1.1.3, the CFD computations are mainly carried out at low Reynolds numbers. Similarly to the transverse-only VIV studies, two different types of computations can be found in the literature: (1) when the Reynolds number and the reduced velocity are varied independently and (2) when Re is varied linearly with U^*. Singh and Mittal [72] carried out two sets of computations: (1) at Re = 100 and varying U^* and (2) at $U^* = 4.92$ and varying Re. They showed that the initial↔lower branch transition range is hysteretic, which is consistent with the findings of Brika and Laneville [58]. Hysteresis jump was also found at the upper boundary of the lower branch, which was confirmed by the experiments of Klamo et al. [62]. Singh and Mittal [72] also found that varying the reduced velocity at Re = 100, 2S wakes were identified for low oscillation amplitudes and $C(2S)$ for relatively high oscillation amplitudes. This observation agrees well with the transverse-only VIV results by Leontini et al. [68]. Singh and Mittal [72] showed that varying the Reynolds number above Re = 300, P+S vortex structure was observed (a vortex pair and a single vortex are shed from the cylinder in each vibration period), which is very rare in VIV.

Assuming that the natural frequency of the system is constant, the Reynolds number changes linearly with the reduced velocity [see Eq. (1.13)]. In the following numerical studies 2DoF VIV was investigated, where the natural frequencies in streamwise and transverse directions were chosen to be identical ($f_{Nx} = f_{Ny} = f_N$) and constant. Prasanth et al. [87, 88] investigated the effects of numerical blockage ratio $B = d/H$ (the ratio of the cylinder diameter and the height of the computational domain H) at $K = 16.6$. Similarly to the findings of [72], Prasanth and Mittal [88] observed hysteresis loops at the lower and upper boundaries of the lock-in domain. They showed that the width of the hysteresis loop at the lower boundary of the synchronization range reduces as the blockage ratio is decreased. The hysteresis loop completely disappeared at $B = 2.5\%$. Prasanth and Mittal [88] computed the phase angle Φ_y between the transverse fluid force and the transverse vibration component. An abrupt phase jump (between $\Phi_y = 0°$ and $180°$) was observed at Re = 110. Decomposing the transverse fluid force into pressure and viscous parts, their results showed that the jump in Φ_y was caused by the pressure transverse force, since the viscous part remained in-phase with the transverse vibration component in the entire Re range. Mittal and Singh [89] carried out computations for a very low non-dimensional natural frequency value ($K = 3.1875$) and found that VIV occurred as low as Re = 20, which is in the steady state regime for a stationary cylinder. They showed that the vortex shedding frequency and the natural frequency of the system are relatively far from each other for low mass ratios ($m^* = 4.73$). Increasing the mass ratio up to $m^* = 50$, the frequency values moved closer to each other. This phenomenon was confirmed by the experimental data of Williamson and Govardhan [39].

For two-degree-of-freedom free vibration cases the path of the cylinder is another area of interest. The numerical studies of Mittal and Kumar [38] and Bao et al. [83] and the experimental studies of Sarpkaya [55], Williamson and Govardhan [39], Dahl et al. [41, 81, 82], Blevins and Coughran [40], and Srinil et al. [90] showed that an isolated cylinder placed into a uniform stream usually follows a figure-eight path, where the oscillation frequency in streamwise direction is double that in transverse direction ($f_x^* = 2f_y^*$). In addition to the figure-eight orbits, there are some applications where the cylinder follows orbital motion, where $f_x^* = f_y^*$. Kang et al. [91] investigated experimentally the effects of aspect ratio L/d (where L is the length of the cylinder), and natural frequency ratio f_{Nx}/f_{Ny} on the moving trajectory. Orbital motions such as D-shaped, egg-shaped or raindrop-shaped paths were found for $L/d = 24$ by varying f_{Nx}/f_{Ny}. The effect of natural frequency ratio was less significant for $L/d = 6$; only figure-eight paths were identified. Kheirkhah et al. [42], Oviedo-Tolentino et al. [92] and Marble et al. [93] investigated the VIV of a rigid pivoted cylinder, where the oscillation amplitude varied linearly along the cylinder span. An elliptical path was observed in a wide reduced velocity range. Tu et al. [43] and Gsell et al. [44] investigated numerically the two-dimensional flow around an isolated circular cylinder placed in a planar shear flow. They found that increasing the shear parameter (the ratio of the dimensionless inflow velocity gradient and the free stream velocity at the cylinder center) switched the path of the cylinder from figure-eight to elliptical motion. Prasanth and Mittal [94] carried out systematic computations for two circular cylinders (with identical diameters) in tandem and staggered arrangements. For the staggered arrangement the downstream cylinder showed orbital motion in a wide range of reduced velocity. These studies show that orbital motion truly occurs in several engineering applications. However, to the best knowledge of the author, the occurrence of orbital motion has not been specified for a single isolated cylinder placed into uniform free stream considering low Reynolds numbers.

1.2 Objectives and layout of the current dissertation

In this PhD dissertation incompressible Newtonian constant property fluid flow around a circular cylinder undergoing vortex-induced vibrations is investigated by means of two-dimensional CFD computations. The dissertation is organized as follows:

- In Chapter 2, first the dimensional and non-dimensional forms of the partial differential equations governing the fluid and solid motions are written. After that, the boundary and initial conditions, and the numerical solution methodology are given in detail.
- In order to find the best compromise between accuracy and computational time, independence studies are carried out. Afterwards, the currently obtained results are validated against the data in literature for different vortex-induced vibration cases. The results of these investigations are shown in Chapter 3.
- Based on the literature review (see Section 1.1), different research questions can be addressed, which determine the objectives of this dissertation. I try to answer these questions in Chapters 4, 5 and 6. The research questions and the objectives are detailed in the following points.

Objective I

In experimental studies the independent effects of the Reynolds number Re and the reduced velocity U^* are hard to investigate, since both parameters depend on the free stream velocity. When the natural frequency of the cylinder f_N is constant (which mostly happens in the measurements), a linear relationship can be written between Re and U^* as $\mathrm{Re} = KU^*$, where $K = f_N d^2/\nu$ is the dimensionless natural frequency. Although there are some studies in the literature in which the Reynolds number varied linearly with the reduced velocity [69, 70, 87–89], these investigations are limited to low dimensionless natural frequency values ($K < 20$ for transverse-only VIV and $K < 16.6$ for 2DoF free vibrations). The first research question addressed in this dissertation is as follows:

What are the effects of the dimensionless natural frequency K on the cylinder response and aerodynamic force coefficients?

In order to answer this question, systematic computations are carried out at different dimensionless natural frequency values between $K = 12$ and 35. The Reynolds number is varied in the range of $60 \leq \mathrm{Re} \leq 250$ (corresponding to the variation of K), while the mass and damping ratio values are fixed at $m^* = 10$ and $\zeta = 0\%$, respectively. The results of these investigations are shown in Chapter 4, Section 4.1.

Objective II

Singh and Mittal [72] carried out computations at the fixed reduced velocity of $U^* = 4.92$ in the Reynolds number range $50 \leq \mathrm{Re} \leq 500$. They showed that below $\mathrm{Re} = 300$ the traditional 2S and C(2S) vortex structures occur. However, varying the Reynolds number over $\mathrm{Re} = 300$, the asymmetrical P+S wake mode can be observed, which is rarely identified in vortex-induced vibration cases. About this the following research questions are addressed:

Does P+S wake mode occur at high dimensionless natural frequency values? What is the effect of this asymmetrical mode on the cylinder path?

These questions are aimed to be answered in Chapter 4, Section 4.2. For these aims systematic computations are carried out at fixed mass and damping ratio values of $m^* = 10$ and $\zeta = 0\%$. The dimensionless natural frequency is chosen to be in the domain of $K = 34$–44, and the Reynolds number is changed from $\mathrm{Re} = 60$ to 250 (corresponding to the variation of K).

Objective III

There are several studies available in the literature investigating the streamwise-only vortex-induced vibration of a circular cylinder at moderately high Reynolds numbers, $\mathrm{Re} > 10^3$ [73–78]. However, the forced vibration studies revealed that self-excited streamwise vibration of a circular cylinder is not feasible at low Reynolds numbers [35–37]. In this part of the research project the following question is addressed:

Is it possible for streamwise-only VIV to occur in the low-Re domain? What are the effects of m^* and Re on the cylinder response?

In order to answer these questions, systematic computations are carried out, where the cylinder is restricted to move only streamwise with the free stream. Two sets of computations are performed: (a) at the mass ratio values of $m^* = 2, 5, 10$ and 20, and constant Reynolds number of 180, and (b) different Reynolds numbers between $\mathrm{Re} = 100$ and 250 and fixed mass ratio value of 10. In both computation sets the reduced velocity is varied between $U^* = 1.5$ and 3.5, while the structural damping ratio is fixed at zero ($\zeta = 0\%$). The results of these investigations are presented in Chapter 5.

Objective IV

It was mentioned in Section 1.1.3 that the cylinder responses for high and low Reynolds numbers, considering transverse-only vortex-induced vibrations, show very different characteristics. For high Re, depending on the combined mass-damping parameter $m^*\zeta$, two and three-branch responses can occur. In contrast, in the low-Reynolds number domain, irrespective of the $m^*\zeta$ value, only two-branch response has been identified; a separate upper branch has not yet been reported.

However, there are some results available in the literature, which suggest that the upper branch can occur at low Reynolds numbers. Evangelinos and Karniadakis [71] concluded from their 2D and 3D computations that the upper branch may be associated with the asymmetrical P+S mode (see Section 1.1.3). Leontini et al. [31] using transverse-only forced vibration computations showed that the P+S vortex structure appears at Re = 300 in a thin range near the fundamental lock-in domain (see Section 1.1.2). Singh and Mittal [72] carried out 2DoF VIV computations, and they found this asymmetrical wake mode for Re > 300 (see Section 1.1.5). For this reason the following research questions are addressed:

Does the upper branch (i.e. the three-branch cylinder response) occur at the Reynolds number of 300? What is the effect of structural damping on the cylinder response?

In order the answer these research questions, computations are performed at the Reynolds number and mass ratio values of Re = 300 and $m^* = 10$, respectively. Damping ratio between $\zeta = 0\%$ and 5% is considered, that is, the combined mass-damping parameter is chosen to be in the range of $m^*\zeta = 0$ and 0.5. The reduced velocity based on the natural frequency of the cylinder in vacuum is varied from $U^* = 2.5$ to 7.5. The results of this analysis are shown in Chapter 6.

Chapter 2

Methodology

In this dissertation fluid flow around a circular cylinder undergoing vortex-induced vibrations is analyzed at low Reynolds numbers using a two-dimensional *Computational Fluid Dynamics* (CFD) approach. The outline of this chapter is as follows. In Sections 2.1 and 2.2 the dimensional and dimensionless forms of the governing equations of fluid and solid motions are introduced. In Section 2.3 the applied boundary conditions are given and, finally, in Section 2.4 the numerical solution methodology is presented.

2.1 Dimensional forms of the governing equations

The partial differential equations governing the Newtonian incompressible constant property fluid flow around an oscillating circular cylinder are the two components of the Navier-Stokes equations (written in the non-inertial frame of reference attached to the moving body) and the continuity equation, which in dimensional forms are written as follows:

$$\frac{\partial \widetilde{u}}{\partial \widetilde{t}} + \widetilde{u}\frac{\partial \widetilde{u}}{\partial \widetilde{x}} + \widetilde{v}\frac{\partial \widetilde{u}}{\partial \widetilde{y}} = -\frac{1}{\rho}\frac{\partial \widetilde{p}}{\partial \widetilde{x}} + \nu\left(\frac{\partial^2 \widetilde{u}}{\partial \widetilde{x}^2} + \frac{\partial^2 \widetilde{u}}{\partial \widetilde{y}^2}\right) - \ddot{\widetilde{x}}_0, \tag{2.1}$$

$$\frac{\partial \widetilde{v}}{\partial \widetilde{t}} + \widetilde{u}\frac{\partial \widetilde{v}}{\partial \widetilde{x}} + \widetilde{v}\frac{\partial \widetilde{v}}{\partial \widetilde{y}} = -\frac{1}{\rho}\frac{\partial \widetilde{p}}{\partial \widetilde{y}} + \nu\left(\frac{\partial^2 \widetilde{v}}{\partial \widetilde{x}^2} + \frac{\partial^2 \widetilde{v}}{\partial \widetilde{y}^2}\right) - \ddot{\widetilde{y}}_0, \tag{2.2}$$

$$\widetilde{D} = \frac{\partial \widetilde{u}}{\partial \widetilde{x}} + \frac{\partial \widetilde{v}}{\partial \widetilde{y}} = 0. \tag{2.3}$$

In these equations tilde $(\widetilde{\ldots})$ refers to dimensional quantities, i.e., $\widetilde{t}$ is time, $\widetilde{u}$ and $\widetilde{v}$ are the velocity components along $\widetilde{x}$ (streamwise) and $\widetilde{y}$ (transverse) Cartesian directions, respectively, $\widetilde{p}$ is hydrodynamic pressure that involves components due to fluid motion and gravitational force (see details for example in [95]), ρ and ν are the density and kinematic viscosity of the fluid and $\widetilde{D}$ is dilation. In Eqs. (2.1) and (2.2) $\ddot{\widetilde{x}}_0$ and $\ddot{\widetilde{y}}_0$ are the acceleration components of the cylinder in streamwise and transverse directions, respectively.

Figure 2.1 shows the layout of the elastically supported circular cylinder, where the body with diameter of d and mass per unit length of m is elastically constrained in both streamwise and transverse directions. This vibration system is placed into a uniform flow characterized by the free stream velocity U_∞. Vortices shedding from the cylinder means a periodic load on the structure that can cause the vibration of the body; in this case in two degrees of freedom (2DoF). The possibility of high-amplitude oscillation strongly depends on the natural frequency of the system, which in vacuum is defined as

$$f_N = \frac{1}{2\pi}\sqrt{\frac{k}{m}}, \tag{2.4}$$

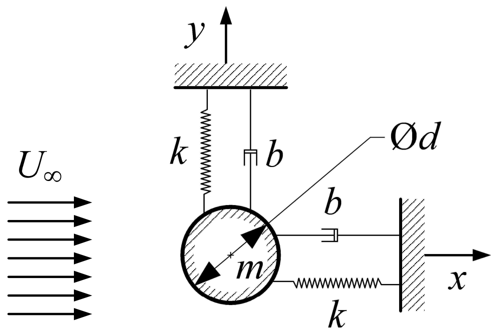

Figure 2.1: Layout of the elastically supported cylinder

where k is the spring stiffness, which is identical in $\widetilde{x}$ and $\widetilde{y}$ directions (see Fig. 2.1); thus, the natural frequencies are also equal in the streamwise and transverse directions. However, in experimental studies cylinder natural frequency is measured in still fluid, which can be expressed as

$$f_{N,a} = \frac{1}{2\pi}\sqrt{\frac{k}{m+m_A}}. \tag{2.5}$$

In this equation $m_A = C_A\rho\frac{d^2\pi}{4}$ is the added mass per unit length of the body, where C_A is the added mass coefficient. Blevins [56] showed analytically using the potential flow theory that $C_A = 1$ for a circular cylinder.

In order to compute the two acceleration components in Eqs. (2.1) and (2.2), Newton's second laws of motion written for the dynamic system shown in Fig. 2.1 are applied:

$$m\ddot{\widetilde{x}}_0 + b\dot{\widetilde{x}}_0 + k\widetilde{x}_0 = \widetilde{F}_x, \tag{2.6}$$

$$m\ddot{\widetilde{y}}_0 + b\dot{\widetilde{y}}_0 + k\widetilde{y}_0 = \widetilde{F}_y, \tag{2.7}$$

where $\widetilde{x}_0$ and $\dot{\widetilde{x}}_0$ are the streamwise cylinder displacement and velocity, and $\widetilde{y}_0$ and $\dot{\widetilde{y}}_0$ are the same quantities in transverse direction. In these equations overdot indicates derivative with respect to dimensional time. In Eqs. (2.6) and (2.7) b is structural damping and $\widetilde{F}_x$ and $\widetilde{F}_y$ are the fluid force components per unit length of the cylinder in $\widetilde{x}$ and $\widetilde{y}$ directions.

2.2 Non-dimensional governing equations

In this study the governing equations are solved in dimensionless forms. The non-dimensional Navier-Stokes and continuity equations are read as follows:

$$\frac{\partial u}{\partial t} + u\frac{\partial u}{\partial x} + v\frac{\partial u}{\partial y} = -\frac{\partial p}{\partial x} + \frac{1}{\mathrm{Re}}\left(\frac{\partial^2 u}{\partial x^2} + \frac{\partial^2 u}{\partial y^2}\right) - \ddot{x}_0, \tag{2.8}$$

$$\frac{\partial v}{\partial t} + u\frac{\partial v}{\partial x} + v\frac{\partial v}{\partial y} = -\frac{\partial p}{\partial y} + \frac{1}{\mathrm{Re}}\left(\frac{\partial^2 v}{\partial x^2} + \frac{\partial^2 v}{\partial y^2}\right) - \ddot{y}_0, \tag{2.9}$$

$$D = \frac{\partial u}{\partial x} + \frac{\partial v}{\partial y} = 0, \tag{2.10}$$

where $x = \widetilde{x}/d$ and $y = \widetilde{y}/d$ are the dimensionless Cartesian coordinates, $u = \widetilde{u}/U_\infty$ and $v = \widetilde{v}/U_\infty$ are the non-dimensional velocity components in streamwise and transverse directions, respectively, $t = \widetilde{t}U_\infty/d$ is the dimensionless time, $p = \widetilde{p}/(\rho U_\infty^2)$ is the non-dimensional pressure and $\ddot{x}_0 = \ddot{\widetilde{x}}_0 d/U_\infty^2$ and $\ddot{y}_0 = \ddot{\widetilde{y}}_0 d/U_\infty^2$ are the dimensionless streamwise and transverse acceleration components of the cylinder. In Eq. (2.10) $D = \widetilde{D}d/U_\infty$ is the dimensionless dilation and $\mathrm{Re} = U_\infty d/\nu$ is the Reynolds number. Note that, here overdot refers to derivative with respect to dimensionless time.

Theoretically the instantaneous velocity and pressure fields can be obtained by solving Eqs. (2.8)–(2.10). However, as seen in Eq. (2.10), the continuity equation does not explicitly involve time, which can cause numerical instabilities. In order to reduce the computational errors, based on the methodology developed by Harlow and Welch [96], the fluid pressure is obtained by solving a separate Poisson equation, which in non-dimensional form can be written as follows:

$$\nabla^2 p = \frac{\partial^2 p}{\partial x^2} + \frac{\partial^2 p}{\partial y^2} = 2\left(\frac{\partial u}{\partial x}\frac{\partial v}{\partial y} - \frac{\partial u}{\partial y}\frac{\partial v}{\partial x}\right) - \frac{\partial D}{\partial t}. \tag{2.11}$$

Although dilation is zero for incompressible fluids [see Eq. (2.10)], $\partial D/\partial t$ is retained in Eq. (2.11) to avoid computational instabilities [96].

Non-dimensionalizing the cylinder equations of motion [see Eqs. (2.6) and (2.7)], the following dimensionless equations are obtained:

$$\ddot{x}_0 + \frac{4\pi\zeta}{U^*}\dot{x}_0 + \left(\frac{2\pi}{U^*}\right)^2 x_0 = \frac{2C_x}{\pi m^*}, \tag{2.12}$$

$$\ddot{y}_0 + \frac{4\pi\zeta}{U^*}\dot{y}_0 + \left(\frac{2\pi}{U^*}\right)^2 y_0 = \frac{2C_y}{\pi m^*}, \tag{2.13}$$

where $x_0 = \widetilde{x}_0/d$ and $\dot{x}_0 = \dot{\widetilde{x}}_0/U_\infty$ are the dimensionless streamwise cylinder displacement and velocity components, and $y_0 = \widetilde{y}_0/d$ and $\dot{y}_0 = \dot{\widetilde{y}}_0/U_\infty$ are the same quantities in transverse direction. In these equations $U^* = U_\infty/(f_N d)$ is the reduced velocity, $\zeta = b/(2\sqrt{km})$ is the structural damping ratio, and $m^* = 4m/(\rho d^2\pi)$ is the mass ratio. In Eqs. (2.12) and 2.13) C_x and C_y are the streamwise and transverse fluid force coefficients, respectively, which are computed from the pressure and shear stress distributions on the cylinder surface. Therefore C_x and C_y can be divided into two parts:

$$\frac{\widetilde{F}_x}{\frac{\varrho}{2}U_\infty^2 d} = C_x = C_{xp} + C_{xv}, \qquad \frac{\widetilde{F}_y}{\frac{\varrho}{2}U_\infty^2 d} = C_y = C_{yp} + C_{yv}, \tag{2.14a, b}$$

where subscripts p and v refer to pressure and viscous parts, respectively.

2.3 Boundary and initial conditions

In the left-hand side of Fig. 2.2 the physical domain is shown, where R_1 is the dimensionless radius of the cylinder and R_2 represents the outer surface of the physical domain. On the cylinder surface ($R = R_1$) no-slip boundary conditions are applied to the velocity components u and v and Neumann-type boundary condition is used for pressure p:

$$u = 0, \qquad v = 0, \tag{2.16a, b}$$

$$\frac{\partial p}{\partial n} = \frac{1}{\mathrm{Re}}\nabla^2 v_n - \ddot{x}_{0n} - \ddot{y}_{0n}. \tag{2.17}$$

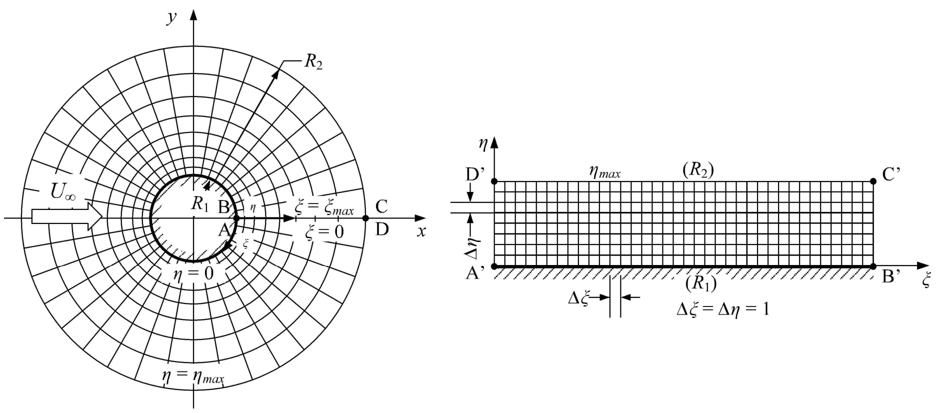

Figure 2.2: The physical and computational domains

where subscript n refers to the outer normal of the circular cylinder. In the outer surface of the physical domain ($R = R_2$) potential flow ("*pot*") is assumed, so that

$$u = u_{pot} - \dot{x}_0, \qquad v = v_{pot} - \dot{y}_0, \tag{2.18a, b}$$

and

$$\frac{\partial p}{\partial n} = \left(\frac{\partial p}{\partial n}\right)_{pot} \cong 0. \tag{2.19}$$

Posdziech and Grundmann [17] and Baranyi [50] showed that this simplification causes only small distortions in the velocity fields. At $t = 0$ cylinder is assumed to be at rest, that is

$$x_0(t = 0) = y_0(t = 0) = 0, \quad \text{and} \quad \dot{x}_0(t = 0) = \dot{y}_0(t = 0) = 0. \tag{2.20a, b}$$

Potential flow is assumed around the cylinder at $t = 0$, hence the force coefficients are $C_x(t = 0) = C_y(t = 0) = 0$, which combined with Eqs. (2.12, 2.13) and (2.20) yields zero initial cylinder acceleration $\ddot{x}_0(t = 0) = \ddot{y}_0(t = 0) = 0$.

In order to satisfy boundary conditions described by Eqs. (2.16)-(2.19) accurately, boundary fitted coordinates are used. For this reason, applying linear mapping functions [50] the physical domain shown in the left-hand side of Fig. 2.2 is transformed into a rectangular computational domain (see on the right in Fig. 2.2). Due to the properties of the mapping functions, the computational grid on the physical domain is very fine in the vicinity of the cylinder and coarse in the far field, but the grid is equidistant in the computational domain.

2.4 Numerical solution

The transformed governing equations with the mapped boundary conditions are solved using an in-house CFD code based on finite difference method [50]. The space derivatives are approximated using fourth order accurate schemes, except for convective terms, which are discretized using the third order modified upwind difference schemes [97]. The equations of fluid and solid motions are integrated in time explicitly using the first order Euler and fourth order Runge-Kutta methods, respectively. The linear system obtained from the discretization of the pressure Poisson equation is solved iteratively using the successive over-relaxation (SOR) method, while the continuity equation is satisfied at each time step.

At each time step, integrating shear stress and pressure around the surface of the cylinder, fluid force coefficients C_x and C_y can be obtained. Substituting the calculated force components into cylinder equations of motion and integrating them numerically, cylinder displacement, velocity and acceleration components can be computed. At the next time step the acceleration components are updated, and the two components of the Navier-Stokes equations are integrated numerically to obtain the new velocity fields. Using the previously computed u and v values the Poisson equation is solved for pressure, where the continuity equation is satisfied.

Chapter 3

Verification and validation

The numerical approach detailed in Chapter 2 has been employed previously in several studies on flow around a stationary cylinder [15] and flow around a cylinder undergoing forced vibrations [32, 46, 50]. However, the in-house code has not yet been used to investigate vortex-induced vibration of a circular cylinder, hence careful validation is required before carrying out the systematic computations. In Section 3.1 the results of independence studies used to determine the optimal combination of computational parameters are shown. Afterwards, a step-by-step validation is presented, where the currently obtained results are compared against those available in the literature. First, single-degree-of-freedom VIV are investigated, where the cylinder is allowed to oscillate only in transverse or streamwise direction (see the results in Sections 3.2 and 3.3, respectively). Then, comparisons are shown for 2DoF VIV cases, where the natural frequencies are equal or different in x and y directions. These results are presented in Section 3.4.

3.1 Independence studies

The three parameters, which characterize the computational setup are the radius ratio R_2/R_1, grid resolution $\xi_{max} \times \eta_{max}$ (number of grid points in the peripheral and radial directions, respectively), and the dimensionless time step Δt. In order to find the optimal combination of these parameters, which is the best compromise between high accuracy and computational cost, independence studies are needed. In these investigations 2DoF VIV is considered where Reynolds number, reduced velocity, mass ratio and structural damping ratio values are fixed at $\mathrm{Re} = 205$, $U^* = 4.8029$, $m^* = 10$ and $\zeta = 0\%$, respectively. Note that this is a special parameter combination where the so-called raindrop-shaped cylinder path is identified (see details in Chapter 4 and also in [J3]). The root-mean-square (rms) values of streamwise and transverse cylinder displacements $x_{0'}$ and $y_{0'}$, the rms values of fluid force coefficients in the same directions $C_{x'}$ and $C_{y'}$ and the time-mean values of streamwise fluid force coefficient $\overline{C}_x$ are presented.

First, the effect of radius ratio is analyzed, where the number of grid points on the cylinder surface is set to $\xi_{max} = 360$, and the dimensionless time step value is chosen to be $\Delta t = 0.0005$. Radius ratio values of $R_2/R_1 = 120, 160$ and 200 are considered. In order to create an equidistant grid on the computational domain, the number of grid points in the radial direction (belonging to the investigated R_2/R_1 values) are chosen to be $\eta_{max} = 274, 291$ and 304. The results are shown in Table 3.1. The relative difference between $y_{0'}$, $C_{x'}$ and $\overline{C}_x$ values obtained from $R_2/R_1 = 120$ and those from $R_2/R_1 = 200$ is less than 0.35%. On the other hand the relative difference between $x_{0'}$ for $R_2/R_1 = 120$ and 200 is 1.03%, and between $C_{y'}$ for the same radius ratio values is 1.5%. However, comparing the results obtained from $R_2/R_1 = 160$ and 200 the relative difference values are under 0.4%. For this reason, the radius ratio value of $R_2/R_1 = 160$ is chosen for further computations.

Table 3.1: Effect of radius ratio on the computational results for Re = 205 and $U^* = 4.8029$

R_2/R_1	$x_{0'}$	$y_{0'}$	$C_{x'}$	$C_{y'}$	$\overline{C}_x$
120	0.02535	0.4098	0.5179	0.3390	2.0487
160	0.02519	0.4105	0.5192	0.3404	2.0449
200	0.02509	0.4108	0.5197	0.3441	2.0416

A grid dependence study is carried out to investigate the effect of ξ_{max} (the number of grid points on the cylinder surface) on the cylinder response and aerodynamic force coefficients. $\xi_{max} = 300, 360$ and 420 are investigated. To make the mesh equidistant on the computational domain the number of points in radial direction is increased with ξ_{max}; $\eta_{max} = 242, 291$ and 339 are used. In Table 3.2 the results of the grid dependence study are shown. It can be seen that ξ_{max} has only a minimal effect on $y_{0'}$, $C_{x'}$ and $\overline{C}_x$. The relative difference between the values obtained from the two coarsest grids ($\xi_{max} = 300$ and 360) and those from $\xi_{max} = 420$ is less than 0.18%. However, grid resolution has a higher impact on $x_{0'}$ and $C_{y'}$. The relative difference between $x_{0'}$ and $C_{y'}$ for $\xi_{max} = 300$ and $\xi_{max} = 420$ is approximately 1%. Increasing the grid resolution up to $\xi_{max} = 360$, the relative difference decreases to 0.3% for both $x_{0'}$ and $C_{y'}$. Consequently, $\xi_{max} = 360$ seems to be adequate for further systematic computations.

Table 3.2: Results of the grid dependence study for Re = 205 and $U^* = 4.8029$

ξ_{max}	$x_{0'}$	$y_{0'}$	$C_{x'}$	$C_{y'}$	$\overline{C}_x$
300	0.02531	0.4102	0.5188	0.3380	2.0475
360	0.02519	0.4105	0.5192	0.3404	2.0449
420	0.02508	0.4107	0.5193	0.3414	2.0439

Finally, the effect of dimensionless time step is analyzed, while the radius ratio and the grid resolution are fixed at $R_2/R_1 = 160$ and 360×291, respectively. During these investigations time step values of 0.001 (Δt_1), 0.0005 (Δt_2) and 0.00025 (Δt_3) are considered. The results are shown in Table 3.3. The relative differences between $x_{0'}$ and $C_{y'}$ for Δt_1 and for Δt_3 are 1.27% and 1.29%, respectively, while the difference for $y_{0'}$, $C_{x'}$ and $\overline{C}_x$ is under 0.32%. The relative differences between all the investigated values ($x_{0'}$, $y_{0'}$, $C_{x'}$, $C_{y'}$ and $\overline{C}_x$) for Δt_2 and Δt_3 do not exceed 0.35%. Hence, $\Delta t_2 = 0.0005$ is chosen for further computations.

Table 3.3: Effects of dimensionless time step on the computational results for Re = 205 and $U^* = 4.8029$

Δt	$x_{0'}$	$y_{0'}$	$C_{x'}$	$C_{y'}$	$\overline{C}_x$
0.001	0.02545	0.4103	0.5197	0.3433	2.0428
0.0005	0.02519	0.4105	0.5192	0.3404	2.0449
0.00025	0.02513	0.4116	0.5190	0.3392	2.0461

3.2 Validation for transverse-only VIV

Using $R_2/R_1 = 160$, $\xi_{max} \times \eta_{max} = 360 \times 291$ and $\Delta t = 0.0005$ step-by-step validations are carried out. In this section comparisons are shown for one-degree-of-freedom (1DoF) VIV, where the cylinder is allowed to move only in transverse direction; the streamwise displacement, velocity and acceleration components are set to zero, $x_0(t) = \dot{x}_0(t) = \ddot{x}_0(t) = 0$.

Leontini et al. [68] carried out computations at fixed Reynolds number, mass and structural damping ratio values of Re = 200, $m^* = 10$ and $\zeta = 1\%$, respectively. Figure 3.1a shows the dimensionless oscillation amplitude $\hat{y}_0$ and in Fig. 3.1b the amplitude of transverse fluid force coefficient $\hat{C}_y$ is plotted against reduced velocity. Note that in these notations the hat symbol $(.\hat{.}.)$ refers to the amplitude of the corresponding signal. As seen in the figures the current results show good agreement with those presented in [68].

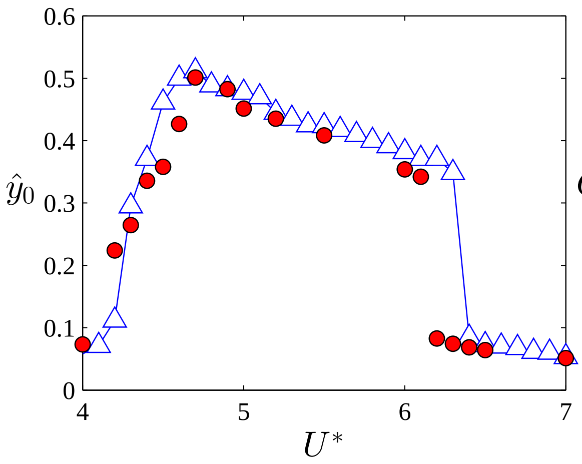

Figure 3.1: Dimensionless amplitude of cylinder oscillation (a) and the amplitude of transverse fluid force coefficient (b) against reduced velocity for Re = 200, $m^* = 10$ and $\zeta = 1\%$; comparison of the current results (●) against those of Leontini et al. [68] (△)

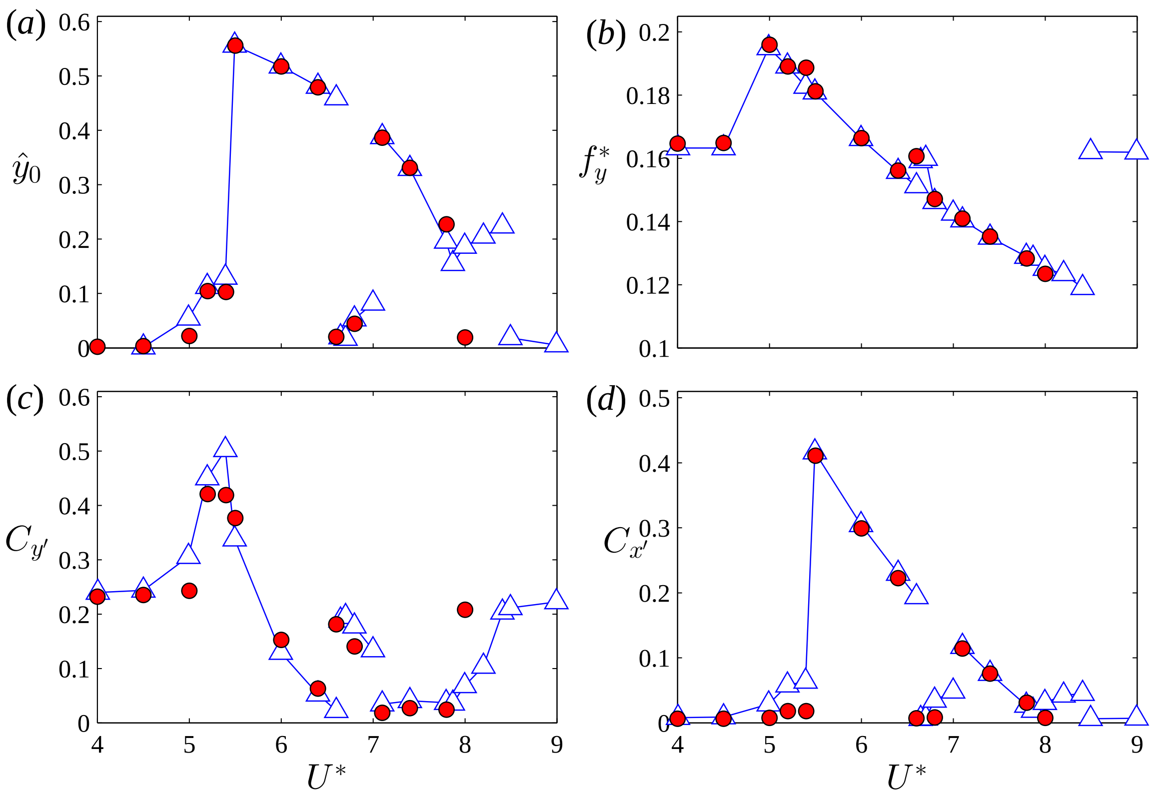

Figure 3.2: Validations for transverse-only VIV: rms values of dimensionless cylinder displacement (a), dimensionless vibration frequency (b), and rms values of transverse (c) and streamwise fluid force coefficients (d) against the reduced velocity for Re = 100, $m^* = 70$ and $\zeta = 0$. △, Navrose and Mittal [66]; ●, present study

Larger discrepancies can be observed between $U^* \cong 4.2$ and 4.8 and in the vicinity of $U^* = 6.2$. These locations correspond to the boundaries of the synchronization domain where the results are very sensitive to the change in reduced velocity.

Navrose and Mittal [66] investigated also transverse-only VIV where the effects of reduced velocity was studied at different mass ratio values ranging from $m^* = 10$ to 150 at Re $= 100$ and $\zeta = 0\%$. At high mass ratios they found a desynchronized range in the middle of the lock-in domain, where the oscillation amplitude was very low. In Figs. 3.2a and 3.2b the dimensionless oscillation amplitude and frequency $\hat{y}_0$ and f_y^*, and in Figs. 3.2c and 3.2d the rms values of transverse and streamwise fluid force coefficients $C_{x'}$ and $C_{y'}$ are plotted against U^* for $m^* = 70$. It can be seen that the agreement between our results and those obtained by Navrose and Mittal [66] is excellent even in the desynchronized regime ($6.5 < U^* \leq 7$).

3.3 Validation for streamwise-only VIV

Streamwise vortex-induced vibrations can also be investigated using the in-house code detailed in Chapter 2. In this case cylinder motion is obtained by solving Eq. (2.12); transverse displacement, velocity and the acceleration components are kept at zero [$y_0(t) = \dot{y}_0(t) = \ddot{y}_0(t) = 0$]. Bourguet and Lo Jacono [79] carried out systematic computations for streamwise VIV of a rotating cylinder at Re $= 100$, $m^* = 40/\pi$ and $\zeta = 0\%$. In Figs. 3.3a and 3.3b the dimensionless oscillation amplitude and frequency $\hat{x}_0$ and f_x^*, and in Figs. 3.3c and 3.3d the amplitudes of streamwise and transverse fluid force coefficients $\hat{C}_x$ and $\hat{C}_y$ are compared against those presented in [79] for a non-rotating cylinder. It can be seen that current results compare very well with those in [79].

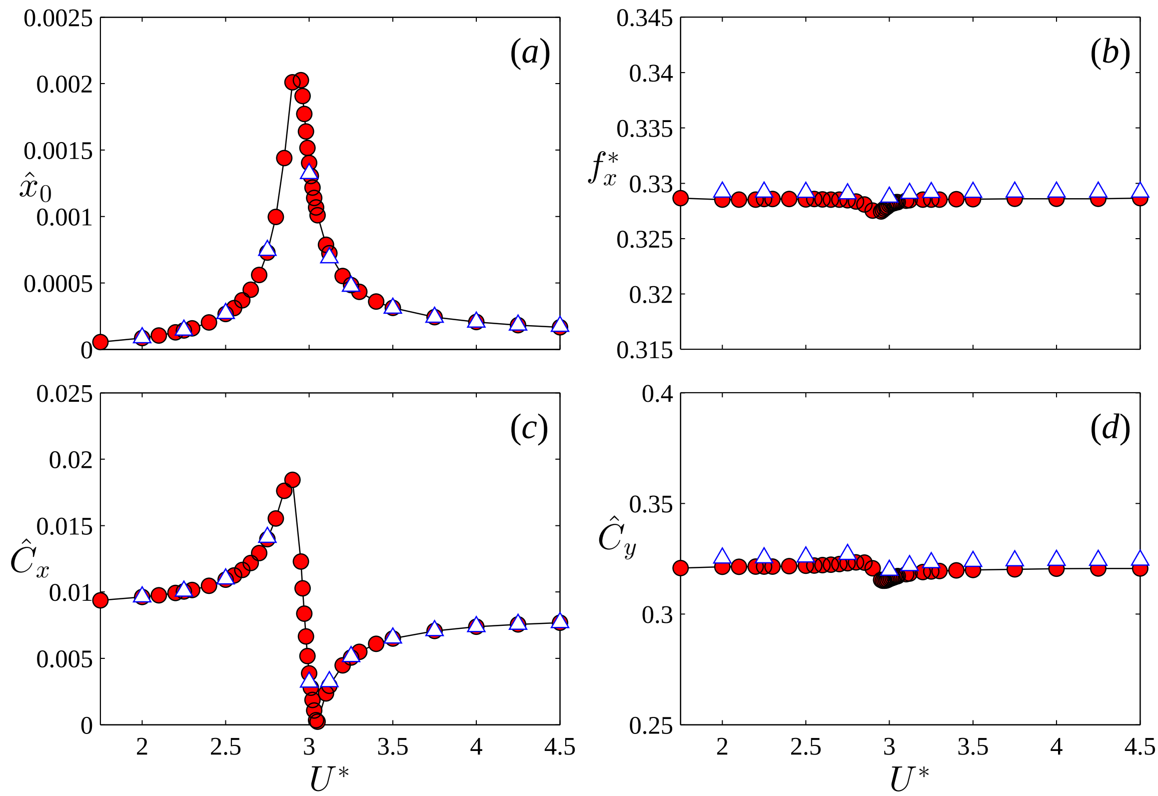

Figure 3.3: Dimensionless oscillation amplitude (a), non-dimensional vibration frequency (b), and root-mean square values of streamwise (c) and transverse fluid forces (d) against the reduced velocity for Re $= 100$, $m^* = 40/\pi$ and $\zeta = 0$. △, Bourguet and Lo Jacono [79]; ●, present study

3.4 Validation for two-degree-of-freedom VIV

Prasanth and Mittal [88] and He and Zhang [98] carried out computations for 2DoF vortex-induced vibrations where the natural frequencies were identical in streamwise and transverse directions, $f_{Nx} = f_{Ny} = f_N$, and it was kept at a constant value, which was chosen to agree with the vortex shedding frequency for a stationary cylinder at the Reynolds number Re = 100. In this case the relationship between Re and U^* is Re $= KU^*$, where $K = f_N d^2/\nu = 16.6$ is the dimensionless natural frequency. The mass ratio was fixed at $m^* = 10$, and the structural damping coefficient was set to zero. In Figs. 3.4a and 3.4b $y_{0'}$ and $x_{0'}$, while in Figs. 3.4c and 3.4d $C_{x'}$ and $C_{y'}$ are shown against the Reynolds number. Similar to the validation cases presented in Section 3.2 the current results and those obtained by [88] and [98] are in a good agreement except for the lower and higher thresholds of the flow synchronization (in the vicinity of Re = 90 and 130).

In the systematic computations carried out by Bao et al. [83] the natural frequencies in streamwise and transverse directions (f_{Nx} and f_{Ny}) were different. They investigated flows at Re = 150, $m^* = 8/\pi$ and $\zeta = 0\%$. The natural frequency ratio FR $= f_{Nx}/f_{Ny}$ was in the range of FR = 1–2. In Figs. 3.5a and 3.5b the streamwise and transverse oscillation amplitudes, and in Figs. 3.5c and 3.5d the time-mean and rms values of stremawise fluid force coefficients are shown against the reduced velocity $U^* = U_\infty/(f_{Ny}d)$ for FR = 2. It can be seen that the currently obtained results compare well with those of [83].

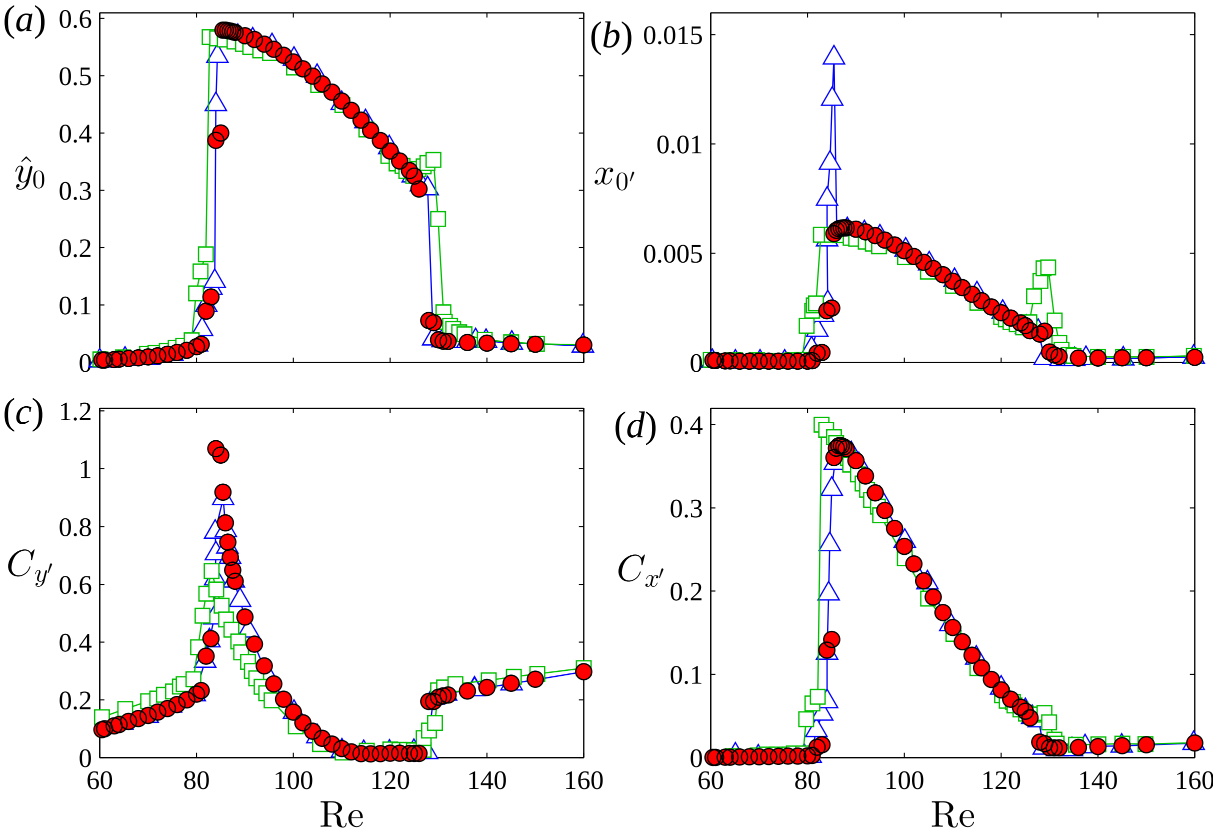

Figure 3.4: Two-degree-of-freedom VIV results (●): transverse oscillation amplitude (a), and rms values of streamwise cylinder displacement (b), transverse fluid force (c) and stremawise fluid force coefficients (d) against the Reynolds number compared to [88] (△) and [98] (□)

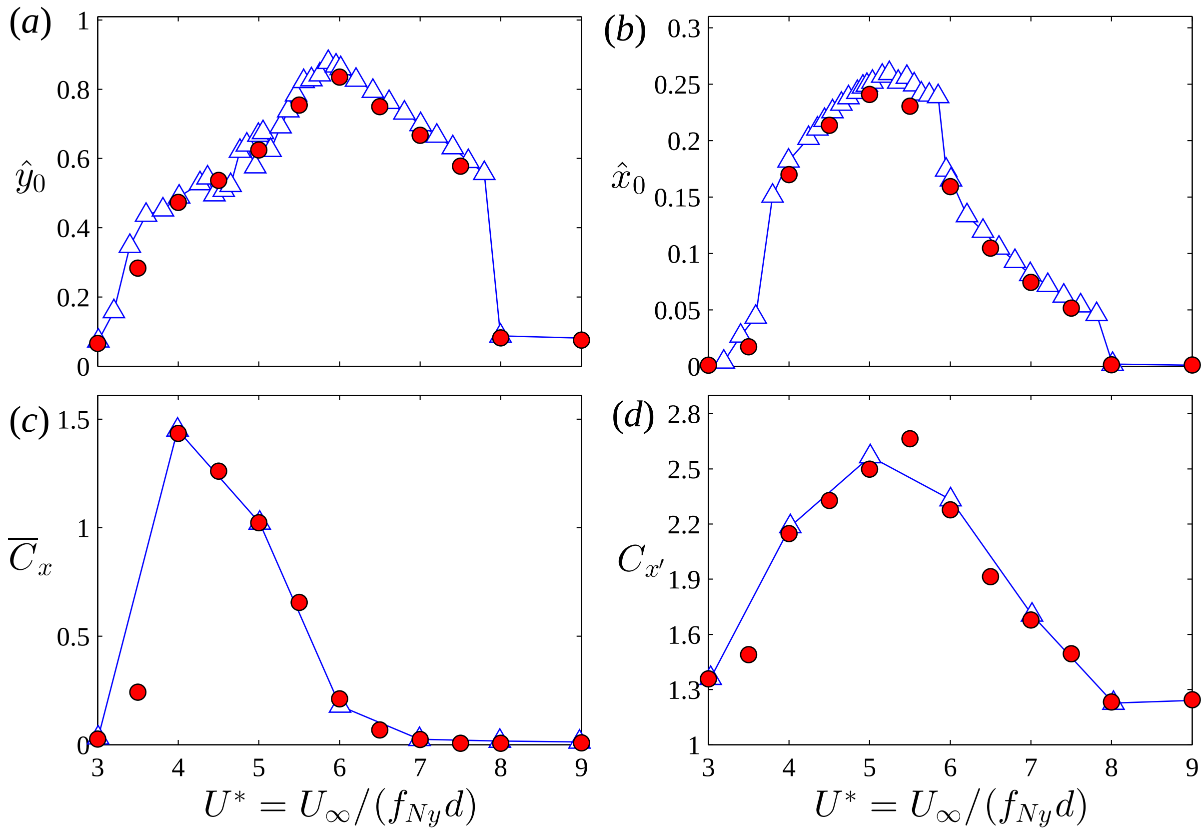

Figure 3.5: Results for cylinder vibrating freely in two degrees of freedom (●): transverse (a) and streamwise oscillation amplitudes (b), and time-mean (c) and root-mean-square (d) values of streamwise fluid force coefficient against the reduced velocity compared to [83] (△)

3.5 Conclusions

In this section, first, independence studies are carried out to find the optimal combination of the computational parameters. These investigations resulted in $R_2/R_1 = 160$, $\xi_{max} \times \eta_{max} = 360 \times 291$ and $\Delta t = 0.0005$. Using these set of parameters validations are carried out with ascending complexity. The comparisons of our results against those presented in Leontini et al. [68], Navrose and Mittal [66], Bourguet and Lo Jacono [79], Prasanth and Mittal [88], He and Zhang [98] and Bao et al. [83] show very good agreements. Additional comparisons for stationary and oscillating cylinders in which good agreement was found are presented in Dorogi and Baranyi [J1, J3].

Chapter 4

Two-degree-of-freedom vortex-induced vibrations

In this chapter two-degree-of-freedom vortex-induced vibrations are investigated at constant mass and damping ratio values of $m^* = 10$ and $\zeta = 0\%$, respectively, in the Reynolds number range of Re = 60–250. As discussed in Sections 1.1.3 and 1.1.5, in the experimental studies the Reynolds number and the reduced velocity are not independent parameters. When the natural frequency of cylinder f_N is constant, Re and U^* are in linear relationship, $\mathrm{Re} = KU^*$, where $K = f_N d^2/\nu$ is the dimensionless natural frequency of the system. The literature review revealed that earlier investigations had been limited to low dimensionless natural frequency values; for two-degree-of-freedom vortex-induced vibrations only $K \leq 16.6$ cases were analyzed [87–89]. Hence, one can ask the question as follows (see also in Section 1.2):

What are the effects of the dimensionless natural frequency K on the cylinder response and aerodynamic force coefficients?

In order to answer this question, systematic computations are carried out at four different K values ranging between approximately $K = 12.3$ and 34.7. The results of these computations are discussed in Section 4.1.

Singh and Mittal [72] investigated 2DoF VIV at fixed reduced velocity value of $U^* = 4.92$ and varying Re. They showed that for Re < 300 the classic 2S and C(2S) vortex structures occur, while for Re > 300 they identified the asymmetrical P+S wake mode. One can ask the following questions (see also in Section 1.2):

Does P+S wake mode occur at high dimensionless natural frequency values? What is the effect of this asymmetrical mode on the cylinder path?

This gave me the motivation to carry out further systematic computations for dimensionless natural frequency values between $K \cong 34.7$ and 43.7. The results of this analysis are given in Section 4.2 in detail.

Since the dimensionless natural frequency values used in the computations mentioned below are calculated based on assumptions (see details in [J1, J3]), these values are not whole numbers. The exact and the rounded K values, and the corresponding markers used in the figures in Sections 4.1 and 4.2 are summarized in Table 4.1. For the sake of simplicity, in further discussions the rounded K values will be used.

4.1 Dimensionless natural frequency effects at K=12–35

In this section systematic computations are carried out for different dimensionless natural frequency values ranging from $K \cong 12.3$ to 34.7 (see Table 4.1). The mass and the

Table 4.1: Dimensionless natural frequency values used in this chapter.

Section	$K = f_N d^2/\nu$	K (rounded)	Marker
4.1	12.3440	12.3	◆
	16.6000	16.6	●
	25.4920	25.5	■
	34.7400	34.7	▲
4.2	34.7400	34.7	▲
	36.5854	36.6	■
	37.6016	37.6	▼
	38.6179	38.6	◆
	40.6504	40.7	●
	42.6829	42.7	◀
	43.6992	43.7	◆

structural damping ratio values are fixed at $m^* = 10$ and $\zeta = 0\%$, respectively, while the Reynolds number is varied in the domain of Re = 60–250.

Figure 4.1a shows the root-mean-square values of the transverse cylinder displacement $y_{0'}$ and in Fig. 4.1b the variations of the dimensionless transverse vibration frequency f_y^*, the Strouhal number St and the reciprocal values of the reduced velocity U^{*-1} are shown against the Reynolds number for $K \cong 25.5$. It can be seen that, the cylinder response shows two-branch behavior, which is typical for low Reynolds numbers. Below Re $\cong$ 110 $y_{0'}$ is very low, and the transverse vibration frequency is close the Strouhal number, $f_y^* \cong$ St. Between Re $\cong$ 110 and 130 an initial branch is found, where the transverse vibration amplitude increases intensively. In this range the frequency of cylinder vibration locks neither to St nor to U^{*-1}. Beyond the initial branch up to Re $\cong$ 165, the lower branch is identified where the oscillation frequency synchronizes with the natural frequency of the system, i.e. $f_y^* \cong U^{*-1}$, resulting in high oscillation amplitudes. Above Re = 165 the oscillation amplitude becomes small again and f_y^* locks in to St, as was observed in the very low amplitude range at Re < 110.

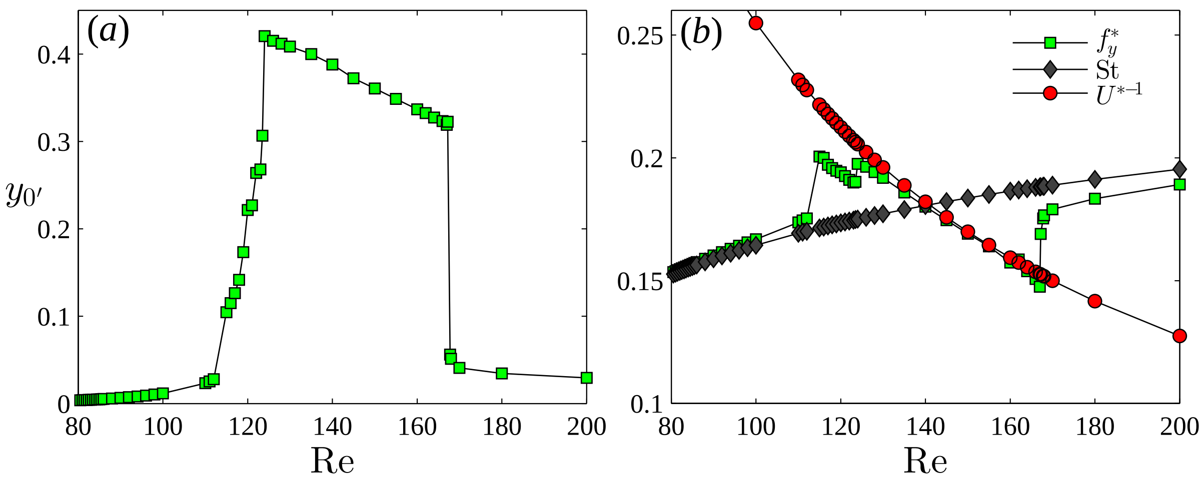

Figure 4.1: The root-mean-square values of the dimensionless transverse cylinder displacement (a), and the dimensionless transverse vibration frequency, the Strouhal number [17], and the reciprocal values of the reduced velocity for $K \cong 25.5$ against the Reynolds number

In Fig. 4.2a the $y_{0'}$ values obtained for different dimensionless natural frequencies ranging between $K \cong 12.3$ and 34.7 are shown against the Reynolds number. It can be seen that the Reynolds number range where flow synchronization is identified strongly depends on K, therefore the comparison of the data is difficult. Khalak and Williamson [59] showed that the cylinder responses for different combined mass-damping parameters $m^*\zeta$ plotted against the "true" reduced velocity $1/f_y^*$ (instead of reduced velocity U^*) can collapse into a single curve. Since $\zeta = 0\%$ in this set of computations, the mass-damping parameter is zero in all the cases investigated in this dissertation. Singh and Mittal [72] used $U^*\mathrm{St}$ as an independent variable for the cases where either Re or U^* was kept constant:

$$U^*\mathrm{St} = \frac{U_\infty}{f_N d}\frac{f_v}{U_\infty d} = \frac{f_v}{f_N}. \tag{4.1}$$

As can be seen, $U^*\mathrm{St}$ is the ratio of the vortex shedding frequency for a stationary cylinder and the natural frequency of the oscillating body. To the best knowledge of the author, $U^*\mathrm{St}$ as an independent parameter has not previously been applied for constant natural frequency cases.

In Fig. 4.2b the rms values of transverse cylinder displacement is plotted against $U^*\mathrm{St}$. This figure shows that the curves belonging to different K values can be represented in the same range, i.e., using $U^*\mathrm{St}$ as an independent parameter is advantageous. It can be seen in Fig. 4.2b that the $y_{0'}$ curves shift upwards when the dimensionless natural frequency is increased. A larger difference in $y_{0'}$ values is found between $K \cong 12.3$ and 16.6 than between $K \cong 25.5$ and 34.7. It can also be observed that the lower branch is significantly wider for lower K values. Previous researchers (e.g. [88]) reported that in the initial branch the flow is quasi-periodic, which is the same what I found in this dissertation. My results show also that the width of the initial branch also depends on K. For $K \cong 12.3$ and 16.6 $y_{0'}$ jumps abruptly between the very low amplitude range and the lower branches, while for $K \cong 25.5$ and 34.7 the transverse oscillation amplitude shows a gradual change.

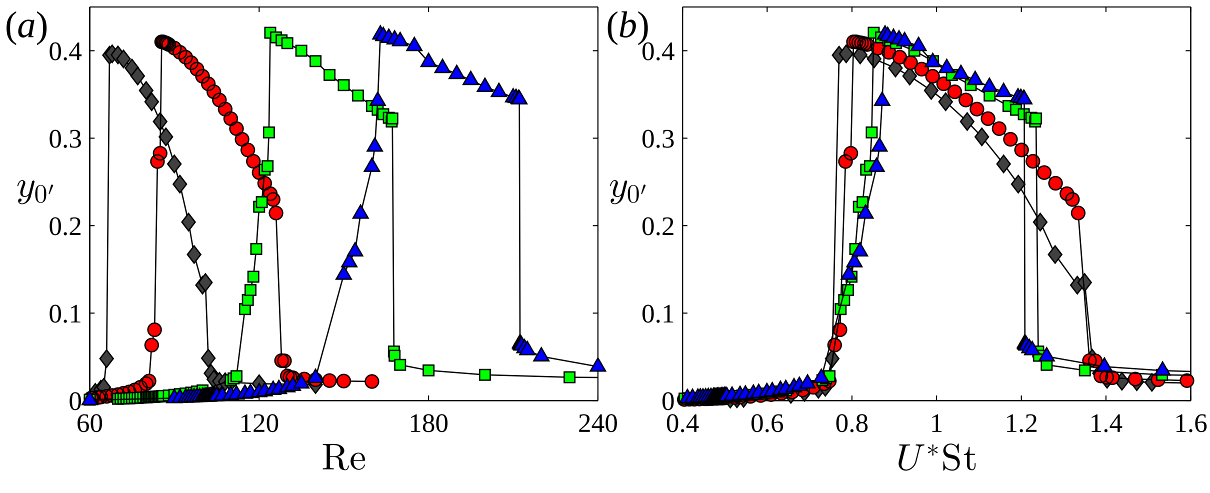

Figure 4.2: Root-mean-square values of dimensionless transverse cylinder displacement against Re (a) and $U^*\mathrm{St}$ (b) for $K \cong 12.3$ (-◆-), 16.6 (-●-), 25.5 (-■-) and 34.7 (-▲-)

In Figs. 4.3a and 4.3b the rms values of streamwise displacement $x_{0'}$ and streamwise fluid force coefficient $C_{x'}$ are shown against $U^*\mathrm{St}$. As expected, the amplitude of cylinder oscillation in streamwise direction is significantly lower than that in the transverse direction. Similar characteristics are observed, as were seen for $y_{0'}$ in Fig. 4.2: the curves belonging to increasing K shift to higher values for both $x_{0'}$ and $C_{x'}$. It is very important to see that the rms values of streamwise cylinder displacement show a local peak value at around $U^*\mathrm{St} \cong 0.47$, which increases with the dimensionless natural frequency (see Fig. 4.3a). As can be seen in Fig. 4.3b, the rms of streamwise fluid force displays a similar

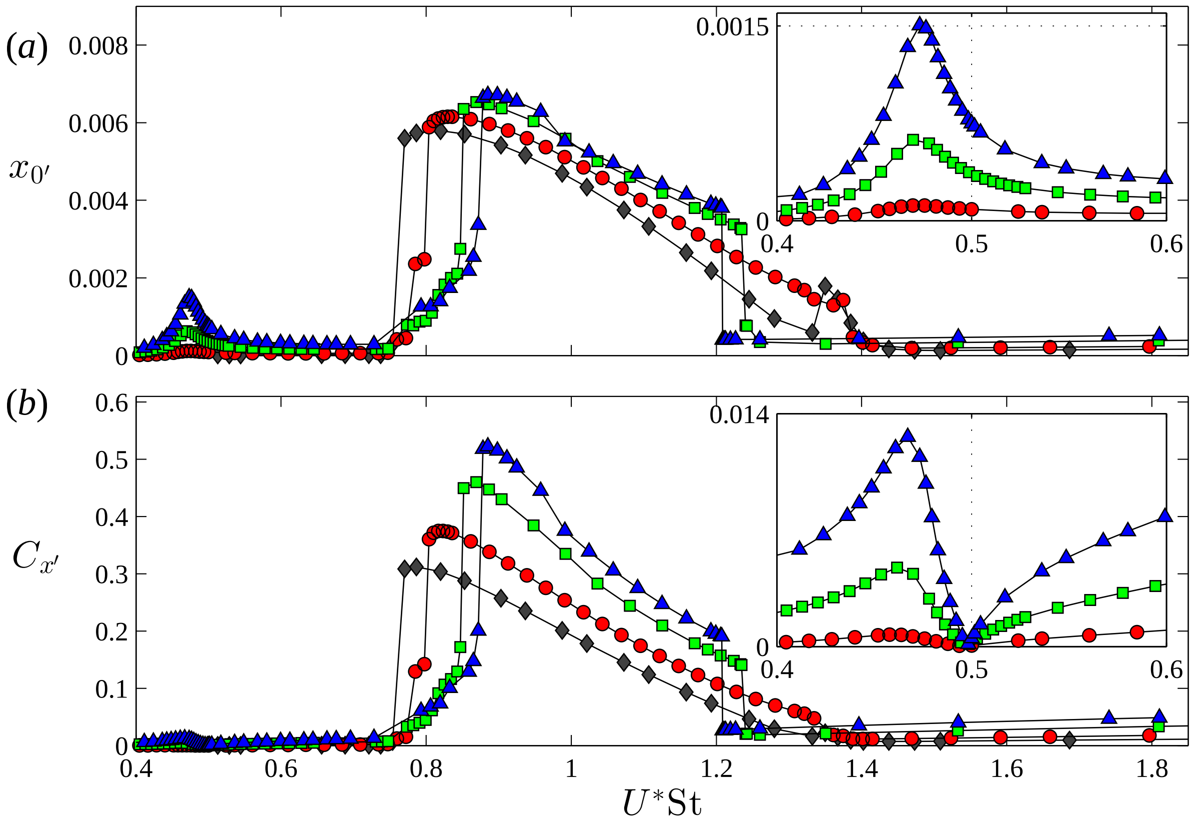

Figure 4.3: Root-mean-square values of dimensionless streamwise cylinder displacement (a) and streamwise fluid force (b) against U^*St for $K \cong 12.3$ (–◆–), 16.6 (–●–), 25.5 (–■–) and 34.7 (–▲–)

feature to that of $x_{0'}$, but $C_{x'}$ varies in a broader range (the peak value of $C_{x'}$ is 0.52, while that of $x_{0'}$ is only 0.0066 for $K \cong 34.7$). That is, the details of $C_{x'}$ close to $U^*\mathrm{St} = 0.47$ are hard to see.

For the aim of better illustration, the domain $0.4 < U^*\mathrm{St} \leq 0.6$ is shown at higher resolution in the inset chart of Figs. 4.3a and 4.3b. Note that $x_{0'}$ and $C_{x'}$ do not display local peaks for $K \cong 12.3$; thus, curves corresponding to this particular dimensionless natural frequency value are not shown in the inset plots. It can be seen in the inset figures that $x_{0'}$ increases continuously until it reaches its local peak value at around $U^*\mathrm{St} = 0.47$ (see Fig. 4.3a). As expected, with decreasing K the peak value decreases, and almost disappears at $K = 16.6$. In addition to the peak, a local minimum point is identified in $C_{x'}$ at $U^*\mathrm{St} \cong 0.5$, where $C_{x'} \to 0$ (see Fig. 4.3b). Beyond the local minimum point $C_{x'}$ starts to increase with the slope of the curve increasing with K.

In order to explore the significance of the local maximum values of $x_{0'}$ and $C_{x'}$ and the local minimum values of $C_{x'}$, the range $0.4 < U^*\mathrm{St} \leq 0.6$ is further investigated. The relative waveforms of streamwise cylinder displacement and fluid force x_0^* and C_x^* are defined as

$$x_0^*(t) = \frac{x_0(t) - \overline{x}_0}{\hat{x}_0}, \tag{4.2}$$

$$C_x^*(t) = \frac{C_x(t) - \overline{C}_x}{\hat{C}_x}, \tag{4.3}$$

where $\overline{x}_0$ and $\overline{C}_x$ are the time-mean values of streamwise displacement and fluid force coefficient, respectively, and $\hat{x}_0$ and $\hat{C}_x$ are the amplitude values of x_0 and C_x. Figure 4.4

shows the time histories of x_0^* and C_x^* at different $U^*\mathrm{St}$ values. It can be seen that the point of $U^*\mathrm{St} \cong 0.5$ separates two different regions. Below $U^*\mathrm{St} \cong 0.5$ the displacement and the fluid force coefficient along the direction of the free stream are in-phase signals, while above the point of approximately $U^*\mathrm{St} = 0.5$ x_0^* is out-of-phase with C_x^*.

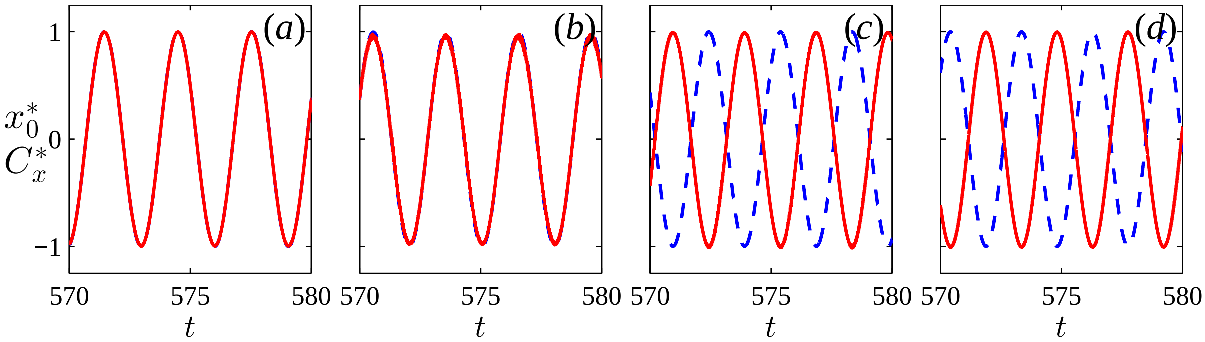

Figure 4.4: The relative waveforms of streamwise cylinder displacement (x_0^*, blue dashed lines) and streamwise fluid force (C_x^*, red solid lines) at $U^*\mathrm{St} = 0.467$ (a), 0.492 (b), 0.498 (c) and 0.536 (d) for $K \cong 34.7$

Let us assume that the streamwise cylinder displacement and the fluid force coefficient are sinusoidal functions of time:

$$x_0(t) = \hat{x}_0 \sin(2\pi f_x^* t), \tag{4.4}$$

$$C_x(t) = \hat{C}_x \sin(2\pi f_x^* t + \Phi_x), \tag{4.5}$$

where f_x^* is the frequency of cylinder vibration in streamwise direction, and Φ_x is the instantaneous phase difference of streamwise fluid force relative to the cylinder displacement in the corresponding direction (hereafter the *streamwise phase*). Note that the mean components of these signals are omitted, because they do not affect the dynamics. The time-dependent streamwise phase (Φ_x) is obtained using the Hilbert transformation, however, in this section only its time-averaged value $\overline{\Phi}_x$ is shown. The calculation methodology of the time-varying phase is shown in Appendix A.2.2 in detail. In Fig. 4.5 the $\overline{\Phi}_x$ values are shown against $U^*\mathrm{St}$ for the dimensionless natural frequencies ranging between

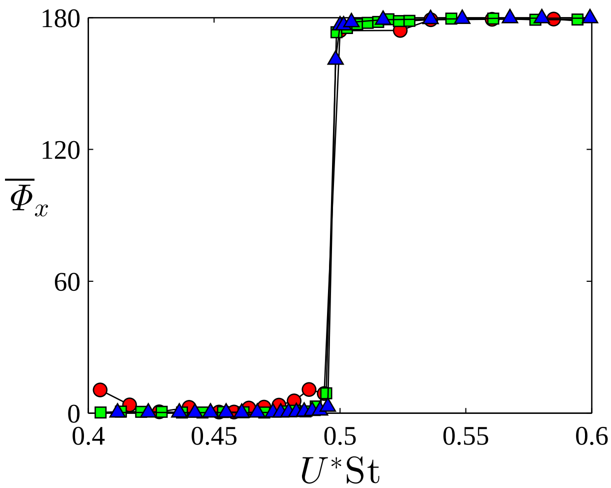

Figure 4.5: Time-averaged phase difference of streamwise fluid force relative to the streamwise cylinder displacement against $U^*\mathrm{St}$ for $K \cong 16.6$ (–●–), 25.5 (–■–) and 34.7 (–▲–)

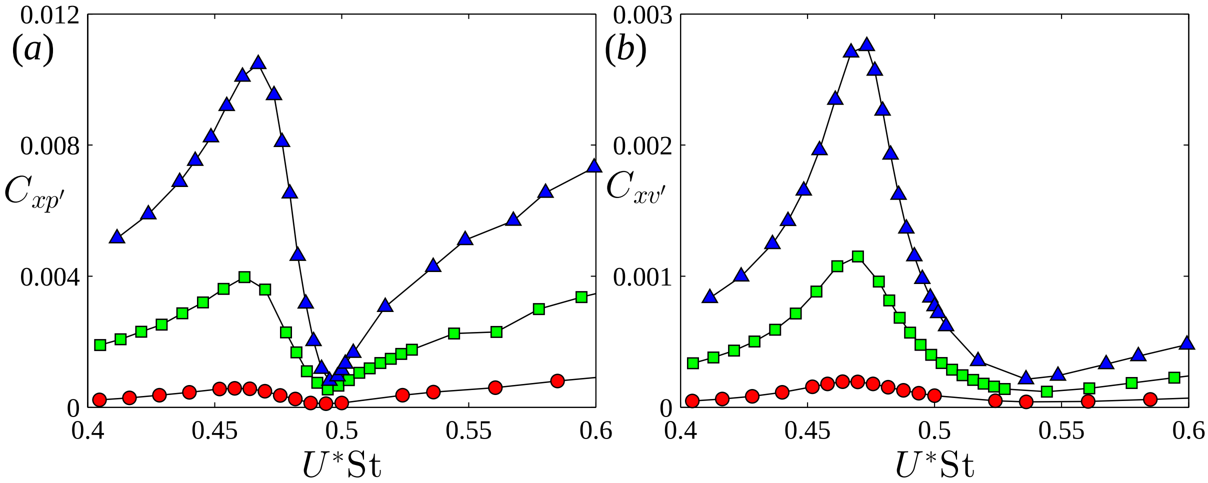

Figure 4.6: Root-mean-square values of pressure streamwise fluid force (a) and viscous streamwise fluid force (b) against U^*St for $K \cong 16.6$ (-●-), 25.5 (-■-) and 34.7 (-▲-)

$K \cong 16.6$ and 34.7. The irregular change in the phase difference can be clearly observed in this figure: for $U^*\mathrm{St} < 0.5$ $\overline{\Phi}_x \cong 0°$, and at the critical value of $U^*\mathrm{St} \cong 0.5$ the time-averaged streamwise phase switches from $\overline{\Phi}_x \cong 0°$ to 180°. This approximately 180° jump can be seen for all K values above $K \cong 12.3$.

The total streamwise fluid force coefficient is composed of two parts: one is due to pressure C_{xp} (pressure streamwise fluid force) and the other part is originated from friction on the cylinder wall C_{xv} (viscous streamwise fluid force), as stated by Eq. (2.14). As can be seen in Fig. 4.6, the rms values of the pressure and viscous streamwise fluid force coefficients $C_{xp'}$ and $C_{xv'}$ in the range $0.4 < U^*\mathrm{St} \leq 0.65$ show different behaviors. Although both quantities have maximum and minimum values in this domain, the variation of $C_{xp'}$ is similar to $C_{x'}$ (see the inset plot in Fig. 4.3b), while the change in $C_{xv'}$ is similar to the characteristics of $x_{0'}$ (see the inset plot in Fig. 4.3a).

In Figs. 4.7a and 4.7b the time-averaged phase differences of C_{xp} and C_{xv} relative to the streamwise cylinder displacement $\overline{\varphi}_{xp}$ and $\overline{\varphi}_{xv}$ are shown as functions of U^*St for $K \cong 16.6$–34.7. It can be seen that, $\overline{\varphi}_{xv}$ and $\overline{\varphi}_{xp}$ show different trends in the vicinity of $U^*\mathrm{St} = 0.5$. In the range of $0.4 < U^*\mathrm{St} \leq 0.5$ there is a $\overline{\varphi}_{xv} \cong 35°$ phase shift between

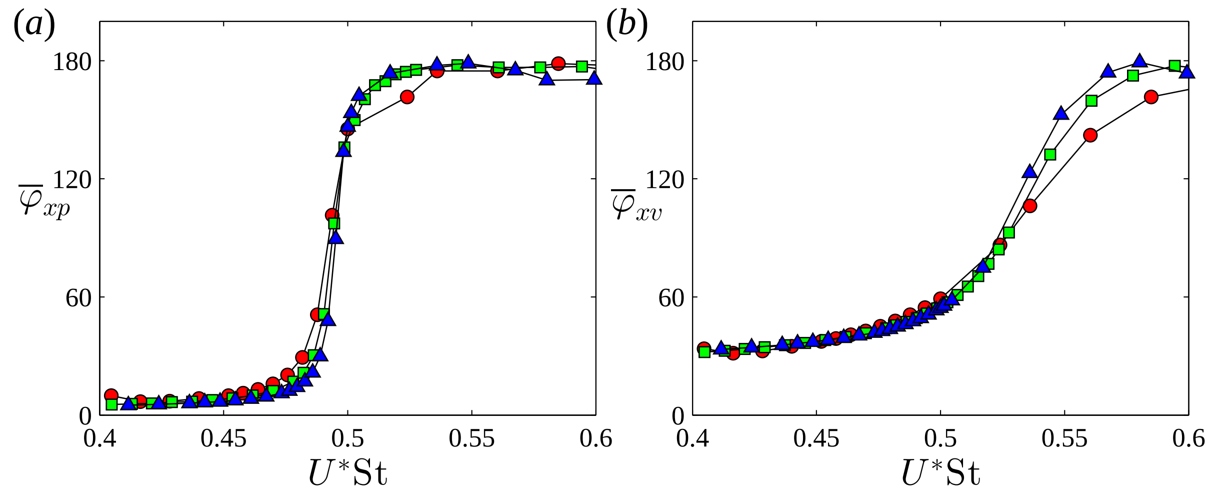

Figure 4.7: Time-averaged phase difference values $\overline{\varphi}_{xp}$ (a) and $\overline{\varphi}_{xv}$ (b) for $K \cong 16.6$ (-●-), 25.5 (-■-) and 34.7 (-▲-)

C_{xv} and x_0. After this period $\overline{\varphi}_{xv}$ changes gradually until it reaches approximately 180° (see Fig. 4.7b). In contrast, C_{xp} and x_0 are approximately in phase between $U^*\mathrm{St} = 0.4$ and 0.5, while in the vicinity of $U^*\mathrm{St} = 0.5$ the time-averaged phase difference changes abruptly to $\overline{\varphi}_{xp} \cong 180°$ (see Fig. 4.7a).

The tendencies of $\overline{\varphi}_{xp}$ and $\overline{\Phi}_x$ are very similar (see Figs. 4.7a and 4.5), therefore pressure distribution around the cylinder surface influences the flow structure more strongly than shear stress does. This behavior is similar to that observed by Prasanth and Mittal [88] for $K = 16.6$, who found an abrupt jump in the phase between the transverse fluid force and displacement from 0° to 180° (between Re = 110 and 115). Decomposing the transverse fluid force into components due to pressure and shear stress they showed that the pressure component is responsible for the jump, since the viscous component remains in-phase with the displacement.

In Fig. 4.8 the limit cycle curves (time histories of viscous streamwise force versus those of pressure streamwise force) are shown in the vicinity of $U^*\mathrm{St} = 0.5$ for $K \cong 25.5$. It can be seen that below $U^*\mathrm{St} \cong 0.499$ the orientation of the curves is clockwise, indicated by filled arrows (see Fig. 4.8). At $U^*\mathrm{St} \geq 0.499$ the orientation switches abruptly to counterclockwise (shown by lined arrows in Fig. 4.8), which means that pressure and viscous streamwise force components become nearly antiphase. This substantial change is mainly caused by C_{xp}, since $\overline{\varphi}_{xv}$ increases gradually in this regime (Fig. 4.7b), in contrast to $\overline{\varphi}_{xp}$, which jumps abruptly between $\overline{\varphi}_{xv} = 0°$ and 180° at around $U^*\mathrm{St} = 0.5$ (Fig. 4.7a). The amplitudes of signals C_{xp} and C_{xv} (closely related to $C_{xp'}$ and $C_{xv'}$) are almost identical in the vicinity of $U^*\mathrm{St} = 0.5$. These two features (antiphase and equal signal amplitudes) nearly cancel each other out, resulting in an approximately zero value of $C_{x'}$ (shown in Fig. 4.3b).

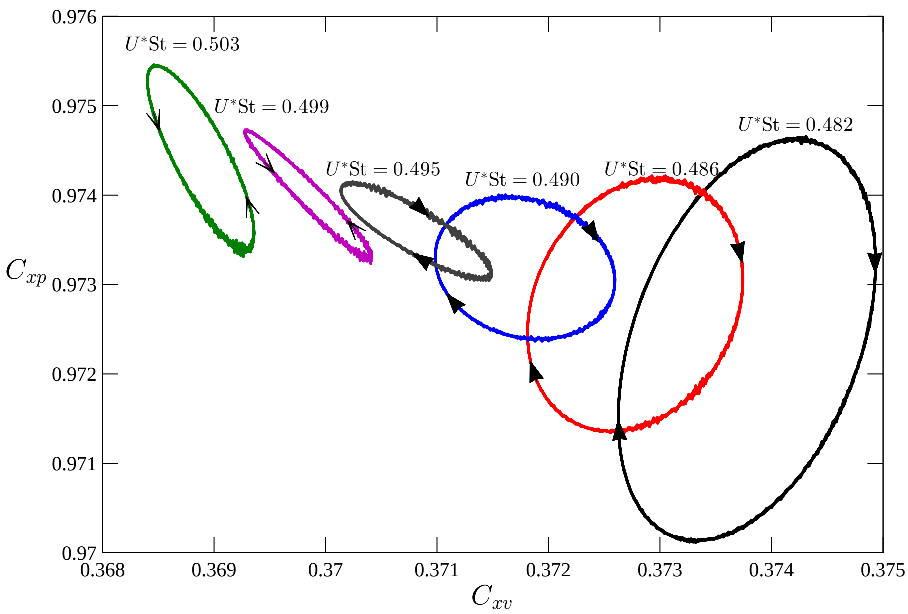

Figure 4.8: Limit cycle curves (C_{xv}, C_{xp}) in the vicinity of $U^*\mathrm{St} = 0.5$ for $K \cong 25.5$

The results of the CFD computations show also that the vibration frequency of the cylinder in streamwise direction is double that in transverse direction, which leads to figure-eight cylinder motion (see Section 1.1.2). In Fig. 4.9 the paths of the cylinder are shown at different $U^*\mathrm{St}$ values for $K \cong 34.7$. Similar to the features observed in the (C_{xv}, C_{xp}) limit cycle curves, the orientation of the motion trajectory switches near the point of $U^*\mathrm{St} = 0.5$. It can be seen that below $U^*\mathrm{St} \cong 0.5$ the orbit is clockwise in the upper loop of the cylinder path, while in the domain of $U^*\mathrm{St} > 0.5$ the orientation of the cylinder trajectory is counterclockwise.

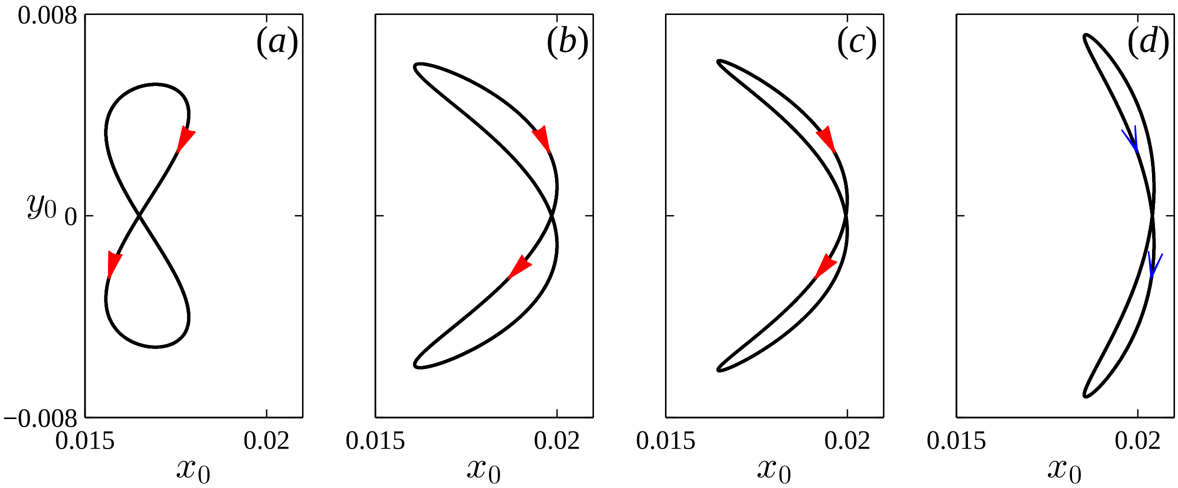

Figure 4.9: Cylinder paths at $U^*\mathrm{St} \cong 0.455$ (a), 0.480 (b), 0.483 (c) and 0.505 (d) for $K \cong 34.7$

4.2 Occurrence of orbital cylinder motion for high dimensionless natural frequencies

As mentioned earlier, in this section systematic computations are carried out to explore whether P+S vortex structure occurs at higher dimensionless natural frequencies. To accomplish this aim, different K values are considered in the range of $K \cong 34.7$–43.7 (see Table 4.1). The Reynolds number is varied in the domain of $\mathrm{Re} = 60$–250, and the mass and structural damping ratio values are fixed at $m^* = 10$ and $\zeta = 0\%$, respectively.

4.2.1 Cylinder response and vortex structures

In Figs. 4.10a and 4.10b $x_{0'}$ and $y_{0'}$ are shown against $U^*\mathrm{St}$ for three different dimensionless natural frequency values. It can be seen in Fig. 4.10a that for $K \cong 40.7$ $x_{0'}$ shows a steep increase (up to $x_{0'} = 0.023$) in the approximate range of $0.92 < U^*\mathrm{St} \leq 0.97$, and then jumps abruptly to lower values ($x_{0'} = 0.005$). For the data sets for $K \cong 16.6$ and 34.7 this phenomenon is not observed, which suggests that only larger K values result in a steep increase in the streamwise oscillation amplitude. In contrast, $y_{0'}$ behaves differently, as

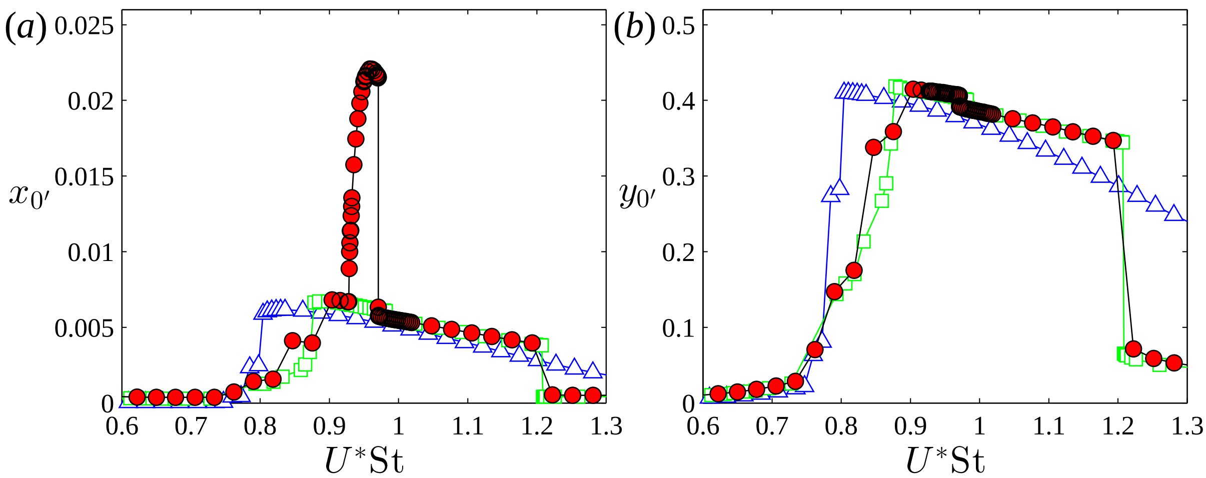

Figure 4.10: Root-mean-square values of streamwise (a) and transverse (b) cylinder displacements against $U^*\mathrm{St}$ for $K \cong 16.6$ (-△-), 34.7 (-□-) and 40.7 (-●-)

only a small jump is found at around $U^*\mathrm{St} = 0.97$ for $K = 40.7$ (Fig. 4.10b).

In order to investigate what happens in the range where $x_{0'}$ steeply increases, first the paths of the cylinder are analyzed. In Fig. 4.11 the ratios of streamwise and transverse oscillation frequencies to the natural frequency of the system in vacuum f_x/f_N and f_y/f_N are shown against $U^*\mathrm{St}$ for $K \cong 40.7$. Figure 4.12 shows the cylinder trajectories (see the top row of the figure), the FFT spectra of streamwise and transverse vibration components (middle row), and the instantaneous vorticity contours (bottom row) at different $U^*\mathrm{St}$ values for $K \cong 40.7$. The blue and the red curves correspond to the FFT spectra of streamwise and transverse oscillation components, respectively. Note that Power Spectral Density (PSD, also referred to as intensity) in Fig. 4.12 is shown in a logarithmic scale.

It can be seen in Fig. 4.11 that conditions $f_y/f_N \cong 1$ and $f_x/f_N \cong 2$ satisfy when $U^*\mathrm{St} < 0.92$ and $U^*\mathrm{St} > 0.97$ (where $x_{0'}$ is sufficiently low), resulting in distorted figure-eight motion (see Figs. 4.12a and 4.12d). This cylinder path occurs most often in vortex-induced vibrations, as seen for example in Mittal and Kumar [38], Williamson and Govardhan [39], Blevins and Coughran [40] and Dahl et al. [41]. Although, the most dominant frequency peaks of transverse and streamwise components are identified at $f/f_N \cong 1$ and 2, respectively (Figs. 4.12a and 4.12d), they show additional (but less significant) peaks. Note that $f/f_N = i$ is usually referred to as the i^{th} harmonic frequency components. In this dissertation the oscillation frequency ratio shown in Fig. 4.11 is defined with the highest-intensity frequency peaks in the spectra. It can also be seen in Figs. 4.12a and 4.12d that the frequency peaks for the two oscillation components do not overlap. For example, the fourth and the third harmonic components are identified in the spectra of x_0 and y_0, respectively, but the $f/f_N = 3$ in streamwise vibration component and the $f/f_N = 4$ in transverse component are not found. Using the notations introduced by Williamson and Roshko [28], at the corresponding $U^*\mathrm{St}$ values where distorted figure-eight motions are found, 2S and C(2S) vortex structures are seem to develop. For both vortex configurations two single vortices are shed from the cylinder, but for the C(2S) wake mode the positive and the negative vortices are in coalescence.

As can be seen in Fig. 4.11, in the range of $0.92 < U^*\mathrm{St} \leq 0.97$ (where $x_{0'}$ increases steeply) both streamwise and transverse vibration frequencies lock into the natural frequency of the system, i.e. $f_x = f_y \cong f_N$. Kheirkhah et al. [42] found similar characteristics for the flow around a pivoted cylinder, and attributed this effect to an orbital type of cylinder motion. Kang et al. [91], investigating the effect of streamwise to transverse natural frequency ratio at different aspect ratios, also found orbital trajectories that they named *raindrop-shaped motion*. In Figs. 4.12b and 4.12c the raindrop-shaped motions and the

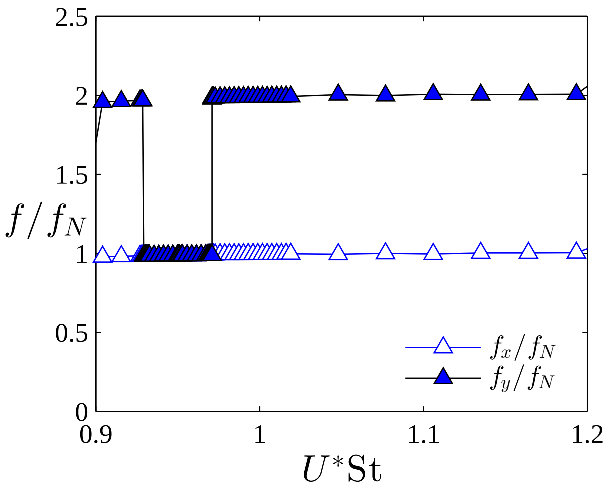

Figure 4.11: Ratios of streamwise and transverse vibration frequencies to the natural frequency of the system for $K \cong 40.7$

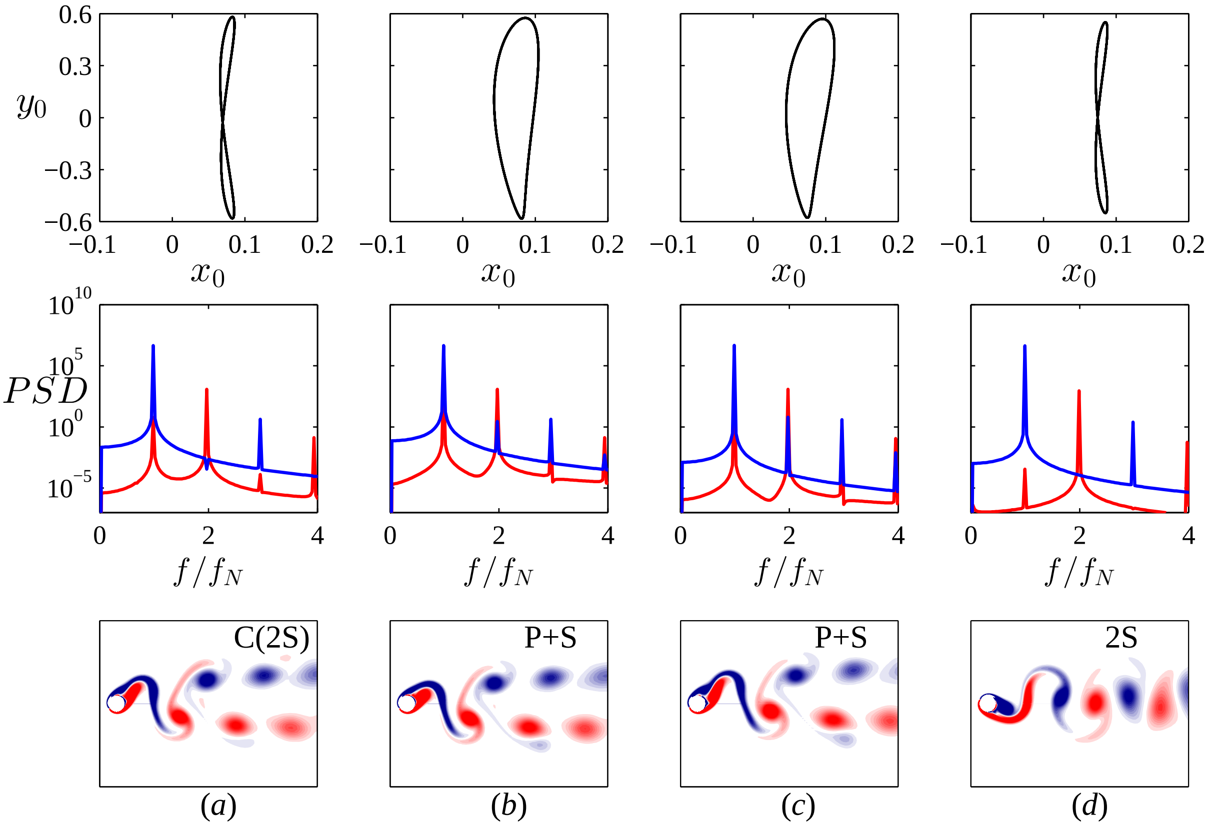

Figure 4.12: Paths of the cylinder (upper row), frequency spectra of streamwise (blue curves) and transverse (red curves) cylinder displacements (middle row), and vortex structures (bottom row) at $U^*\mathrm{St} = 0.9280$ (a), 0.9441 (b), 0.9708 (c) and 0.9757 (d) for $K \cong 40.7$. Each vortex contours are recorded at random phases of the cylinder oscillation

corresponding frequency spectra and vortex structures are shown. In contrast to those observed for distorted figure-eight paths, the high-intensity frequency peaks for the two oscillation components overlap. It can be seen that for streamwise cylinder displacement the first and the second harmonic frequency components play significant role, and in the spectra of transverse displacement only the first harmonic component is identified as high-intensity frequency peak. The Power Spectral Density of the rest of the frequency components is negligible. Due to the fact that two dominant frequency peaks are found for x_0 ($f/f_N = 1$ and 2), the path of the cylinder is asymmetric (see Figs. 4.12b and 4.12c). The asymmetric behavior of the raindrop-shaped motion is confirmed by the vortex configurations; P+S wake modes are identified in these cases (see Figs. 4.12b and 4.12c). Therefore, I can answer the research question I put up at the beginning of Section 4.2; P+S vortex structure can occur at higher natural frequency values.

To conclude the previous findings, it seems likely that the high jump in $x_{0'}$ and the sudden change in $y_{0'}$ occurring at around $U^*\mathrm{St} = 0.97$ for $K \cong 40.7$ (see Fig. 4.10) appear to account for the abrupt changes in the cylinder path (from raindrop-shaped to distorted figure-eight motion) and the switch in the vortex structure (between P+S and 2S modes).

Brika and Laneville [58] investigated experimentally high mass-damping cases in the high-Reynolds number range. They showed that the cylinder response is hysteretic in the domain where the vortex structure changes. Singh and Mittal [72] and Prasanth and Mittal [88] observed a similar phenomenon for low Reynolds numbers using a numerical approach. As was shown previously, the vortex structure changes abruptly at the boundary where the motion trajectory switches (at around $U^*\mathrm{St} = 0.97$ for $K \cong 40.7$), which suggests the occurrence of a hysteresis loop. In order to investigate whether this hysteresis loop exists in the vicinity of $U^*\mathrm{St} \cong 0.97$ for $K \cong 40.7$, different types of computations are carried out:

(a) **Direct computations**, where the cylinder is initially at rest, and it impulsively starts to oscillate at the beginning of the computation. The Reynolds number is fixed during the computation.

(b) **Increasing-Re computations**. First, a direct step is carried out at a given combination of Re, U^*, m^* and ζ. The velocity and the pressure fields obtained at the end of the direct step are used as initial conditions in the next step, where the Reynolds number and the reduced velocity are increased by $\Delta\mathrm{Re}$ and $\Delta U^* = \Delta\mathrm{Re}/K$, respectively. As suggested by [58], the reduced velocity increment is set to $\Delta U^* = 0.02$. This process is repeated until the required number of steps are completed;

(c) **Decreasing-Re computations**. This approach is very similar to the previous one, but the Reynolds number and the reduced velocity are decreased accordingly.

In Fig. 4.13a $x_{0'}$ obtained from the increasing Re and the decreasing Re computations and those from the direct computations are plotted against $U^*\mathrm{St}$. In Figs. 4.13b-4.13e the cylinder paths are shown at different $U^*\mathrm{St}$ values, where I and D (in the top-left corner) refer to increasing or decreasing Reynolds numbers (and reduced velocities), respectively. It can be observed that different solutions can be obtained when Re is increased or decreased. As seen, raindrop-shaped motion develops for increasing Re (see Fig. 4.13c), and

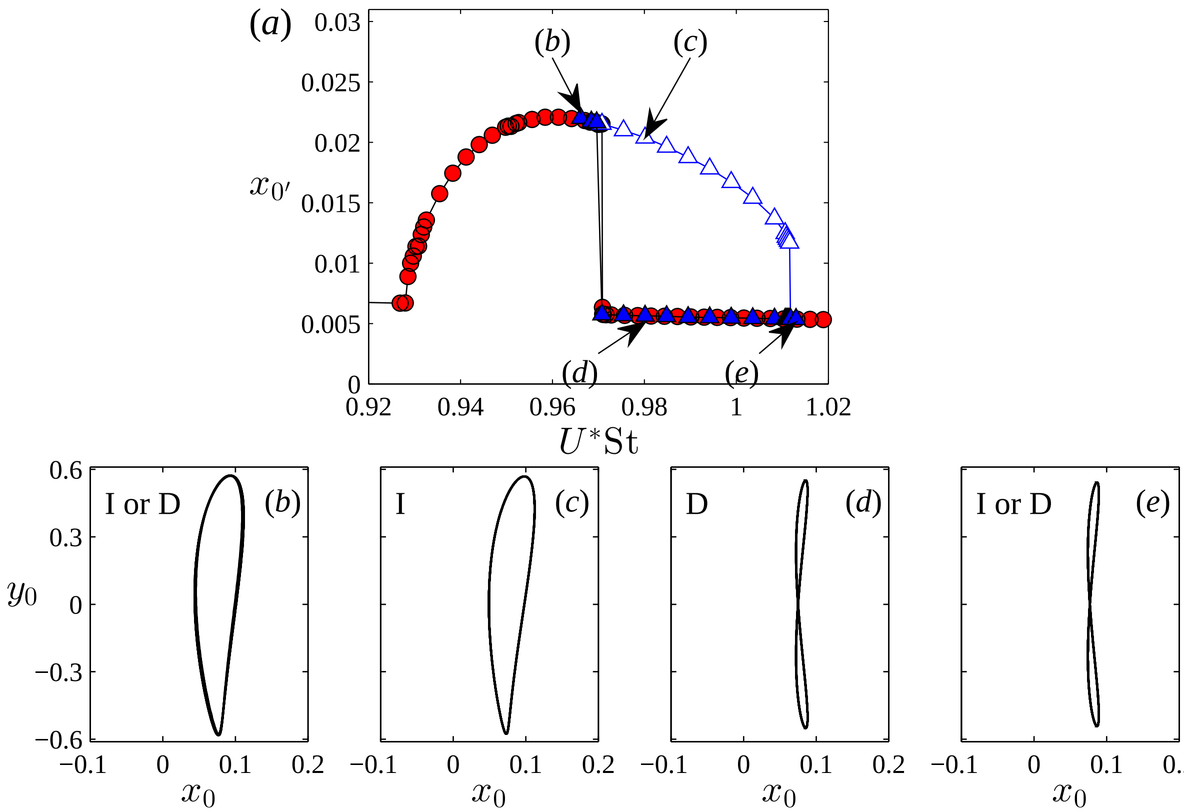

Figure 4.13: Root-mean-square values of streamwise cylinder displacement obtained from the direct computations (-●-), the increasing Re computations (-△-), and the decreasing Re computations (-▲-) against $U^*\mathrm{St}$ for $K \cong 40.7$ (a), and the cylinder paths for increasing and decreasing Re cases at $U^*\mathrm{St} \cong 0.9661$ (b), 0.9802 (c and d) and 1.0129 (e). Here I and D refer to increasing and deceasing Re (and U^*) values, respectively

distorted figure-eight paths are found for decreasing Re cases (see Fig. 4.13d) in the range of $0.97 < U^*\mathrm{St} \leq 1.01$. Below $U^*\mathrm{St} = 0.97$ raindrop-shaped paths are found and above $U^*\mathrm{St} = 1.01$ distorted figure-eight motions are observed for both increasing and decreasing Reynolds number cases (see Figs. 4.13b and 4.13e).

In Fig. 4.14 the vortex structures are shown at the same $U^*\mathrm{St}$ values, where the motion trajectories were analyzed in Fig. 4.13. Wake modes corresponding to increasing Reynolds numbers are shown in the top row, while the decreasing Re cases are shown in the bottom row. As in the figure, within the hysteresis domain (between $U^*\mathrm{St} = 0.97$ and 1.01) P+S wake modes are observed for increasing Re computations and 2S vortex structures are found for decreasing Re cases (see Fig. 4.14b). Outside of the hysteresis range the same vortex structures are obtained by either increasing or decreasing the Reynolds number (see Fig. 4.14a and 4.14c).

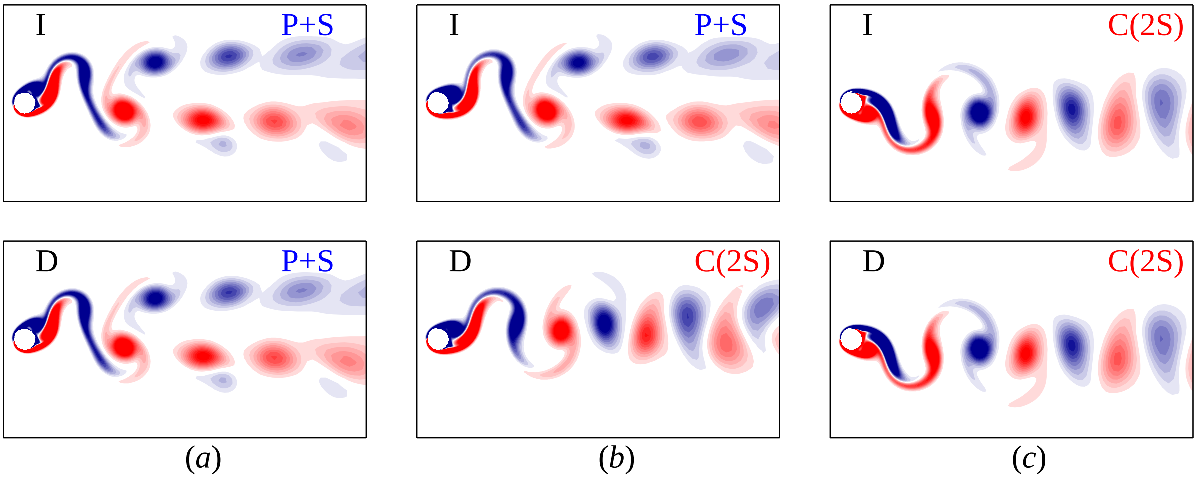

Figure 4.14: Vorticity contours in case of increasing and decreasing Re and U^* at $U^*\mathrm{St} \cong 0.9661$ (a), 0.9802 (b) and 1.0129 (c) for $K \cong 40.7$. Each vortex contours are recorded at random phases of the cylinder oscillation

Systematic computations are carried out to investigate the effects of dimensionless natural frequency on the cylinder path. In Fig. 4.15 $x_{0'}$ is plotted against $U^*\mathrm{St}$ for different K values ranging from $K \cong 34.7$ to 43.7. Values at around 0.007 are for the distorted-figure-eight paths, while higher $x_{0'}$ values indicate raindrop-shaped motion. It can be seen that $K \cong 36.6$ is the lowest dimensionless natural frequency value where both raindrop-shaped and distorted figure-eight motions can occur. Varying K between $K \cong 36.6$ and 43.7, raindrop-shaped motion occurs over a narrow $U^*\mathrm{St}$ domain that widens with increasing the dimensionless natural frequency. It is also shown in Fig. 4.15 that the $x_{0'}$ curves shift upwards and the location of the jump which separates the raindrop-shaped and the distorted-figure-eight motion ranges decreases with the dimensionless natural frequency.

4.2.2 Analysis of fluid force coefficients

In order to show additional differences between the effects caused by the P+S and the 2S vortex structures, the frequency spectra of transverse and streamwise fluid force coefficients are investigated. Figure 4.16 shows the frequency spectra of C_y and C_x at the same $U^*\mathrm{St}$ values where the cylinder paths and the vortex structures were previously analyzed (see Fig. 4.12). The blue and the red curves stand for the FFT spectra of transverse and streamwise fluid forces, respectively. It can be seen that both force coefficients contain two significant frequency peaks at the $U^*\mathrm{St}$ values where 2S vortex structures are found (see Figs. 4.16a and 4.16d). In the FFT of transverse fluid force the first and the third harmonic frequency components are found, and in streamwise fluid force the second and

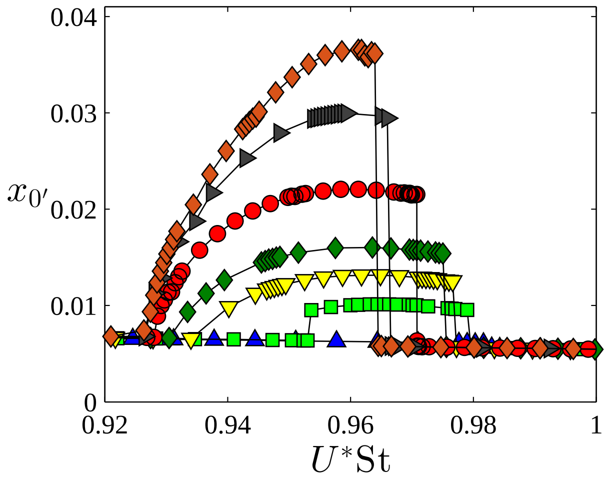

Figure 4.15: Root-mean-square values of streamwise cylinder displacement against U^*St for $K \cong 34.7$ (▲), 36.6 (■), 37.6 (▼), 38.6 (◆), 40.7 (●), 42.7 (◀) and 43.7 (◆)

the fourth harmonic components are identified with high PSD values. Prasanth and Mittal [88] found a jump in the phase difference between C_y and y_0 in the lower branch. They showed that in the vicinity of the switch $f/f_N \cong 3$ was much more significant in the spectrum of transverse fluid force than the frequency component coinciding with the transverse vibration frequency. The experimental data of Dahl et al. [41, 82] also showed this dual resonance effect. In addition, they found that $f/f_N \cong 3$ in the spectra of C_y influenced the first harmonic component. It can also be seen in Figs. 4.16a and 4.16d (where distorted figure-eight motions are identified) that the frequency peaks in the spectra of transverse and streamwise fluid force coefficients do not overlap. This finding is the same what I showed earlier for the Fast Fourier spectra of the vibration components in Figs. 4.12a and 4.12d.

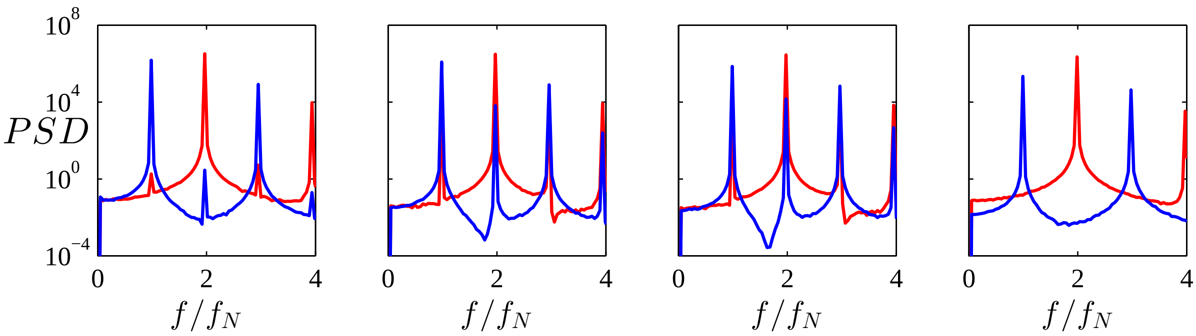

Figure 4.16: Frequency spectra of transverse and streamwise fluid force (red and blue curves) at $U^*\text{St} = 0.9154$ (a), 0.9441 (b), 0.9708 (c) and 0.9757 (d) for $K = 40.7$

Figures 4.16b and 4.16c show the FFT spectra of C_y and C_x at the U^*St values where P+S asymmetric wake modes are identified. It can be seen that the location of the high-intensity frequency peaks of transverse and streamwise fluid force components overlap. In contrast to those observed during the spectral analyses of the vibration components (see Figs. 4.12b and 4.12c), $f/f_N \cong 1, 2, 3$ and 4 occur with remarkable PSD values in the spectra of both transverse and streamwise fluid forces.

Baranyi [46] investigated the effect of forcing frequency in case of figure-eight cylinder motion. Post-processing the data in [46], we found that in case of 2S vortex structures the FFT spectra of C_y and C_x did not overlap (similar to Figs. 4.16a and 4.16d), while the frequency peaks of transverse and streamwise fluid forces collapsed where P+S wake mode was observed (as in Figs. 4.16b and 4.16c). Therefore, the current results for free vibration and those obtained using the data of Baranyi [46] for forced cylinder motion are in *good qualitative agreement*. Good qualitative agreement is also found with the computations of Bao et al. [83], who observed P+S wake mode at only one parameter combination, and where the frequency spectra of C_y and C_x showed similarities to those seen in Figs. 4.16b and 4.16c.

Figure 4.17a shows the time-mean values of transverse fluid force coefficient $\overline{C}_y$ against U^*St for $K \cong 37.6, 40.7$ and 43.7. The results show similar features for all of the investigated K values, so only three curves are presented here to avoid confusion. It can be seen that $\overline{C}_y$ is negligible in the range where distorted figure-eight motion is found. As was shown earlier, P+S vortex structure is observed for orbital cylinder trajectories (see Figs. 4.12b and 4.12c). Since this wake mode means an asymmetric load on the structure, $|\overline{C}_y| > 0$ in raindrop-shaped motion cases, which is seen in Fig. 4.17a. Blackburn and Henderson [30] and Baranyi [46], using the forced vibration models, found also that $\overline{C}_y$ is non-zero for cases where the P+S asymmetric vortex structures are found.

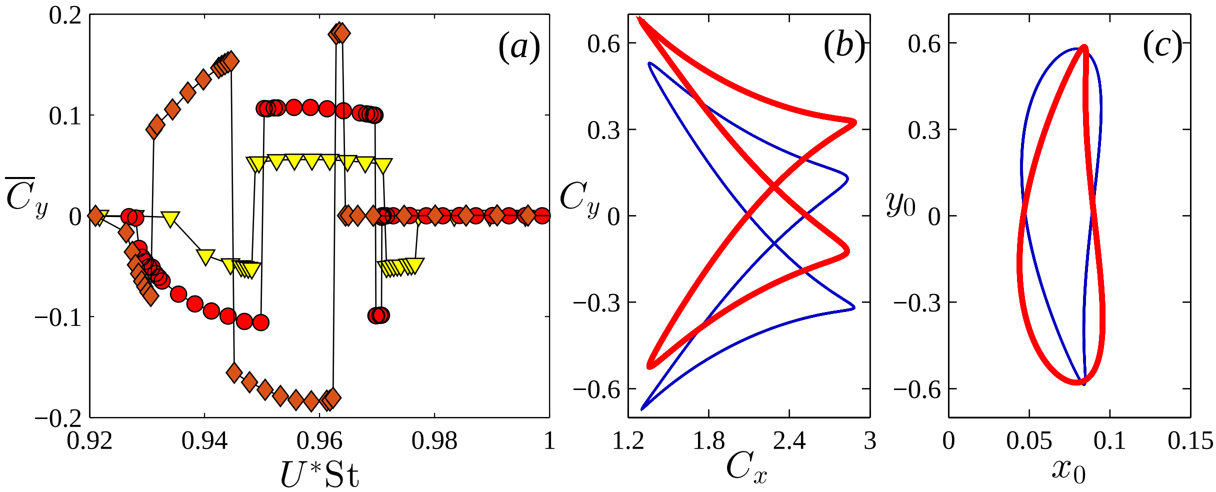

Figure 4.17: Time mean values of transverse fluid force against U^*St for $K \cong 37.6$ (–▽–), 40.7 (–●–) and 43.7 (–◆–) (a), and (C_x, C_y) (b) and (x_0, y_0) (c) limit cycle curves in pre- and post-jump cases (red thick curve: $U^*\text{St} = 0.930$; blue thin curve: $U^*\text{St} = 0.931$) for $K \cong 43.7$

In the raindrop-shaped-motion domain two state curves exist, and the solution jumps abruptly between them. In Fig. 4.17b (C_x, C_y) limit cycle curves are shown before and after a jump. The curves appear to be mirror images of each other, which is due to a symmetry breaking bifurcation [99]. In a nonlinear system there are two attractors, each with a basin of attraction [99]. If the set of parameters (e.g. Re, U^*, m^*, etc.) is close to the boundary separating the basins of attraction then a tiny change can lead to an abrupt jump (see Fig. 4.17a). In Fig. 4.17c the paths of the cylinder are shown in the pre- and post-jump cases. It can be seen that these curves are also appear to be mirror images of each other.

Figures 4.18a and 4.18b show the rms values of streamwise and transverse fluid force coefficients $C_{x'}$ and $C_{y'}$ against U^*St for $K \cong 37.6, 40.7$ and 43.7. The results show similar features for all of the investigated dimensionless natural frequency values, so only three curves are presented here to avoid confusion. Both $C_{x'}$ and $C_{y'}$ show jumps at the upper boundary separating raindrop-shaped and distorted figure-eight motion domains, as can also be seen in $x_{0'}$ (see Fig. 4.15). It can be observed that $C_{x'}$ curves belonging to increasing K values shift to higher values in both the raindrop-shaped and figure-eight motion domains. In contrast, by increasing K the $C_{y'}$ curves shift upwards in the raindrop-shaped and downwards in the figure-eight motion domains.

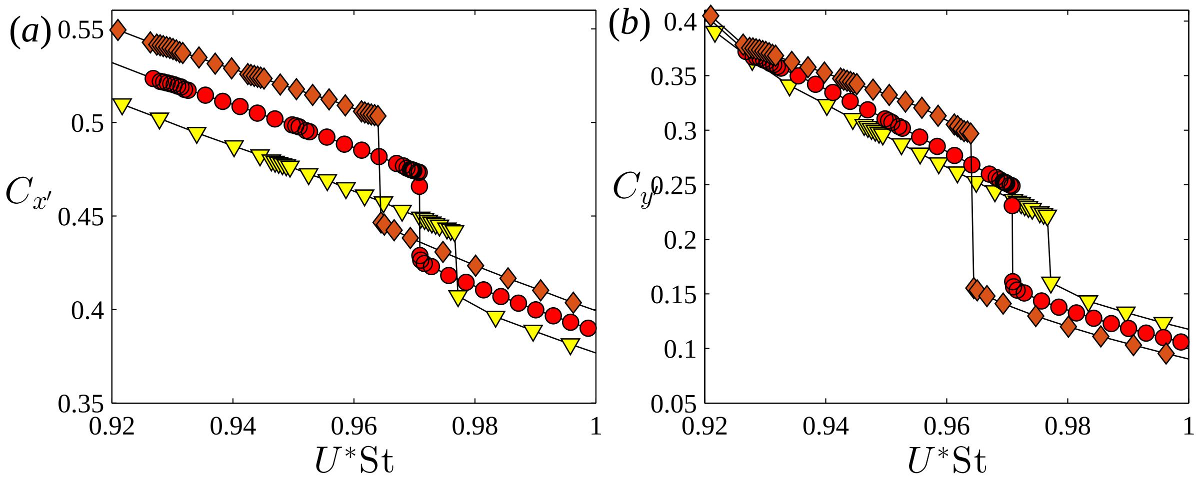

Figure 4.18: Root-mean-square values of stremawise (a) and transverse (b) fluid forces against U^*St for $K \cong 37.6$ (-▽-), 40.7 (-●-) and 43.7 (-◆-)

4.3 New scientific contributions

Contribution I

Systematic computations are carried out for two-degree-of-freedom vortex-induced vibrations at different non-dimensional natural frequency values from $K = 12.3$ to 34.7, and constant mass and structural damping ratios of $m^* = 10$ and $\zeta = 0\%$, respectively ($\mathrm{Re} = 60 - 250$). I found that

(a) Plotting the data set belonging to different K values against U^*St makes the comparison easier than using Re as an independent parameter;

(b) Local peak values are found in the rms of streamwise cylinder displacement $x_{0'}$, and streamwise fluid force coefficient $C_{x'}$ at around $U^*\mathrm{St} = 0.47$. The local maximum values in $x_{0'}$ and $C_{x'}$ are found to increase with K;

(c) $C_{x'}$ approaches zero in the vicinity of $U^*\mathrm{St} = 0.5$, at the same location, where the phase difference of C_x relative to x_0 changes suddenly from 0° to 180°;

(d) While the phase angle between the pressure streamwise fluid force C_{xp} and the cylinder displacement suddenly shifts from 0° to 180° at $U^*\mathrm{St} \cong 0.5$, the phase difference of the viscous streamwise fluid force C_{xv} relative to the cylinder motion is initially at $\sim 35°$, which increases slowly to 180°. These findings indicate that the pressure component of the streamwise fluid force is responsible for the abrupt phase change between C_x and x_0. Due to the sudden change in the phase angle between C_{xp} and x_0, the limit cycle curves (C_{xv}, C_{xp}) switch from clockwise to anticlockwise orientation at $U^*\mathrm{St} \cong 0.5$;

(e) The orientation of the cylinder path changes from clockwise to counterclockwise orbit (in the upper loop of the figure-eight) at around $U^*\mathrm{St} = 0.5$.

Related publications: Dorogi and Baranyi [J1]

Contribution II

Using two-degrees-of-freedom VIV computations at different non-dimensional natural frequency values in the range of $K = 34.7 - 43.7$, and constant mass and structural damping ratio values of $m^* = 10$ and $\zeta = 0\%$. I found that K highly influences the path of the cylinder. For dimensionless natural frequency values below $K \cong 36.6$ only distorted figure-eight motions are observed. Between the values of $K \cong 36.6$ and 43.7, besides figure-eight paths, orbital cylinder trajectories (i.e. raindrop-shaped orbits) are identified in a thin U^*St domain (e.g. in $0.92 < U^*\mathrm{St} < 0.97$ for $K \cong 40.7$), which widens with K. In the range where raindrop-shaped motions are found, the rms values of the streamwise vibration component $x_{0'}$ is significantly higher (can exceed $x_{0'} = 0.023$) compared to the distorted figure-eight path domains (around $x_{0'} = 0.005$). I showed that as the non-dimensional natural frequency increases, the $x_{0'}$ curves shift upwards.

The frequency spectra of the streamwise vibration component for raindrop-shaped orbits contain two high-intensity frequency peaks corresponding to f_y^* and $2f_y^*$, where f_y^* is the transverse oscillation frequency of the cylinder. Due to the multi-frequency vibration, the raindrop-shaped paths are asymmetric. I found P+S asymmetrical vortex structures in the wake of the cylinder for raindrop-shaped motions, while 2S or C(2S) modes for distorted figure-eight motion cases. Here P and S refer to vortex pairs and single vortices shedding form the body, respectively, and C refers to the coalescence of the positive and negative vortices.

I identified abrupt changes in the rms values of streamwise and transverse vibration components and fluid force coefficients $(x_{0'}, y_{0'}, C_{x'}, C_{y'})$, which corresponds to the point, where (1) the cylinder path switches from raindrop-shaped to distorted figure-eight, and (2) the wake mode changes from P+S to 2S. I found a hysteresis loop close the boundary, where the vortex structure and the cylinder orbit switch. I showed that increasing the U^* (together with Re) in the range of $0.97 < U^* \leq 1.01$, orbital trajectories and P+S modes are formed. However, decreasing U^* (and Re) in the same domain, distorted figure-eight paths and 2S modes occur.

I found that the time-mean values of the transverse fluid force coefficient $\overline{C}_y$ is approximately zero for distorted figure-eight paths, while for raindrop-shaped trajectories $|\overline{C}_y| > 0$. Due to the nonlinearity of the fluid flow, $\overline{C}_y$ jumps abruptly between two solutions. Plotting the (C_x, C_y) and (x_0, y_0) limit cycles in the pre- and post-jump cases, I found that these curves are mirror images of each other; hence the two solutions of $\overline{C}_y$ are symmetric.

Related publications: Dorogi and Baranyi [J3], Dorogi and Baranyi [C7] and Dorogi and Baranyi [C8]

Chapter 5

Analyses of streamwise vortex-induced vibrations

As was mentioned in Section 1.1.2, the experimental findings of Tanida et al. [35], and the computational results of Konstantinidis and Bouris [36] and Kim and Choi [37] indicate that streamwise-only vortex-induced vibrations are not feasible at low Reynolds numbers.

However, Bourguet and Lo Jacono [79] investigated self-excited streamwise vibration of a rotating cylinder at $\mathrm{Re} = 100$. Their results obtained for the non-rotating case show a single-peak response, but the maximum oscillation amplitude is only 0.2% of the cylinder diameter.[1] In addition, the computational results from the 2DoF VIV computations presented in Chapter 4 and published in [J1], indicate that the root-mean-square values of streamwise vibration component $x_{0'}$ display a local maximum value at around $U^*\mathrm{St} = 0.47$. Since the transverse oscillation amplitude is negligible in this domain, we suspect that the peak value in $x_{0'}$ is resulted only by the streamwise vibration component. For this reason, the following research questions is addressed:

Is it possible for streamwise-only VIV to occur in the low-Re domain? What are the effects of m^* and Re on the cylinder response?

In order to answer these questions two sets of computations are carried out. First, computations are performed at the mass ratio values $m^* = 2, 5, 10$ and 20, while keeping the Reynolds number constant at $\mathrm{Re} = 180$. The results of these investigations are presented in Section 5.1. A model based on harmonic assumptions is used to explain the phenomenon observed in the numerical results. Second, computations are carried out at different Reynolds numbers ($\mathrm{Re} = 100, 180, 200$ and 250), while keeping mass ratio constant at $m^* = 10$, which results are discussed in Section 5.2. In both sets of computations the reduced velocity is varied between $U^* = 1.5$ and 3.5, while the structural damping ratio is fixed at zero.

5.1 The effect of mass ratio

In this section streamwise-only vortex-induced vibrations are investigated at different mass ratio values of $m^* = 2, 5, 10$ and 20. The Reynolds number and the structural damping ratio values are fixed at $\mathrm{Re} = 180$ and $\zeta = 0\%$, respectively, while the reduced velocity is varied between $U^* = 1.5$ and 3.5.

Figure 5.1 shows the dimensionless oscillation amplitude $\hat{x}_0$ (see Figs. 5.1a and 5.1c), and the non-dimensional vibration frequency f_x^* (Figs. 5.1b and 5.1d) against the reduced

[1] Note that the results obtained by Bourguet and Lo Jacono [79] have been previously used for validation purposes; good agreement was found (see the results in Section 3.3).

velocity for different m^* values. It can be seen that the cylinder response displays a single excitation region with a peak oscillation amplitude of approximately 1.1% of the cylinder diameter for all mass ratios investigated. As can be observed, $\hat{x}_0$ increases gradually up its peak value, and than it decreases monotonically. Although the maximum vibration amplitude seems to be independent of the mass ratio, the U^* value where the maximum in $\hat{x}_0$ is identified increases with m^*. The root-mean-square values of streamwise cylinder displacement $x_{0'}$ obtained from the 2DoF VIV computations show similar trends in the range of $0.4 < U^*\mathrm{St} < 0.6$ (see Section 4.1); a local peak value is observed in $x_{0'}$ at around $U^*\mathrm{St} = 0.47$. In that case the local maximum value increased, because the Reynolds numbers corresponding to the peak $x_{0'}$ values increased.

The dimensionless vibration frequency (see Figs. 5.1b and 5.1d) shows an opposite behavior: f_x^* decreases to its minimum point, which occurs approximately at the same U^* value where the peak amplitude is observed. Beyond the minimum point, f_x^* increases asymptotically to a value corresponding to the double of the Strouhal number for a stationary cylinder [$2\mathrm{St} \cong 0.383$ at $\mathrm{Re} = 180$ using Eq. (1.8) obtained by [17]]. In other words, in the excitation region the dimensionless vibration frequency of the cylinder is always lower than the double of the Strouhal number, i.e. $f_x^* < 2\mathrm{St}$. This finding is consistent with the forced vibration results obtained by Nishihara et al. [1] and Konstantinidis and Liang [100], who showed that streamwise-only VIV due to alternating vortex shedding can occur only for $f_x^* < 2\mathrm{St}$.

It can also be observed in Fig. 5.1 that as we increase the mass ratio, the width of the excitation region diminishes, i.e. the rate of change of $\hat{x}_0$ and f_x^* becomes faster. In particular, for $m^* = 20$, the oscillation amplitude and frequency show sudden changes at $U^* = 2.614$, at the same point where the peak response is observed (see Figs. 5.1c and 5.1d).

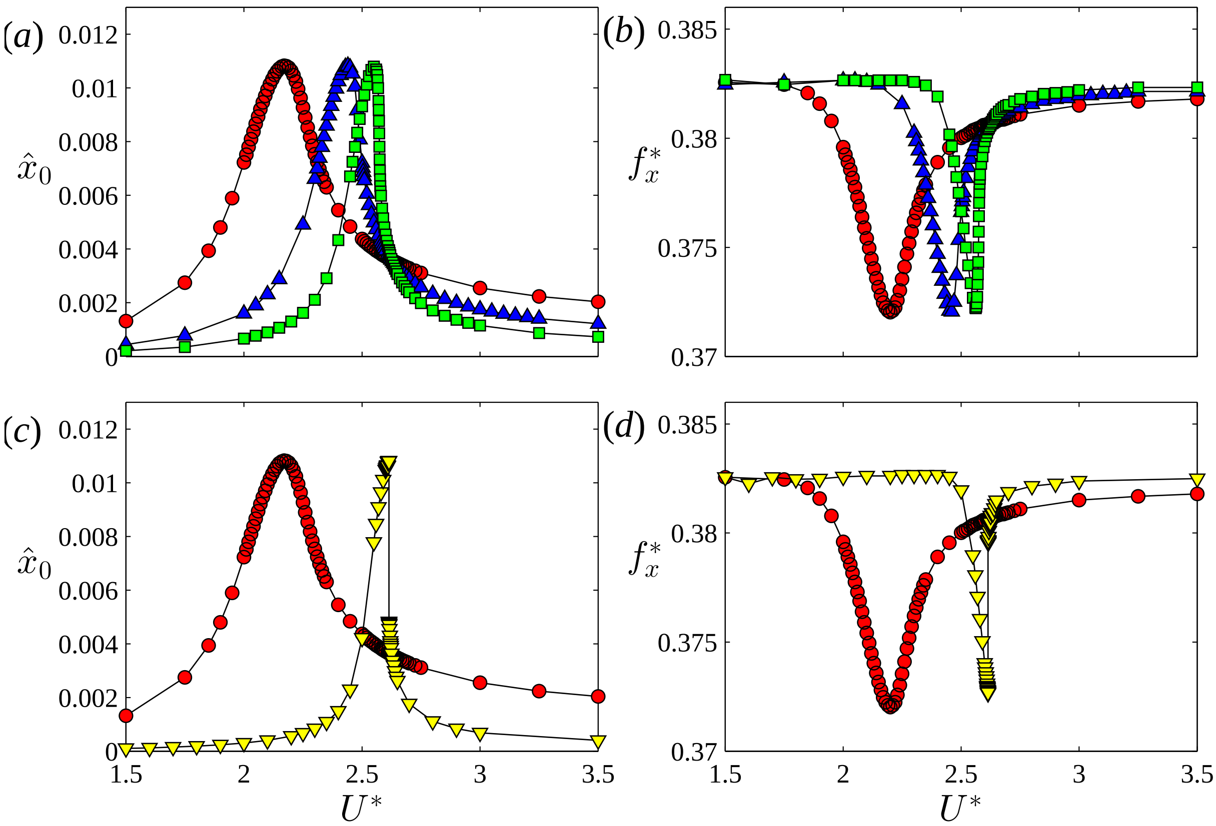

Figure 5.1: Dimensionless oscillation amplitude (a and c) and frequency (b and d) against reduced velocity for different mass ratio values at $\mathrm{Re} = 180$. $m^* = 2$, –●–; 5, –▲–; 10, –■–; 20, –▼–

Aguirre [75], Okajima et al. [76] and Cagney and Balabani [77] investigated experimentally streamwise-only vortex-induced vibrations. Their results at moderately high Reynolds numbers reveal that two excitation regions (branches) occur. The first branch is associated with a symmetrical mode of vortex shedding, while in the second branch an alternating vortex shedding mode[2] is observed. Figure 5.2 shows the vorticity contours at the corresponding combinations of m^* and U^*, where the peak responses (maximum oscillation amplitude and minimum vibration frequency) occur. It can be seen that, irrespective of m^*, only alternating modes of vortex shedding are found. This suggest that the single excitation region shown in Fig. 5.1 corresponds to the second branch. The experimental results at moderately high Re show also that symmetrical mode of vortex shedding develops only for $\hat{x}_0 > 0.1$ cases. The peak oscillation amplitude for Re = 180 is only 0.011, which is not sufficiently high for the symmetrical vortex shedding mode. Consequently, the absence of the first branch at Re = 180 is expected.

In Fig. 5.3 the amplitude of streamwise fluid force coefficient $\hat{C}_x$ is plotted against U^* for different m^* values. As can be seen, $\hat{C}_x$ follows similar trends for all mass ratios. Initially, $\hat{C}_x$ increases gradually with U^* reaching a peak level near the point where peak amplitudes of cylinder oscillation occur (see Fig. 5.1a and Fig. 5.1c). Despite the peak

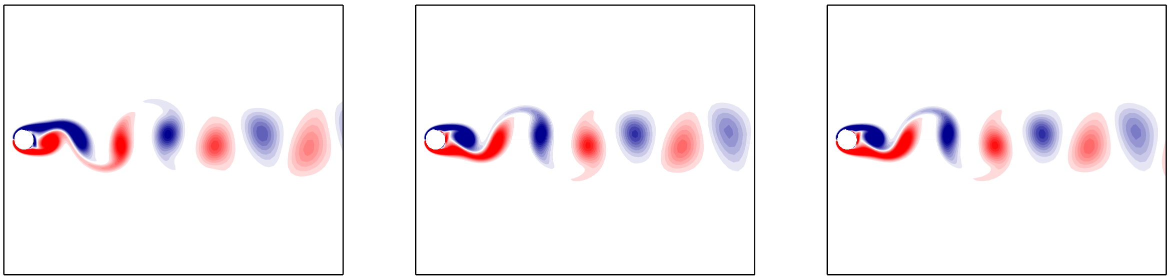

(a) (b) (c)

Figure 5.2: Vorticity contours (red: positive, blue: negative) at the peak amplitude points $(m^*, U^*) = (2, 2.17)$ (a) $(10, 2.55)$ (b) and $(20, 2.614)$ (c) for Re = 180. Each vortex contours are recorded at random phases of the cylinder oscillation

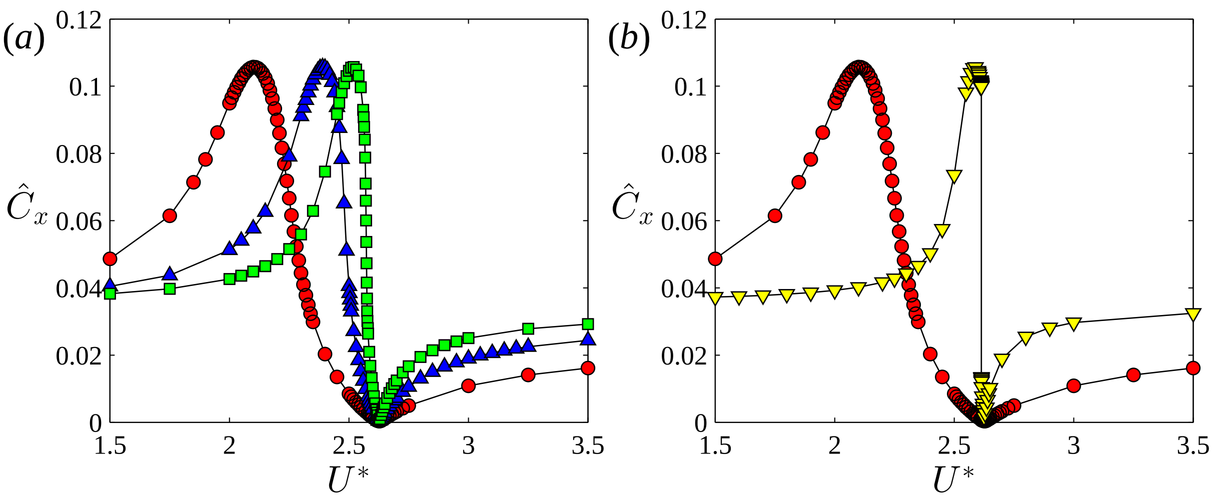

Figure 5.3: Amplitude of streamwise fluid force coefficient against reduced velocity for different mass ratio values at Re = 180. $m^* = 2$, -●-; 5, -▲-; 10, -■-; 20, -▽-

[2]Similar to the Kármán vortex street. Using the notations introduced by Williamson and Roshko [28], alternating vortex shedding mode is referred to as 2S mode. However, in terms of streamwise-only VIV, the terminology *alternating mode of vortex shedding* is more preferred than the *2S mode*.

vibration amplitude is only $\hat{x}_0 = 0.011$, the maximum $\hat{C}_x$ is around 0.106, which is roughly three times higher than the value obtained for a stationary cylinder. After the maximum point, a steep decrease of $\hat{C}_x$ within a narrow range of U^* is observed at the end of which it approaches zero; $\hat{C}_x \to 0$ at $U^* \cong 2.625$. Note that the results obtained from the two-degree-of-freedom VIV computations, presented in Section 4.1 show a somewhat similar effect; as seen in Fig. 4.3, $\hat{C}_{x'} \to 0$ at around $U^*\mathrm{St} = 0.5$. It is also seen in Fig. 5.3 that beyond the point where $\hat{C}_x \to 0$ the amplitude of the streamwise fluid force coefficient increases gradually. Similar to the tendencies observed in the non-dimensional oscillation amplitude and frequency (see Fig. 5.1), $\hat{C}_x$ found to jump at $U^* = 2.614$ for $m^* = 20$, closely after the reduced velocity value where the peak value in $\hat{C}_x$ is identified (see Fig. 5.3b).

In order to investigate the phenomenon $\hat{C}_x \to 0$ more in depth, a model based on harmonic assumptions (often called harmonic oscillator model) is used. Let us assume that the cylinder displacement and the streamwise fluid force coefficient are sinusoidal functions of time:

$$\begin{aligned} x_0(t) &= \hat{x}_0 \sin 2\pi f_x^* t, && (5.1)\\ C_x(t) &= \hat{C}_x \sin(2\pi f_x^* t + \Phi_x), && (5.2)\end{aligned}$$

where Φ_x is the phase difference of streamwise fluid force relative to the cylinder displacement (i.e. the streamwise phase). Similar to Eqs. (4.4) and (4.5), the mean components of $x_0(t)$ and $C_x(t)$ are omitted, because they do not affect the dynamics. The differentiation of $x_0(t)$ with respect to time result in the following formulæ for the time-varying velocity $\dot{x}_0(t)$ and acceleration $\ddot{x}_0(t)$ of the cylinder:

$$\begin{aligned} \dot{x}_0(t) &= 2\pi f_x^* \hat{x}_0 \cos 2\pi f_x^* t, && (5.3)\\ \ddot{x}_0(t) &= -4\pi^2 f_x^{*2} \hat{x}_0 \sin 2\pi f_x^* t. && (5.4)\end{aligned}$$

Substituting Eqs. (5.1)-(5.4) into the cylinder equation of motion [Eq. (2.12)], the following equation is obtained:

$$\begin{aligned} &-4\pi^2 f_x^{*2} \hat{x}_0 \sin(2\pi f_x^* t) + \frac{8\pi^2 f_x^* \hat{x}_0 \zeta}{U^*} \cos(2\pi f_x^* t) + \frac{4\pi^2 \hat{x}_0}{U^{*2}} \sin(2\pi f_x^* t) \\ &= \frac{2\hat{C}_x}{\pi m^*} \left[\sin(2\pi f_x^* t) \cos \Phi_x + \cos(2\pi f_x^* t) \sin \Phi_x\right]. \end{aligned} \qquad (5.5)$$

Equating the sine and cosine terms in this equation the following expressions can be obtained:

$$\begin{aligned} \cos \Phi_x &= \frac{2\pi^3 m^* \hat{x}_0}{\hat{C}_x U^{*2}} (1 - f_x^{*2} U^{*2}), && (5.6)\\ \sin \Phi_x &= \frac{4\pi^3 m^* \zeta \hat{x}_0}{\hat{C}_x U^*} f_x^*. && (5.7)\end{aligned}$$

Adding the squares of Eqs. (5.6) and (5.7), and expressing the amplitude of streamwise fluid force coefficient the following formula is resulted in:

$$\hat{C}_x = \frac{2\pi^3 m^* \hat{x}_0}{U^{*2}} \sqrt{(1 - f_x^{*2} U^{*2})^2 + 4\zeta^2 f_x^{*2} U^{*2}}. \qquad (5.8)$$

Substituting zero structural damping ratio $\zeta = 0\%$ into Eq. (5.8), it can be seen that $\hat{C}_x = 0$ at the point where the frequency of cylinder vibration coincides with the natural frequency of the system in vacuum, i.e. at $f_x^* U^* = 1$. Table 5.1 shows f_x^* and $f_x^* U^*$ at different reduced velocity values for $m^* = 10$. It can be observed that $f_x^* U^*$ is very close to unity at $U^* = 2.625$, at the same point where the amplitude of streamwise fluid force coefficient approaches zero (see Fig. 5.3).

Table 5.1: The f_x^* and $f_x^* U^*$ for different reduced velocity values close to the point where $\hat{C}_x \to 0$ for $m^* = 10$ and Re = 180

	U^*				
	2.618	2.62	2.625	2.63	2.635
f_x^*	0.3805	0.3806	0.3807	0.3808	0.3809
$f_x^* U^*$	0.9961	0.9972	0.9993	1.0015	1.0037

Besides, Eq. (5.7) shows that for $\zeta = 0\%$ $\sin \Phi_x = 0$, therefore Eq. (5.6) can results in only $\Phi_x = 0°$ and $180°$ values; hence the cylinder displacement can be only in-phase or out-of-phase with the streamwise fluid force coefficient. In Fig. 5.4 Φ_x[3] is plotted against the reduced velocity for different m^* values. This figure seems to confirm the above mentioned criteria, Φ_x jumps between approximately 0° and 180° at around $U^* = 2.625$ for all mass ratio values.

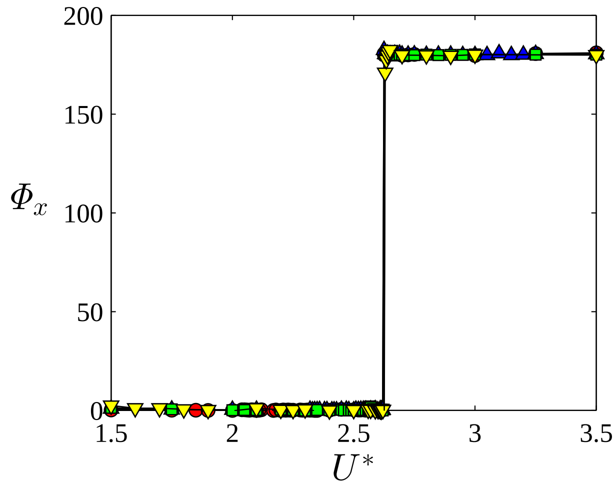

Figure 5.4: Phase difference of streamwise fluid force relative to cylinder displacement against the reduced velocity for $m^* = 2$ (red circle), 5 (blue triangle), 10 (green square) and 20 (yellow inverted triangle) at Re = 180

It is very important to see in Fig. 5.1 that the dimensionless oscillation amplitude shows a non-zero value at the point where $\hat{C}_x$ reaches zero. The question arises how can the unsteady streamwise fluid force with approximately zero fluctuation result in finite amplitude of cylinder oscillation. Figure 5.5 shows the relative waveforms of the cylinder displacement x_0^* and streamwise fluid force C_x^* [defined by Eqs. (4.2) and (4.3)], and the frequency spectra of C_x at different U^* values for $m^* = 2$. It can be seen that, while x_0^* is harmonic, the streamwise fluid force shows a strongly non-harmonic behavior in the vicinity of the point where $\hat{C}_x \to 0$. As seen in the Fast Fourier spectra of C_x, a frequency component with the double of the cylinder's vibration frequency $2f_x^*$ (i.e. the second harmonic component) appears. It can be observed that the intensity of $2f_x^*$ increases with

[3] The computation methodology of Φ_x is shown in Appendix A.2.1.

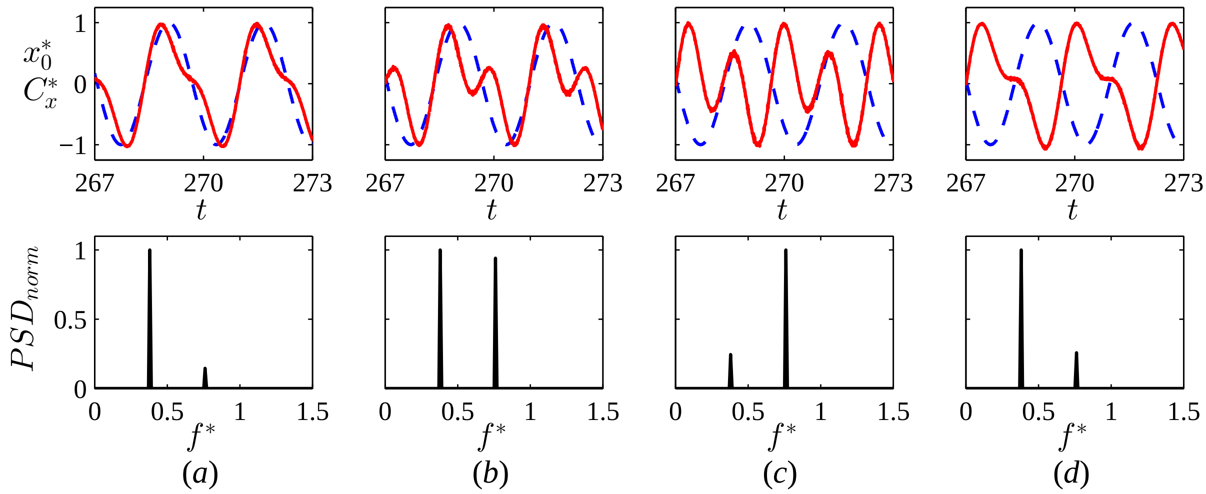

Figure 5.5: The relative waveforms (top plots) of streamwise cylinder displacement (x_0^*, blue dashed lines) and streamwise fluid force (C_x^*, red solid lines), and the frequency spectra of streamwise fluid force (bottom plots) for $U^* = 2.61$ (a), 2.62 (b), 2.63 (c) and 2.64 (d) at $m^* = 2$ and $\mathrm{Re} = 180$

the reduced velocity towards the point of $f_x^* U^* = 1$. At the point where the vibration frequency is the closest to the natural frequency of the system, at $U^* = 2.63$, the $2f_x^*$ peak is the most dominant in the spectra, the intensity of the f_x^* frequency component is very low. This result indicates that, vortex-induced vibrations at around $f_x^* U^* = 1$ is highly nonlinear, and the mechanical energy is transferred from the fluid to the cylinder across different harmonic components.

Figure 5.6 shows the amplitude of transverse fluid force $\hat{C}_y$ against U^* for different mass ratio values between $m^* = 2$ and 20. As can be seen, $\hat{C}_y$ displays comparable tendencies at all m^* values, similarly to $\hat{C}_x$ (see Fig. 5.3). At the beginning, $\hat{C}_y$ increases monotonically up to its peak value, which is followed by a rapid decrease. Beyond the minimum point $\hat{C}_y$ increases gradually. It can be seen that increasing the mass ratio, the maximum and minimum points of $\hat{C}_y$ shift towards increasing U^* values. In contrast to the findings concerning the amplitude of streamwise fluid force coefficient, the maximum and minimum $\hat{C}_y$ values are only 6% higher and 5% lower, respectively, than the value

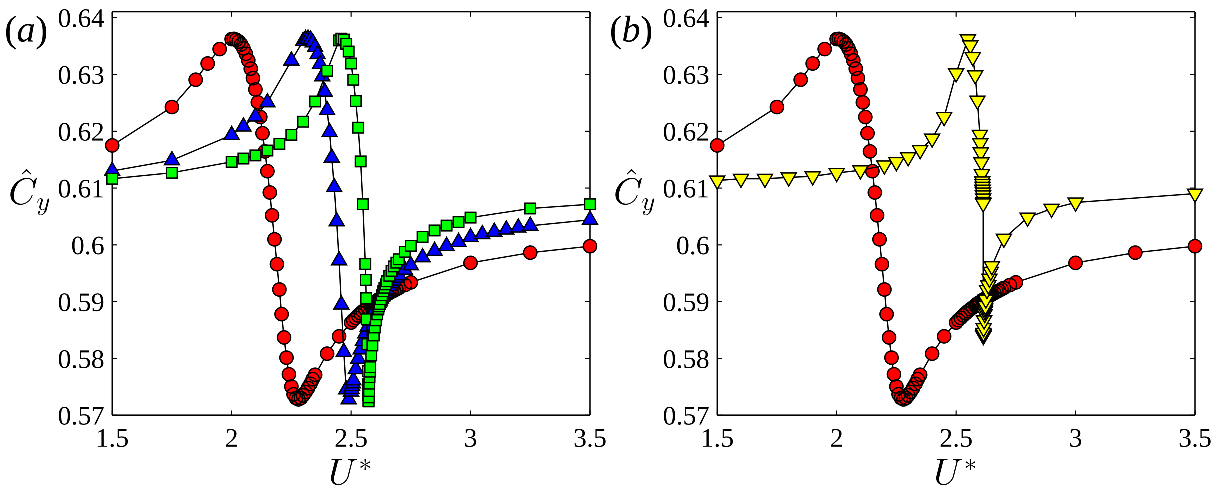

Figure 5.6: Amplitude of transverse fluid force coefficient against reduced velocity for different mass ratio values at $\mathrm{Re} = 180$. $m^* = 2$, -●-; 5, -▲-; 10, -■-; 20, -▼-

obtained for a stationary cylinder. Note that, the minimum point observed for $m^* = 20$ is an exception, it is only 3% lower than the corresponding value for a stationary cylinder. Since the body oscillates only streamwise with the free stream, there is no inertial force in the transverse direction, which could result in larger changes in $\hat{C}_y$. For this reason, the variations of $\hat{C}_y$ can only be caused by the changes in the vortex dynamics. As can be seen in Fig. 5.2 no significant change can be observed in the vortex shedding, so that, a small variation in $\hat{C}_y$ is expected.

Similarly to the time history of C_x, let us assume that the transverse fluid force coefficient can be represented as a harmonic function of time:

$$C_y(t) = \hat{C}_y \sin(\pi f_x^* t + \Phi_y), \tag{5.9}$$

where Φ_y is the phase difference of transverse fluid force relative to the cylinder displacement. Note that the frequency of C_y is $f_x^*/2$, hence the phase difference value is meaningful in the range of $0° \leq \Phi_y \leq 180°$. In Fig. 5.7 Φ_y is shown against the reduced velocity for different m^* values. Unlike Φ_x which is restricted to the values of 0° and 180° for $\zeta = 0\%$ [Eqs. (5.6) and (5.7)], Φ_y shows a smooth variation between approximately 20° to 110°. It was shown earlier that as the mass ratio is increased the width of the excitation range decreases (see Fig. 5.1), consequently, the rate of change for Φ_y increases (Fig. 5.7). Moreover, at $U^* = 2.614$ for $m^* = 20$ Φ_y jumps abruptly from $\Phi_y = 56.5°$ to 93.4°.

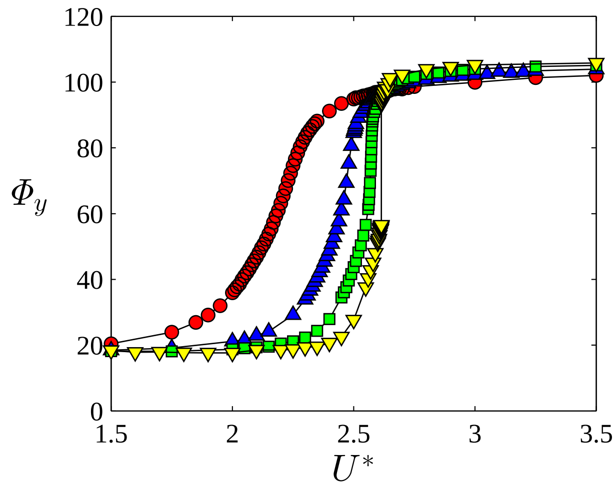

Figure 5.7: Phase difference of transverse fluid force relative to the cylinder displacement for $m^* = 2$ (-●-), 5 (-▲-), 10 (-■-) and 20 (-▼-) at Re = 180

Konstantinidis et al. [101] investigated the flow around a stationary cylinder placed into a free stream upon which a periodic velocity oscillation (perturbation) is superimposed. They measured the unsteady transverse velocity component, and calculated the phase difference of this velocity component with respect to the in-flow velocity. Note that this phase angle value is similar to the Φ_y applied in this study. Konstantinidis et al. [101] found that increasing the frequency of velocity perturbation the phase difference value increases. They attributed this effect to the shift in the timing of vortex shedding[4]. Since the case investigated in [101] is kinematically equivalent with the streamwise-only vortex-induced vibration of a circular cylinder analyzed in the chapter, the gradual increase observed in Φ_y (Fig. 5.7) may be attributed also to the shift in the timing of vortex shedding.

Konstantinidis et al. [101] calculated also the vortex strength Γ based on the velocity fields obtained using the Digital Particle Image Velocimetry technique. They showed that

[4]"... the phase at which a vortex pinches off from the cylinder with respect to the inflow velocity oscillation" (see [101], p. 48.)

Γ increases up to the point (time instant), where a vortex is shed from the cylinder. At this instant Γ shows a sudden drop. In terms of transverse fluid force (obtained from the present CFD simulations), increasing vortex strength means increasing C_y, which reaches its maximum (or minimum) value at the same point where Γ is at its maximum, i.e. at the time instant where a vortex (negative or positive) is shed from the body. In other words, the time instant of vortex shedding can be determined from the time history of the transverse fluid force. Negative or positive vortices are shed from the body at the points, where C_y reaches its maximum or minimum, respectively.

Figure 5.8 shows the vorticity distributions at the time instants corresponding to the positive extreme point (top row) and the zero cross-over point (middle row) of the cylinder displacement at different U^* values for $m^* = 5$. The relative waveforms of the displacement and the transverse fluid force coefficient x_0^* and C_y^{*}[5] are shown in the bottom row. It can be seen in Fig. 5.8a that at $U^* = 2.35$ the time corresponding to the peak values observed in x_0^* and C_y^* are very close to each other. This finding indicates that the (negative) vortex is shed from the cylinder close to the point at which the body approaches its positive extreme position. As can be seen in Fig. 5.7, the phase difference value is $\Phi_y = 40.6°$ at $U^* = 2.35$. However, increasing the reduced velocity, Φ_y shows a significant increase; at $U^* = 2.6$ the phase difference reaches $\Phi_y \cong 96°$. This remarkable increase is related to the shift in the timing of vortex shedding. It can be observed in Fig. 5.8b that the instants where the negative vortex is shed from the cylinder and that where the cylinder attains

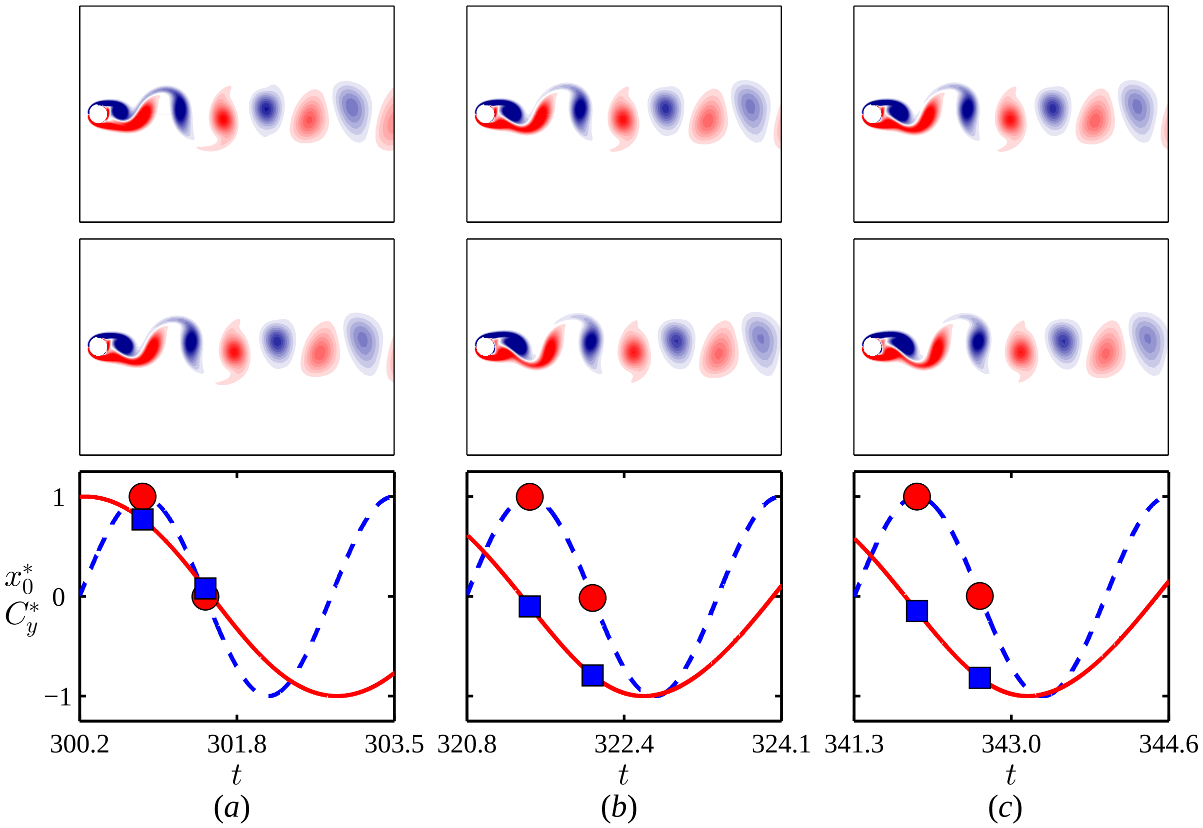

Figure 5.8: Vorticity contours at different time instants (top and middle rows), and the relative waveforms of the cylinder displacement (blue dashed line) and the transverse fluid force (red solid line) for $U^* = 2.35$ (a), 2.6 (b) and 2.7 (c) at $m^* = 5$ and Re = 180. The vortex structures in the top and middle rows are recorded at the time instant values at which the cylinder is at its positive extreme point and zero-cross over point

[5]The relative waveform of the transverse fluid force is defined as $C_y^* = [C_y - \overline{C}_y]/\hat{C}_y$, similarly to x_0^* and C_x^* [see Eqs. (4.2) and (4.3)]

its positive extreme position are far from each other: $C_y^*(t) < 0$ at the point where $x_0^*(t)$ is at its maximum. As can also be seen, beyond $U^* = 2.6$ there is no significant change in Φ_y, for example at $U^* = 2.7$ the phase difference value of $\Phi = 99.2°$ is obtained. This implies a slight shift in the timing of vortex shedding.

5.2 The effect of Reynolds number

In this section the streamwise-only VIV of a circular cylinder is investigated at different Reynolds numbers ($\mathrm{Re} = 100, 180$ and 250), and constant mass and structural damping ratio values ($m^* = 10$ and $\zeta = 0\%$, respectively). Similar to the computations carried out earlier and present in Section 5.1, the reduced velocity is varied between $U^* = 1.5$ and 3.5.

Figure 5.9a shows the non-dimensional oscillation amplitude $\hat{x}_0$ against the reduced velocity for different Re values. It can be seen the $\hat{x}_0$ curves show similar trends; increasing the reduced velocity at a certain Reynolds number, $\hat{x}_0$ increases continuously up to its peak value, and then it shows a decreasing effect. As seen, the amplitude curves shift upwards with Re. Table 5.2 shows the peak values in $\hat{x}_0, \hat{C}_x$ and $\hat{C}_y$, and the minimum values in f_x^* and $\hat{C}_y$ at the three Reynolds numbers for $m^* = 10$. It is observed that increasing the Re from 100 to 180 the peak vibration amplitude shows a fivefold increase, and the maximum $\hat{x}_0$ at $\mathrm{Re} = 250$ is more than the double of the value obtained for $\mathrm{Re} = 180$. As can also be seen, when the Reynolds number is increased, the rate of change for the amplitude of cylinder oscillation increases. Similar to high mass ratio cases for $\mathrm{Re} = 180$, $\hat{x}_0$ displays a sudden drop directly after the point corresponding to the peak cylinder response for $\mathrm{Re} = 250$.

Figure 5.9a reveals also that the U^* value where the peak vibration amplitude occurs decreases with Re. For example the maximum $\hat{x}_0$ is observed at $U^* = 2.469$ for $\mathrm{Re} = 250$, which reduced velocity value is very close to the point of $1/(2\mathrm{St}) = 2.457$. Since the Strouhal number increases in the domain of $100 \leq \mathrm{Re} \leq 250$ [see Eq. (1.8) [17]], the point corresponding to $1/(2\mathrm{St})$ decreases; hence the U^* value where the peak $\hat{x}_0$ occurs has to decrease with the Reynolds number.

Figure 5.9b shows the dimensionless vibration frequency of the cylinder as function of the reduced velocity for different Reynolds numbers. It can be seen that the f_x^* curves display similar characteristics for all Re cases. At one particular Reynolds number f_x^* decreases to its minimum point, which occurs approximately at the same reduced veloc-

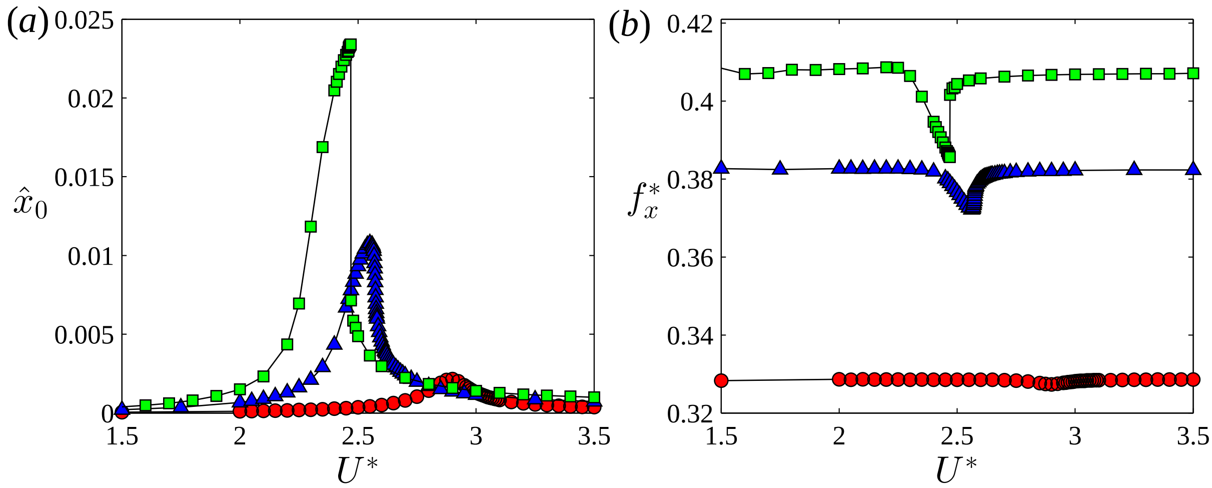

Figure 5.9: Dimensionless oscillation amplitude (a) and frequency (b) against the reduced velocity for $\mathrm{Re} = 100$ (-●-), 180 (-▲-) and 250 (-■-) at $m^* = 10$

Table 5.2: The maximum values in $\hat{x}_0, \hat{C}_x$ and $\hat{C}_y$, and the minimum values in f_x^* and $\hat{C}_y$ for different Reynolds numbers at $m^* = 10$

Re	St	$\hat{x}_0$	f_x^*	$\hat{C}_x$	$\hat{C}_y$	
		Max	Min	Max	Min	Max
100	0.1644	0.00215	0.3273	0.0109	0.3151	0.3234
180	0.1913	0.01080	0.3722	0.1057	0.5724	0.6363
250	0.2035	0.02340	0.3856	0.2279	0.7642	0.8701

ity value, where the maximum $\hat{x}_0$ is observed. Beyond the minimum point f_x^* increases asymptotically to a value corresponding to the double of the Strouhal number. Since St depends highly on Re in the low-Reynolds number domain, the asymptote shifts towards higher frequency values. It is also clearly seen in Fig. 5.9b that f_x^* shifts upwards with Re. Although this phenomenon is partially caused by the strong dependence of St on Re, the correlation is not explicit, because the difference between the minimum f_x^* and 2St is strongly influenced by the peak oscillation amplitude, which depends also on the Reynolds number. As can be seen in Fig. 5.9, the higher peak oscillation amplitude (or the Reynolds number), the higher the difference between 2St and the minimum vibration frequency value. For example the minimum f_x^* is only 0.47% lower than the double of the Strouhal number for Re = 100, while for Re = 250 f_x^* is 5.27% lower than 2St (see Table 5.2).

In Fig. 5.10a the amplitude of streamwise fluid force coefficient is shown against the reduced velocity for different Re values. Similarly to the oscillation amplitude and frequency curves (see Fig. 5.9), the $\hat{C}_x$ data sets corresponding to different Reynolds numbers show similar tendencies. It can be seen that increasing the reduced velocity at one particular Reynolds number, at the beginning, $\hat{C}_x$ increases gradually reaching a peak level, which point approximately coincides with the point of peak cylinder response. It was shown earlier that the U^* value, where the maximum in $\hat{x}_0$ and the minimum in f_x^* is identified decreases with Re. Hence, the point where the maximum $\hat{C}_x$ is found also tends to lower reduced velocity values, when the Reynolds number is increased. As seen in Table 5.2, the peak $\hat{C}_x$ value increases intensively with Re, and, as already mentioned, these values are significantly larger than those obtained for a stationary cylinder (see the relevant discus-

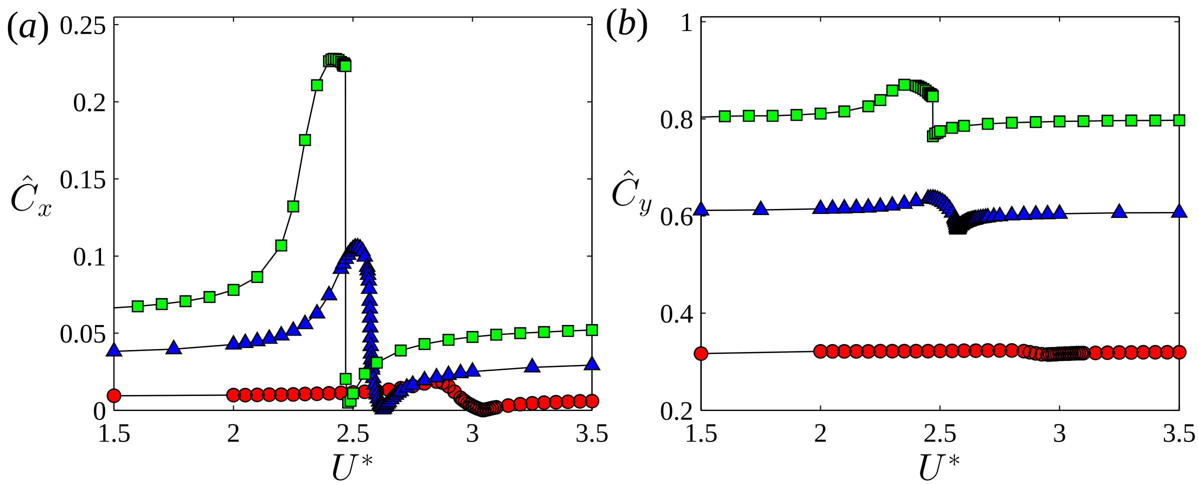

Figure 5.10: Amplitude of streamwise (a) and transverse fluid force (b) against reduced velocity for Re = 100 (-●-), 180 (-▲-) and 250 (-■-) at $m^* = 10$

sion in Section 5.1). After the maximum point $\hat{C}_x$ found to decrease to a value of zero. Similar to the different mass ratio cases presented in Section 5.1, the location of $\hat{C}_x \to 0$ coincides with the point where $f_x^* = U^{*-1}$. It can be seen that increasing the Reynolds number, the U^* value where $\hat{C}_x$ tends to zero decreases, which may also be attributable to the fact that $\mathrm{St} = \mathrm{St(Re)}$. As also seen, when Re increases, the interval within which $\hat{C}_x$ diminishes is narrowing. In addition, $\hat{C}_x$ shows a high jump between the reduced velocity values of $U^* = 2.469$ and 2.47 for Re = 250. Beyond the minimum point, $\hat{C}_x$ increases gradually for all Reynolds numbers investigated.

Figure 5.10b shows the amplitude of transverse fluid force coefficient against the reduced velocity for different Re values and constant $m^* = 10$. It can be seen that the trends in $\hat{C}_y$ is very similar to that in $\hat{C}_x$ (see Fig. 5.10a). As can be seen, when the reduced velocity is varied, at a certain Reynolds number, $\hat{C}_y$ gradually increases up to its peak point, then it decreases to its minimum value within a domain which narrows with Re. It can be observed that $\hat{C}_y$ displays a sudden drop for Re = 250 at the same point where $\hat{x}_0$, f_x^* and $\hat{C}_x$ jump (see Figs. 5.9 and 5.10a). After the minimum point $\hat{C}_y$ increases monotonically. It was mentioned earlier in Section 5.1 that the maximum and minimum values in $\hat{C}_y$ are only slightly higher and lower than the corresponding value for a stationary cylinder. This finding holds true for each Reynolds numbers considered in this analysis. The maximum values in $\hat{C}_y$ are 2.06% and 10.6% higher than the values obtained for a stationary cylinder for Re = 100 and 250, respectively, while the minimum values of $\hat{C}_y$ for the same Reynolds numbers are 0.5% and 2.8% lower than those for a non-oscillating cylinder. As mentioned earlier in Section 5.1, the slight changes in $\hat{C}_y$ is caused only by vortex dynamics. Figure 5.11 shows the vorticity contours at different Reynolds numbers corresponding to the point of peak cylinder response. As seen, despite the significant increment in the oscillation amplitude, there is no remarkable change in the vortex structure; alternating modes of vortex shedding are observed at each Re values. For this reason, the small variations in the amplitude of transverse fluid force coefficient are expected, which is consistent with the results presented in Fig. 5.10b.

Figures 5.12a and 5.12b show the variations of Φ_x and Φ_y, respectively, against the reduced velocity for different Re. As shown earlier, Φ_x is restricted to the values of 0° and 180°, and the jump between these two values occurs at the point where the amplitude of streamwise fluid force tends to zero [see Eqs. (5.6) and (5.7)]. It can be observed in Fig. 5.10a that the U^* value where $\hat{C}_x \to 0$ decreases with the Reynolds number, which explains why the point where Φ_x jumps between approximately 0° and 180° shifts to lower reduced velocities. Instead of abrupt changes, the phase difference of transverse fluid force relative to the cylinder displacement, i.e. Φ_y, increases gradually from approximately 20° to 120° (see Fig. 5.12b). Note that the data set obtained for Re = 250 is an exception,

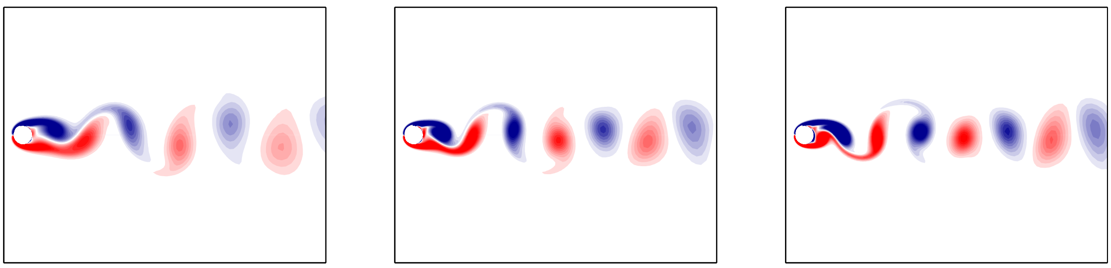

(a) (b) (c)

Figure 5.11: Vorticity contours for $(\mathrm{Re}, U^*) = (100, 2.9)$ (a), $(180, 2.55)$ (b) and $(250, 2.469)$ (c) at $m^* = 10$. Each snapshots are recorded at random phases of the cylinder oscillation

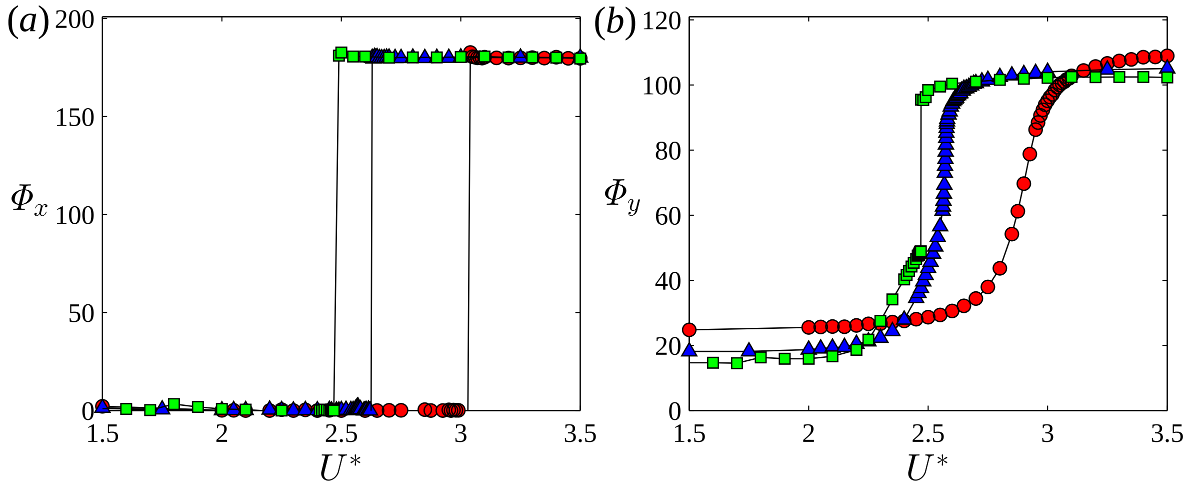

Figure 5.12: Phase differences of streamwise (a) and transverse (b) fluid force coefficients relative to the cylinder displacement against the reduced velocity for Re = 100 (-●-), 180 (-▲-) and 250 (-■-) at $m^* = 10$

Φ_y displays a sudden change at $U^* = 2.469$, similar to the quantities investigated earlier ($\hat{x}_0$, f_x^*, $\hat{C}_y$ and $\hat{C}_y$). It was shown in detail in Section 5.1 that the gradual increase in Φ_y relates to the shift in the timing of vortex shedding.

5.3 New scientific results

Contribution III

Using two-dimensional CFD computations I showed that streamwise-only vortex-induced vibrations are possible at low Reynolds numbers. A single excitation region is observed for all Reynolds number and mass ratio combinations investigated (Re $= 100, 180$ and 250, and $m^* = 2, 5, 10$ and 20). The dimensionless oscillation amplitude $\hat{x}_0$ increases up to its peak value, beyond which it gradually decreases. The nondimensional frequency of cylinder vibration f_x^* behaves oppositely: it decreases to its minimum value, then it monotonically increases. I showed that the dimensionless vibration frequency is always lower than the double of the Strouhal number for a stationary cylinder. This finding is consistent with the forced vibration results available in the literature.

The peak value in $\hat{x}_0$ and the minimum value in f_x^* are identified approximately at the same U^* value. These maximum and minimum values appear to be independent of the mass ratio. Increasing the Reynolds number, the peak $\hat{x}_0$ value increases intensively; for the Reynolds number values of Re $= 100, 180$ and 250 the peak vibration amplitudes are approximately 0.22%, 1.1% and 2.3% of the cylinder diameter, respectively. I showed also that the single excitation region identified in this study corresponds to the second response branch found at moderately high-Re experiments, because alternating modes of vortex shedding are observed in each cases.

Related publications: Konstantinidis et al. [J5], Dorogi et al. [C12] and Dorogi et al. [C11]

Contribution IV

Assuming that the cylinder displacement x_0 and the streamwise fluid force coefficient C_x are sinusoidal functions of time I derived the following formula for the amplitude of C_x:

$$\hat{C}_x = \frac{2\pi^3 m^* \hat{x}_0}{U^{*2}} \sqrt{(1 - f_x^{*2} U^{*2})^2 + 4\zeta^2 f_x^{*2} U^{*2}}, \tag{5.8}$$

where m^* and ζ are the mass ratio and damping ratio values, respectively, $\hat{x}_0$ and f_x^* are the dimensionless oscillation amplitude and frequency values, and U^* is the reduced velocity. Substituting $\zeta = 0\%$, it can be seen that $\hat{C}_x = 0$ at the point, where the vibration frequency coincides with the cylinder's natural frequency, i.e. at $f_x^* U^* = 1$. I confirmed this finding using CFD simulations for $m^* = 2, 5, 10$ and 20 at Re $= 180$. The computations revealed that $\hat{C}_x \to 0$ at $U^* \cong 2.625$. Since $\hat{x}_0$ is non-zero, the streamwise fluid force coefficient has strongly non-harmonic nature in the vicinity of $U^* = 2.625$. I showed the occurrence of a frequency component double the frequency of cylinder vibration (i.e. the second harmonic component) just before the point of $\hat{C}_x \to 0$. At the reduced velocity value, where the vibration frequency is the closest to the natural frequency of the cylinder, the intensity of the second harmonic component is the highest.

The harmonic oscillator model show that the phase difference of C_x relative to x_0 has to switch suddenly between $0°$ and $180°$, which I confirmed using the CFD data. Besides, I calculated the phase lag of the transverse fluid force with respect to the cylinder displacement Φ_y. Instead of abrupt jumps, I showed that Φ_y displays gradual increase from approximately $20°$ to $110°$. This gradual increase can be attributed to shift in the timing of vortex shedding, which was confirmed using the instantaneous vorticity contours.

Related publications: Konstantinidis et al. [J5], Dorogi et al. [C12] and Dorogi et al. [C11]

Chapter 6

Transverse vortex-induced vibrations: identification of the upper branch for Re = 300

In this chapter, similar to the computations carried out in Chapter 5, single-degree-of-freedom vortex-induced vibrations are investigated, but here the cylinder is restricted to oscillate only transverse to the main stream. Although there are several studies in the literature dealing with transverse-only vortex-induced vibrations, there are still some open questions which are worth to deal with.

As was pointed out in Chapter 1, vortex-induced vibrations show very different trends at high and low Reynolds numbers. For high-Re cases, and very low mass and damping values, three-branch cylinder response occurs; initial, upper and lower branches are found [59, 60, 62, 63, 102]. Feng [57] and Khalak and Williamson [59] showed that the mass-damping parameter affects the cylinder response significantly; at high $m^*\zeta$ values the upper branch does not appear, a two-branch response is identified. In contrast, in the low-Reynolds number domain, independently of the $m^*\zeta$ only two-branch cylinder response is identified; an upper branch has not yet been observed [38, 66, 70, 72, 89].

However, there are some relevant findings available in the literature, which may refer to the possible existence of the upper branch in the low-Reynolds number domain. These findings are listed as follows:

(a) Khalak and Williamson [59] found 2P wake mode in the upper branch. However, Evangelinos and Karniadakis [71] reported using two and three-dimensional computations that the P+S vortex pattern may also be associated with the upper branch;

(b) Leontini et al. [31] carried out transverse-only forced vibration computations at several Reynolds numbers. At Re = 300, close to the fundamental lock-in domain they identified the P+S vortex structure with positive mechanical energy transfer, meaning that the energy is transferred from the fluid to the cylinder.

(c) Singh and Mittal [72] investigated two degrees of freedom vortex-induced vibrations at constant $U^* = 4.92$. They showed the occurrence of the P+S wake mode above Re = 300;

(d) The results from the 2DoF VIV computations presented in Chapter 4, and published in [J3], show that the P+S vortex shedding mode develops at high dimensionless natural frequency values, near the Reynolds number of 300.

These findings motivated us to address the following research questions (see also Section 1.2):

Does the upper branch (i.e. the three-branch cylinder response) occur at the Reynolds number of 300? What is the effect of structural damping on the cylinder response?

In order to answer these questions, computations are carried out at the Reynolds number and mass ratio values of Re $= 300$ and $m^* = 10$, respectively. The structural damping ratio is considered between $\zeta = 0\%$ and 5%, hence the combined mass-damping parameter is chosen to be in the range of $m^*\zeta = 0$ and 0.5. The reduced velocity based on the cylinder's natural frequency in vacuum is varied from $U^* = 2.5$ to 7.5.

6.1 The three-branch response

Figure 6.1a shows the rms values of the non-dimensional cylinder displacement $y_{0'}$, and in Fig. 6.1b the vibration frequency normalized by the cylinder's natural frequency in vacuum f_y/f_N is plotted against U^* for $\zeta = 0\%$. The dashed line in Fig. 6.1b represents f_v/f_N, where f_v is the vortex shedding frequency for a stationary cylinder. It can be seen that the cylinder response obtained is very similar to the three-branch response presented in many studies but only for high Reynolds numbers. In the following, the individual branches will be described in detail.

As can be seen, in the range of $2.5 \leq U^* \leq 3.5$ the oscillation amplitude is very low and the vibration frequency is close to the vortex shedding frequency for a stationary cylinder ($f_y \cong f_v$). From $U^* = 3.5$ to 4 an initial branch is identified, where f_y/f_N represents an approximately constant value of $f_y/f_N \cong 0.95$, and $y_{0'}$ increases intensively. Between $U^* = 4$ and 5.9 lock-in or synchronization is observed, where the vibration frequency locks approximately to the natural frequency of the system (see Fig. 6.1b). The entire lock-in domain can be divided into two subdomains. Relatively high oscillation amplitudes are observed in the range of $4 < U^* \leq 4.89$ (see Fig. 6.1a), where the vibration frequency is slightly lower than the cylinder's natural frequency ($f_y/f_N < 1$, Fig. 6.1b). This reduced velocity domain appears to correspond to the upper branch. In order to confirm this suggestion, careful analysis is needed, which is presented in Section 6.2. At the higher boundary of the suggested upper branch $y_{0'}$ drops abruptly by 7%, and f_y passes through f_N. Govardhan and Williamson [60] identified a similar phenomenon at the boundary separating the upper and the lower branches for Re $\cong 10^3$–10^4. Between $U^* = 4.89$ and 5.9 the lower branch is observed, where f_y is slightly higher than f_N (see Fig. 6.1b), and $y_{0'}$

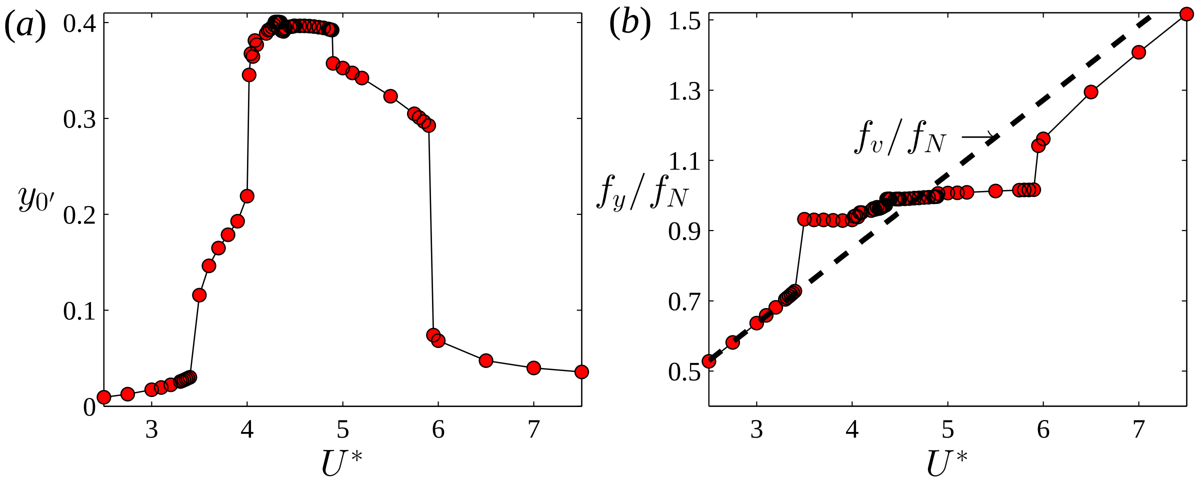

Figure 6.1: Root-mean square values of transverse cylinder displacement (a) and the vibration frequency normalized by the natural frequency of the system in vacuum (b) against the reduced velocity for $\zeta = 0\%$

reaches intermediate values (Fig. 6.1a). The reduced velocity range above $U^* = 5.9$ is out of the lock-in domain: the oscillation amplitude is very low ($y_{0'} \cong 0.1$), and the vibration frequency is close again to the vortex shedding frequency for a stationary cylinder.

Govardhan and Williamson [60], based on the methodology introduced by Lighthill [61] applied the following decomposition on the time-dependent transverse fluid force $\widetilde{F}_y(t)$:

$$\widetilde{F}_y(\widetilde{t}) = \widetilde{F}_V(\widetilde{t}) + \widetilde{F}_p(\widetilde{t}). \tag{6.1}$$

In this formula $\widetilde{F}_V$ and $\widetilde{F}_p$ are the instantaneous vortex and potential added mass forces, respectively, per unit length of the cylinder. The potential added mass force is defined as follows [60]:

$$\widetilde{F}_p(\widetilde{t}) = -C_A m_d \ddot{\widetilde{y}}_0(\widetilde{t}), \tag{6.2}$$

where C_A is the potential added mass coefficient, which equals to unity for a circular cylinder [56], $m_d = \rho\frac{d^2\pi}{4}$ is the displaced fluid mass per unit length of the cylinder, and $\ddot{\widetilde{y}}_0$ is the dimensional cylinder acceleration. Rearranging and normalizing Eq. (6.1) by $\frac{1}{2}\rho U_\infty^2 d$ the following expression can be obtained for the instantaneous vortex force coefficient:

$$C_V(t) = C_y(t) + \frac{\pi}{2}\ddot{y}_0(t), \tag{6.3}$$

where $\ddot{y}_0 = \frac{d}{U_\infty^2}\ddot{\widetilde{y}}_0$ is the non-dimensional cylinder acceleration.

Figures 6.2a and 6.2b show the rms values of transverse fluid force and vortex force coefficients $C_{y'}$ and $C_{V'}$, respectively, against U^* for $\zeta = 0\%$. It can be seen that for very low cylinder displacements, i.e. in the domains of $2.5 \leq U^* \leq 3.45$ and $5.9 < U^* \leq 7.5$, $C_{y'}$ and $C_{V'}$ are approximately identical and near the value obtained for a stationary cylinder ($C_{y'} \cong C_{V'} \sim 0.5$, see Norberg [23]). Govardhan and Williamson [60] found $C_{y'} \cong C_{V'} \cong 0.1$ in the very low oscillation amplitude range (in $U^* < 4$ and $U^* > 10.5$ in their study), which is close to $C_{V'} \cong 0.05$, the value identified for a non-oscillating cylinder at Re $\sim 10^3$ [23]. In this sense, the currently obtained CFD results for Re $= 300$ and the experimental findings of [60] for high Reynolds numbers show good *qualitative* agreement.

Increasing the reduced velocity in the initial branch, $C_{y'}$ increases gradually, and reaches its peak value at the beginning of the suggested upper branch (at $U^* = 4$, see Fig. 6.2a). Between $U^* = 4$ and 4.89 $C_{y'}$ drops dramatically, moreover at $U^* = 4.36$ (in

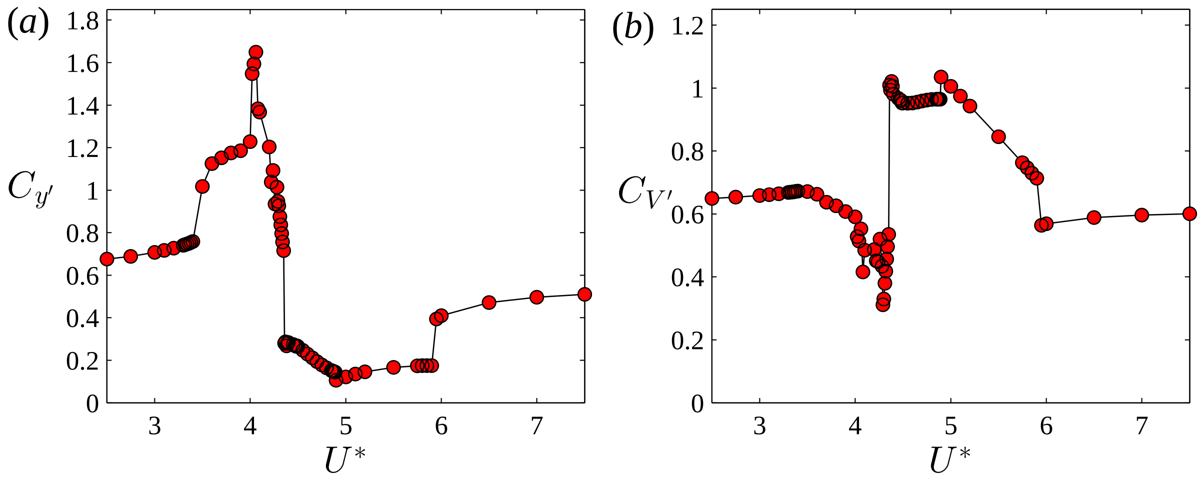

Figure 6.2: Root-mean square values of transverse fluid force (a) and vortex force (b) against the reduced velocity for $\zeta = 0\%$

the middle of the proposed upper branch) it suffers a sudden change from $C_{y'} \cong 0.71$ to approximately 0.25. It is also seen in Fig. 6.2a that at $U^* = 4.89$ $C_{y'}$ shows another but much smaller jump, above which it increases. The experimental results of Govardhan and Williamson [60] and the trends in the current computational results are very similar. However, abrupt change in $C_{y'}$ in the middle of the upper branch has not been identified in the high-Reynolds number domain; this jump may correspond to other important flow phenomena.

The rms values of vortex force coefficient (see Fig. 6.2b) found to decrease in the initial branch until it reaches its minimum value. The locations of the extreme values in $C_{y'}$ and $C_{V'}$ are near to each other. In the proposed upper branch $C_{V'}$ increases strongly, and at $U^* = 4.36$ it changes suddenly between $C_{V'} \cong 0.53$ and 1.02. Similarly again to the tendencies observed in $C_{y'}$, at $U^* = 4.89$ the rms of vortex force coefficient shows another but much smaller jump. The peak value in $C_{V'}$ is observed at the beginning of the lower branch, which finding qualitatively agrees well with that of [60].

6.2 Phase dynamics for undamped vibrations

The results presented earlier suggest that the upper branch exists at the Reynolds number of 300. In order to confirm this suggestion, careful analyses are required. Let us assume again that the motion of the cylinder and the aerodynamic force coefficients acting on the body are sinusoidal functions of time:

$$y_0(t) = \hat{y}_0 \sin 2\pi f_y^* t, \tag{6.4}$$

$$C_y(t) = \hat{C}_y \sin(2\pi f_y^* t + \Phi_y), \tag{6.5}$$

$$C_V(t) = \hat{C}_V \sin(2\pi f_y^* t + \Phi_V), \tag{6.6}$$

where $\hat{C}_y$ and $\hat{C}_V$ are the amplitude of the transverse fluid force and vortex force coefficients, and $\hat{y}_0$ and f_y^* are the non-dimensional oscillation amplitude and frequency values. In these expressions Φ_y and Φ_V are the phase differences for transverse fluid force and vortex force, respectively, relative to the cylinder displacement. For the sake of simplicity, Φ_y and Φ_V will be referred to as *transverse* and *vortex phases*, respectively.

In Chapter 5 the harmonic oscillator model is given in detail for a circular cylinder free to vibrate only in streamwise direction. Since the approaches used for transverse-only and streamwise-only vortex-induced vibrations are very similar to each other, only little detail is provided in this chapter. For further details the reader is referred to Chapter 5, Section 5.1.

Substituting Eqs. (6.4) and (6.5) into the cylinder equation of motion [Eq. (2.13)], and equating the coefficients of sine and cosine terms, the following expressions can be obtained:

$$\cos \Phi_y = 2\pi^3 \frac{m^* \hat{y}_0}{\hat{C}_y U^{*2}} (1 - f_y^{*2} U^{*2}), \tag{6.7}$$

$$\sin \Phi_y = 4\pi^3 \frac{m^* \zeta \hat{y}_0}{\hat{C}_y U^*} f_y^*. \tag{6.8}$$

It can be seen in Eq. (6.7) that $\cos \Phi_y$ changes from positive to negative at the point where the vibration frequency passes through the natural frequency of the system in vacuum, i.e. at $f_y^* U^* = 1$. In addition, Eq. (6.8) shows that for zero structural damping, $\sin \Phi_y = 0$, therefore, the cylinder motion can only be in-phase ($\Phi_y = 0°$) or out-of-phase

($\Phi_y = 180°$) with the transverse fluid force. Hence, as the system goes through $f_y^* U^* = 1$ for $\zeta = 0°$, the transverse phase has to jump from 0° to 180°.

Introducing $C_y(t) = C_V(t) - \frac{\pi}{2}\ddot{y}_0(t)$ [based on Eq. 6.3] and the harmonic approximations [Eqs. (6.4) and (6.6)] into Eq. (2.13), and equating the coefficients of the sine and cosine functions, the following formulæ are obtained:

$$\cos \Phi_V = 2\pi^3 \frac{(m^* + C_A)\hat{y}_0}{\hat{C}_V U_A^{*2}} (1 - f_y^{*2} U_A^{*2}), \tag{6.9}$$

$$\sin \Phi_V = 4\pi^3 \frac{\sqrt{m^*(m^* + C_A)}\zeta \hat{y}_0}{\hat{C}_V U_A^*} f_y^*, \tag{6.10}$$

where U_A^* is the reduced velocity based on the cylinder's natural frequency in still fluid $f_{N,a}$. Similarly to Eq. (6.7), Eq. (6.9) shows that $\cos \Phi_V$ changes from positive to negative as the system passes through $f_y^* U_A^* = 1$. Since for undamped vibrations the vortex phase is restricted to the values of $\Phi_V = 0°$ and 180°, the vortex phase has to jump between these two values (0° and 180°) at the point corresponding to $f_y^* U_A^* = 1$.

Govardhan and Williamson [60] at high Reynolds numbers and low mass and damping values found that Φ_V and Φ_y jump at different reduced velocity values. The U^* domain which is enclosed between the two phase jumps (in Φ_V at its beginning and in Φ_y at its upper boundary) corresponds to upper branch. In other words, to confirm that the range of $4 < U^* \leq 4.89$, where relatively high oscillation amplitudes are found (see Fig. 6.1), represents the upper branch, Φ_y and Φ_V should be investigated.

The time-dependent transverse and vortex phases (Φ_y and Φ_V) are calculated using the analytical signal approach based on Hilbert transform, which is shown in detail in Appendix A.2.2. In the figures the time-dependent phase differences are mostly plotted in radian as unwrapped signals. However, their time-average values ($\overline{\Phi}_y$ and $\overline{\Phi}_V$) are shown in degrees, and are calculated via time-averaging Φ_y and Φ_V wrapped in the interval of $[-\pi/2, 3\pi/2]$ (see also Appendix A.2.2).

Figure 6.3 shows Φ_y (on the left-hand side) and Φ_V (right) for different reduced velocity values in the very low amplitude range (see Figs. 6.3a and 6.3b), and in the initial branch (Fig. 6.3c). It can be seen that in the domain of $2.5 \leq U^* \leq 3.45$ the transverse and vortex phases are approximately constant, only small oscillations are observed near $U^* = 3.45$ (Fig. 6.3b). In the initial branch ($3.45 < U^* \leq 4$) Φ_y shows intermediate oscillations, but its time-mean value is roughly zero (Fig. 6.3c). However, in the same range Φ_V shows unbounded decrease, which corresponds to the loss of synchronization between the cylinder motion and the vortex force coefficient [103, 104]. In Pikovsky et al. [103] this phenomenon is interpreted by analyzing the relationship between motion and forcing frequencies.

In Fig. 6.4 differences of vibration frequency relative to the frequency of transverse fluid force and vortex force coefficients, i.e. $f_y^* - f_{C_y}^*$ and $f_y^* - f_{C_V}^*$, respectively, are shown against U^* in the initial, proposed upper and lower branches. These quantities are called detuning. It can be seen that in the initial branch $f_y^* > f_{C_V}^*$, which explains why the time-dependent vortex phase decreases in this domain [103]. In addition, the difference between the two frequency values is relatively large in the range of $3.45 < U^* \leq 4$, which causes the roughly uniform drop in the vortex phase (see Fig. 6.3c). It is also shown in Fig. 6.4 that $f_y^* - f_{C_y}^* \cong 0$ in the initial branch, which implies the roughly constant value of transverse phase.

Based on Fig. 6.1, the upper branch is expected to appear in the domain of $4 < U^* \leq 4.89$. Figures 6.5a and 6.5b show the times histories of transverse and vortex phases at $U^* = 4.2$ and 4.28, respectively. In contrast to the trends observed in the initial branch, in the range of $4 < U^* \leq 4.28$ f_y^* is lower than $f_{C_V}^*$ (see Fig. 6.4), which leads to increasing Φ_V (Fig. 6.5). Besides, $|f_y^* - f_{C_V}^*|$ is significantly lower in this domain compared to that

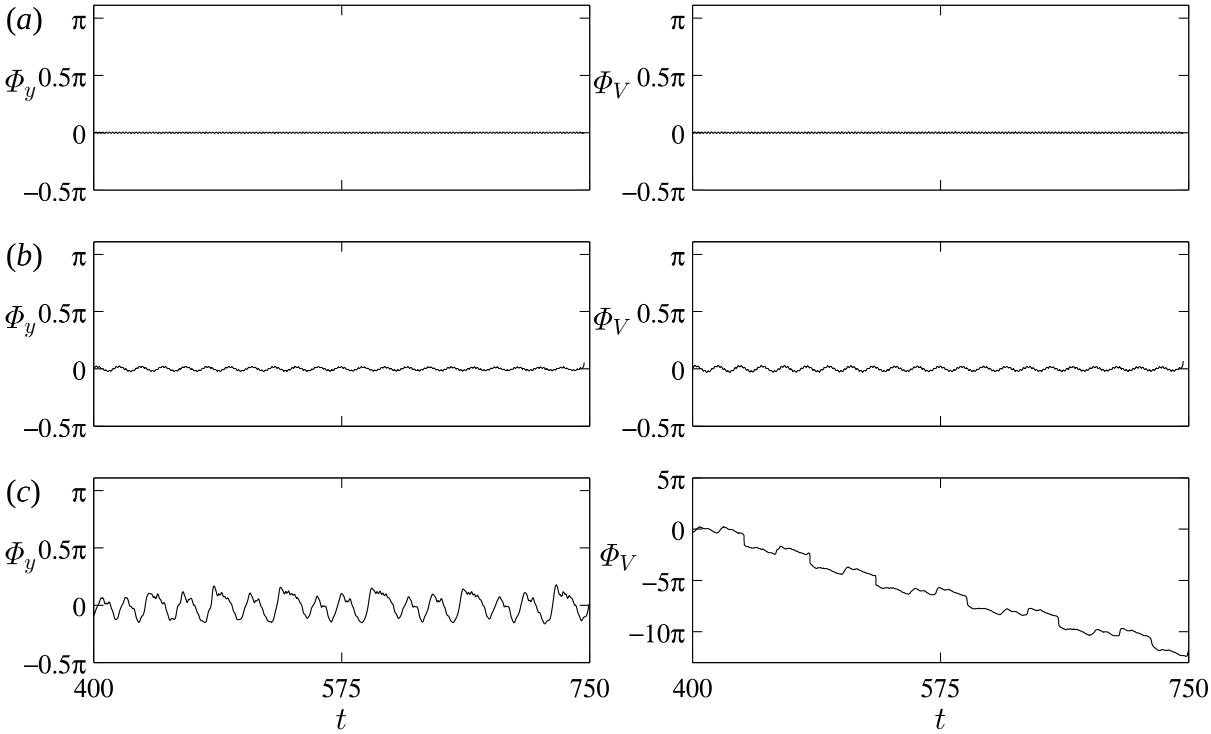

Figure 6.3: Time-dependent phase differences of transverse fluid force (left) and vortex force (right) relative to cylinder displacement at the reduced velocity values of $U^* = 3$ (a), 3.36 (b) and 4 (c) for $\zeta = 0\%$

in the initial branch; thus, one can expect remarkable changes in the dynamics of vortex phase. As shown in Fig. 6.5, instead of unbounded changes, Φ_V consists of time intervals, so called *epochs* [103], where the vortex phase is approximately constant. It can be seen that the time interval of an epoch extends with the reduced velocity. Two neighboring epochs are separated by so-called *phase slips*, where the vortex phase shows rapid change [103]. In addition, Figs. 6.5a and 6.5b show approximately constant Φ_y values, which is expected because $|f_y^* - f_{C_y}^*| \cong 0$ between $U^* = 4$ and 4.28 (Fig. 6.4). Note that in this context, the phrase *approximately constant* refers to that the phase difference varies around a constant value (in this case, around zero).

Figure 6.6 shows the time histories of vortex phase wrapped between $-\pi/2$ and $3\pi/2$ at the same reduced velocity values where the time-dependent phase differences were investigated in Figs. 6.3c and 6.5. Pikovsky et al. [103] showed that the change of phase difference via a phase slip (see Fig. 6.5) cannot be arbitrary, it is always the whole number multiples of π. This finding is explicitly shown in Figs. 6.6b and 6.6c.

It is also very important to see that at an epoch, the wrapped vortex phase varies periodically around π (see Figs. 6.6a and 6.6b), and Φ_y represents an almost constant zero value (Fig. 6.5). For this reason, the conditions of the existence of the upper branch ($\Phi_V = \pi$ and $\Phi_y = 0$) in $4 < U^* \leq 4.28$ seem to be satisfied. However, in-between two epochs (i.e. in phase slips) the vortex phase deviates marginally from π, which causes discrepancies in its time-mean value. As shown earlier, time lengths of the epochs increase with U^*, that is, the deviation in $\overline{\Phi}_V$ from its theoretically expected value ($\overline{\Phi}_V = 180°$) decreases with the reduced velocity. Similar issues appear in the initial branch (see Fig. 6.6a), where the high spikes occurring in the wrapped phase angle influence $\overline{\Phi}_V$ significantly. In further time-averaged phase difference plots it is necessary to distinguish between synchronous and non-synchronous cases. By *non-synchronous cases* I mean that at the corresponding U^* values unbounded changes or phase slips are identified. These points will be indicated by empty symbols.

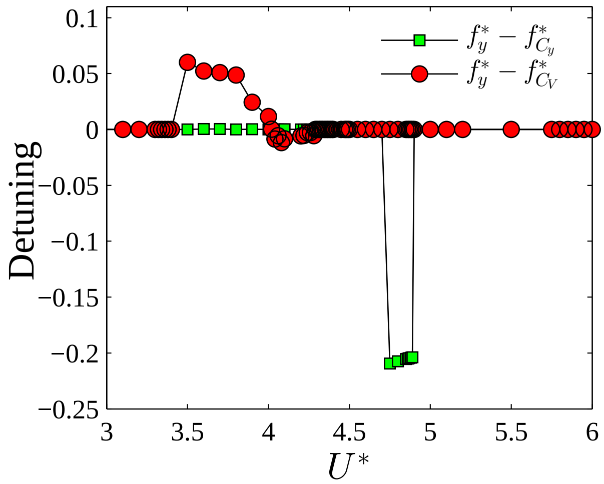

Figure 6.4: Detuning values $f_y^* - f_{C_y}^*$ and $f_y^* - f_{C_V}^*$ against the reduced velocity in the initial and upper branches for $\zeta = 0\%$. Here f_y^*, $f_{C_y}^*$ and $f_{C_V}^*$ are the frequencies of cylinder oscillation, transverse fluid force and vortex force, respectively

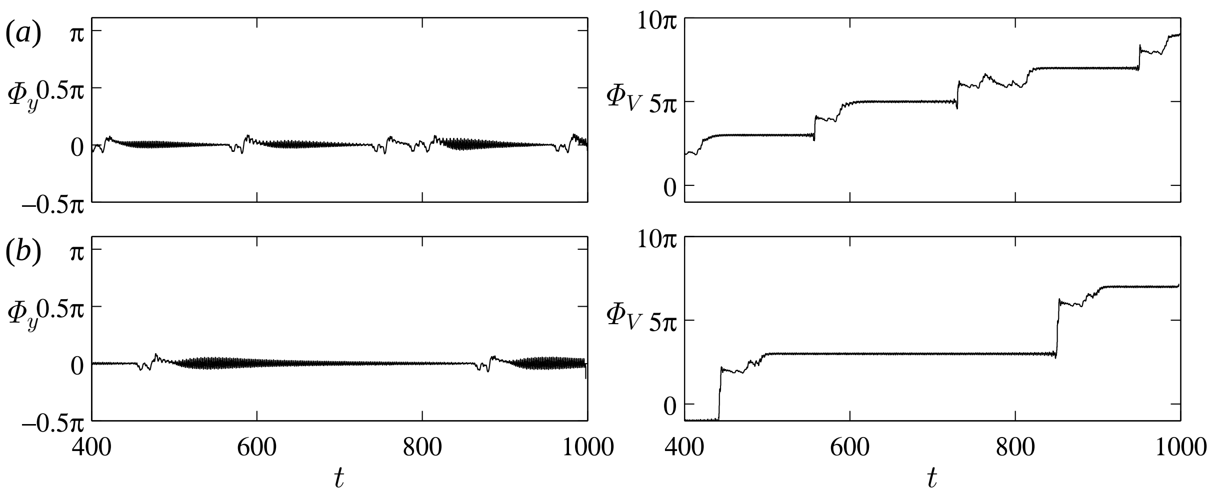

Figure 6.5: Time-dependent phase differences Φ_y (left) Φ_V (right) at $U^* = 4.2$ (a) and 4.28 (b) in the upper branch for $\zeta = 0\%$

Figure 6.7 shows the time histories of transverse and vortex phases in the range of $4.28 < U^* \leq 4.89$. As can be seen in Fig. 6.4, the frequencies of vortex force and transverse fluid force are equal to the vibration frequency of the cylinder between $U^* = 4.28$ and 4.7. Consequently, *approximately constant* Φ_y and Φ_V values are expected in this domain. Figures 6.7a-6.7c corroborate these expectations: neither unbounded change nor phase slips are identified in Φ_y and Φ_V. It is also seen in these figures that the time-mean values of Φ_V and Φ_y approximately equal to π and 0, respectively, which are consistent with the experimental results for the upper branch. This finding further strengthens my previous evidence concerning the existence of the upper branch at Re = 300.

It can also be seen in Figs. 6.7a-6.7c that the fluctuations in transverse and vortex phases are amplified when U^* is increased. As seen, in the range of $4.28 < U^* \leq 4.35$, both Φ_y and Φ_V show small periodic oscillations (Fig. 6.7a). Varying the reduced velocity from $U^* = 4.35$ to 4.48, Φ_y oscillates randomly with very high rms values. The random oscillations are also observed in the time history of Φ_V, but its fluctuation is significantly lower. In the domain of $4.48 < U^* \leq 4.7$ the transverse and the vortex phases return back to periodic, but the very high fluctuations in Φ_y are still observed (see Fig. 6.7c).

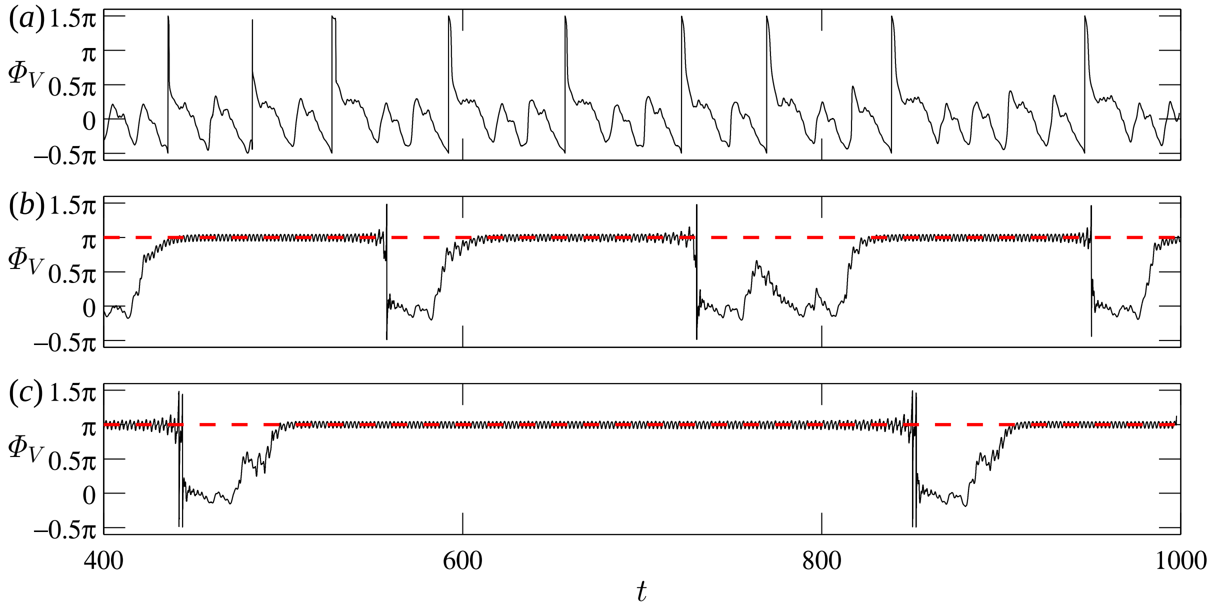

Figure 6.6: Time-dependent vortex phase at $U^* = 4$ (a), 4.2 (b) and 4.28 (c) for $\zeta = 0\%$. Here, phase difference is wrapped in $[-\pi/2; 3\pi/2]$

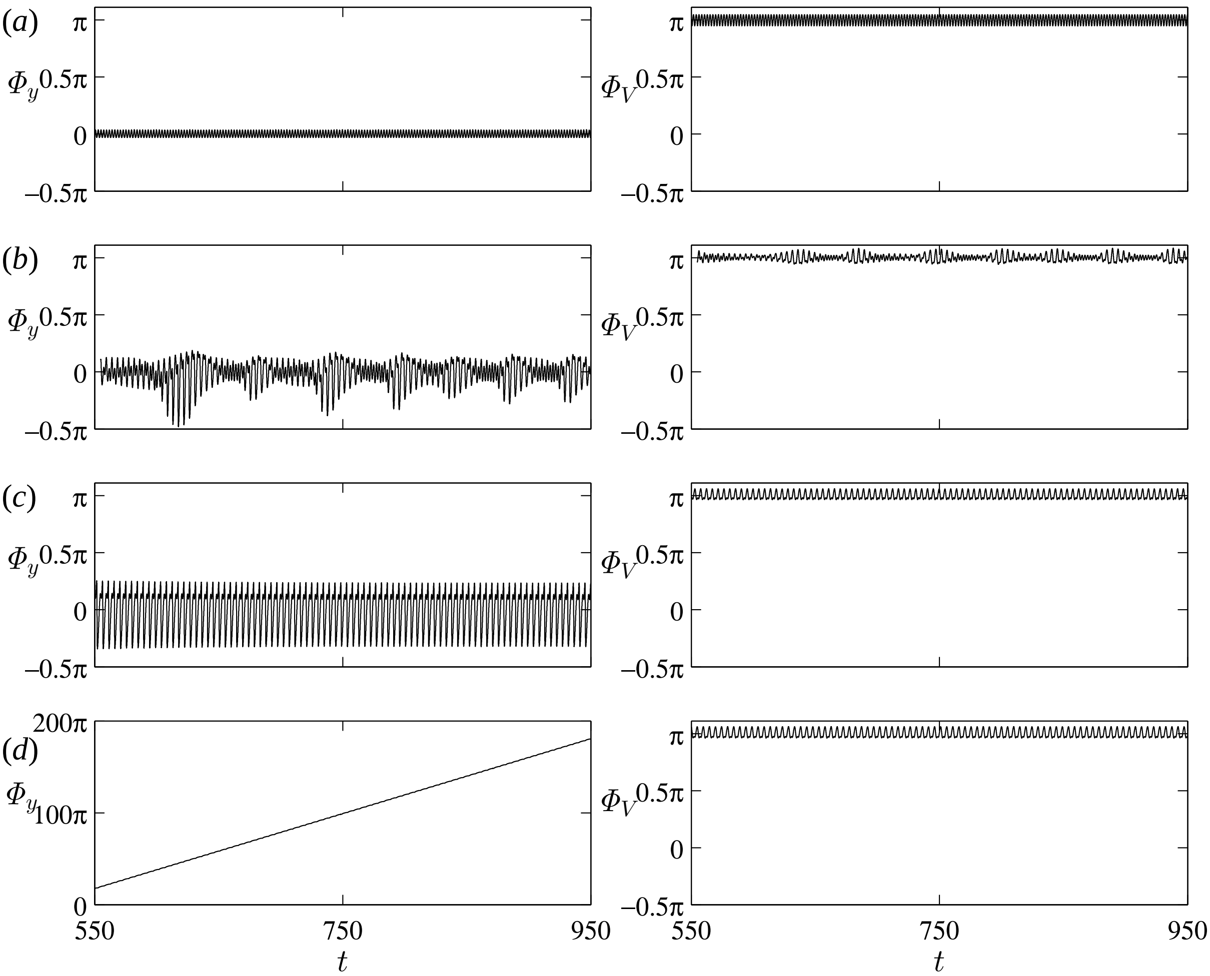

Figure 6.7: Time-dependent phase differences Φ_y (left) Φ_V (right) at $U^* = 4.35$ (a), 4.4 (b), 4.65 (c) and 4.89 (d) in the upper branch for $\zeta = 0\%$

Increasing the reduced velocity in the range of $4.7 < U^* \leq 4.89$, I found that the detuning $f_y^* - f_{C_y}^*$ drops to approximately -0.2 (Fig. 6.4), which causes an unbounded increase in the transverse phase (Fig. 6.7d). It is very interesting to note that the absolute value of this detuning is very close to the Strouhal number at $\mathrm{Re} = 300$, i.e. $f_y^* - f_{C_y}^* \cong -\mathrm{St}$. Besides, the vibration frequency is also near St in the aforementioned U^* range ($f_y^* \cong \mathrm{St}$, see Fig. 6.1b). Combining these two findings the detuning value of -0.2 can only be achieved when the frequency of the transverse fluid force, more precisely, the most dominant frequency component in the spectra of C_y, is double the Strouhal number, $f_{C_y}^* \cong 2\mathrm{St} \cong 2f_y^*$. Moreover, the unreasonably high fluctuations in Φ_y appear to be caused by the occurrence of higher order harmonics for C_y. These effects are further investigated in Section 6.4.

Figure 6.8 shows Φ_y and Φ_V in the range of $4.89 < U^* \leq 5.9$, which domain corresponds to the lower branch, because $\overline{\Phi}_y \cong \overline{\Phi}_V \cong 180°$ [60, 63]. It can be seen that the rms values of transverse and vortex phases decrease with the reduced velocity.

Figure 6.9 shows the time-mean values of transverse and vortex phases $\overline{\Phi}_y$ and $\overline{\Phi}_V$, respectively, in degrees where filled and empty symbols indicate synchronous and non-

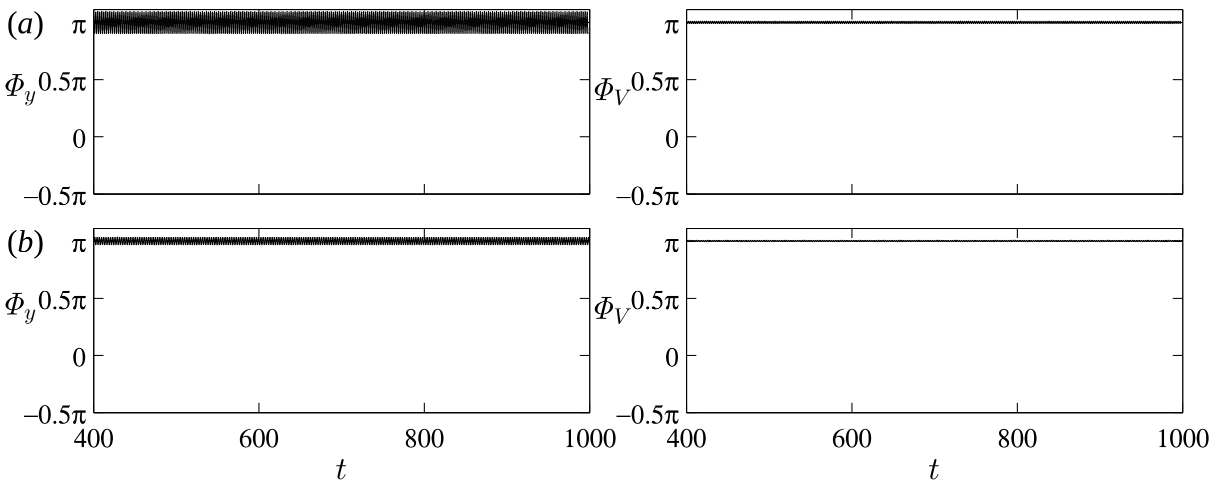

Figure 6.8: Time-dependent phase differences Φ_y (left) Φ_V (right) at $U^* = 4.9$ (a) and 5.5 (b) in the lower branch for $\zeta = 0\%$

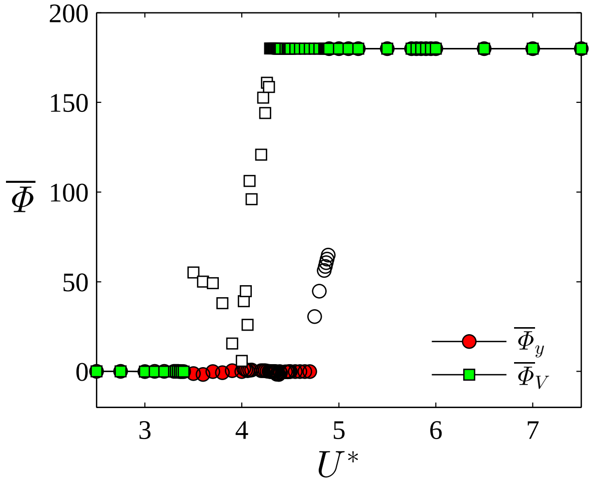

Figure 6.9: Time-mean transverse and vortex phase values against U^* for $\zeta = 0\%$. Here synchronous and non-synchronous cases are denoted by filled and empty symbols, respectively

synchronous cases. Although the phase differences show gradual variations between 0° and 180°, the transitions in $\overline{\Phi}_V$ and $\overline{\Phi}_y$ are observed in different U^* ranges, which is the distinctive feature of three-branch response. However, experimental studies at high Reynolds numbers and low mass and damping values reported abrupt phase changes in the initial↔upper and upper↔lower branch transition domains. As discussed earlier, the reason behind the gradual and not abrupt variations in $\overline{\Phi}_V$ and $\overline{\Phi}_y$ is the unbounded changes and phase slips found in the time-dependent transverse and vortex phases.

To conclude, the initial branch is observed in the range of $3.45 < U^* \leq 4$, the upper branch between $U^* = 4$ and 4.89, and the lower branch in the domain of $4.89 < U^* \leq 5.9$. The most important observations related to the dynamics of Φ_y and Φ_V at the different response branches are summarized in Table 6.1.

Table 6.1: Summary of phase dynamics in the three response branches

Branch	U^* domain	Φ	Φ_v
–	$[2.5, 3.45]$	low periodic osc.	low periodic osc.
Initial	$]3.45, 4.0]$	intermediate osc.	unbounded decrease
Upper	$]4.0, 4.28]$	low random osc.	phase slips
	$]4.28, 4.35]$	low periodic osc.	low periodic osc.
	$]4.35, 4.48]$	high random osc.	low random osc.
	$]4.48, 4.7]$	high periodic osc.	low periodic osc.
	$]4.7, 4.89]$	unbounded increase	low periodic osc.
Lower	$]4.89, 5.9]$	low periodic osc.	low periodic osc.

6.3 Analyses for non-zero structural damping

As mentioned at the beginning of Chapter 6, the second important aim of this chapter is to investigate the effect of structural damping ratio on the cylinder response. Figure 6.10 shows $y_{0'}$ and f_y/f_N as functions of the reduced velocity for different structural damping ratio values between $\zeta = 0\%$ and 5%. It can be seen that the results obtained harmonize

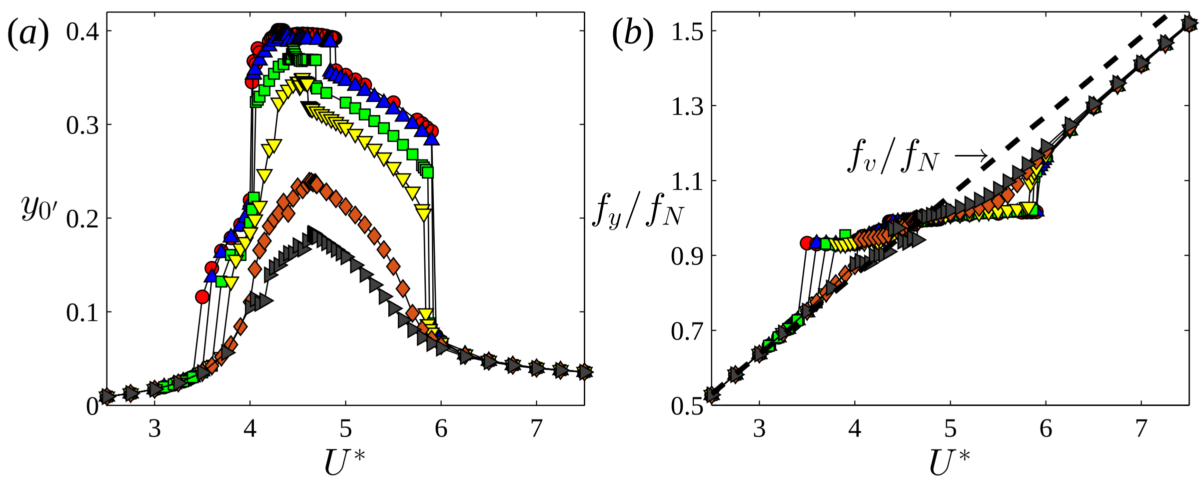

Figure 6.10: Root-mean square values of transverse cylinder displacement (a) and vibration frequency normalized by the natural frequency in vacuum (b) against the reduced velocity for $\zeta = 0\%$ (-●-), 0.1% (-▲-), 0.5% (-■-), 1% (-▽-), 3% (-◆-) and 5% (-◀-)

with the expectations: the oscillation amplitude decreases with the damping ratio. As can be observed in Fig. 6.10a, the structural damping causes significant changes in the cylinder response. The obtained $y_{0'}$ and f_y/f_N curves for $\zeta \leq 1\%$ are very similar to each other, they seem to form three-branch response. For these ζ values and low reduced velocities (below approximately $U^* = 3.5$), the oscillation amplitude is very low. Between $U^* \cong 3.5$ and 4 the initial branch is identified, where $y_{0'}$ increases intensively. At $U^* \cong 4$, regardless of ζ, the oscillation amplitude shows a sudden upward jump, which corresponds to the boundary separating the initial and upper branches. However, the U^* value where the cylinder response switches between the upper and lower branches shows to decrease with the structural damping ratio. Klamo et al. [62] found a somewhat different feature, in their study the upper↔lower branch transition range remained independent of the structural damping. Soti et al. [63] investigated a wider ζ range. They showed that when damping was increased the boundary between the upper and lower branches shifted to lower U^* values. This finding is very similar to my results at Re = 300 (see Fig. 6.10).

Figure 6.11 shows the time-dependent transverse and vortex phases in the initial branch (Fig. 6.11a), upper branch (Fig. 6.11b and Fig. 6.11c) and lower branch (Fig. 6.11d) for $\zeta = 0.5\%$. It can be seen in Fig. 6.11a that Φ_V shows an unbounded decrease in the initial branch, similar to that observed for undamped vibrations. At the beginning of the upper branch phase slips are found in the vortex phase (Fig. 6.11b), but interestingly, Φ_V remains *approximately constant*, because the detuning $f_y^* - f_{C_V}^*$ is zero in this range. Increasing the reduced velocity in the further part of the upper branch, the results show similar features to those reported for $\zeta = 0\%$. However, at the end of the upper branch no unbounded increase was identified in the transverse phase, which is in contrast to the results presented for undamped vibrations (see Fig. 6.7d). Figure 6.11c shows Φ_y and Φ_V just before the jump to the lower branch, and here *approximately constant* transverse

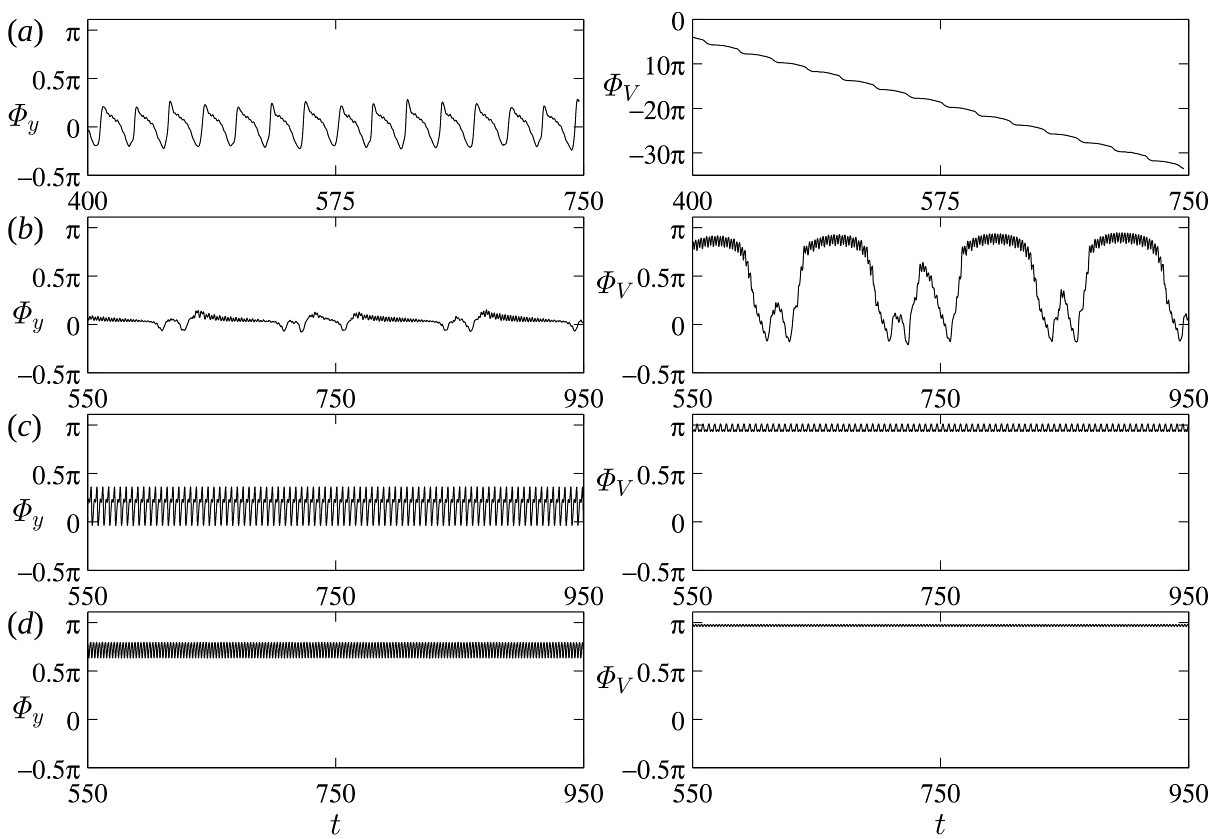

Figure 6.11: Time histories of phase differences Φ_y (left) Φ_V (right) at reduced velocity values of $U^* = 3.8$ (a), 4.25 (b), 4.68 (c) and 4.8 (d) for $\zeta = 0.5\%$

phase is shown. The possible reason behind this phenomenon is that the role of the second harmonic frequency component changes with the structural damping ratio. This effect will be further investigated in Section 6.4.

It can also be seen in Fig. 6.10 that cylinder responses for $\zeta = 3\%$ and 5% are very different from those observed in $\zeta = 0$–1%. For these *high-damping cases*, without any sudden changes, $y_{0'}$ and f_y/f_N show smooth variations, with no upper branch occurring, only initial and lower branches are identified. Feng [57], Khalak and Williamson [59], Klamo et al. [62] and Soti et al. [63] also found that increasing the damping ratio (or the combined mass-damping parameter) can lead to the transition from three-branch to two-branch response. Since the condition of $f_y/f_N \cong 1$ does not satisfy, no classic lock-in domains are found for high structural damping values. This is in contrast to the phenomenon observed for $\zeta \leq 1\%$. Although Prasanth et al. [105] investigated the effect of mass ratio, they carried out CFD computations for $\zeta = 0.1\%$ and 10%. For $\zeta = 10\%$ they observed a similar phenomena; f_y/f_N increased almost linearly with U^*.

In order to show explicitly that the upper branch does not occur for $\zeta = 3\%$ and 5%, the time-averaged transverse and vortex phases are analyzed. As already discussed in Section 6.2, theoretically, the upper branch is characterized by abrupt phase jumps at its lower and higher boundaries. Although for zero damping ratio, the phase difference values of 0° and 180° are the only theoretically possible values [as shown by Eqs. (6.8) and (6.10)], for $\zeta > 0\%$ $\overline{\Phi}_y$ and $\overline{\Phi}_V$ are allowed to vary between 0° and 180°. Figures 6.12a and 6.12b show $\overline{\Phi}_y$ and $\overline{\Phi}_V$ against the reduced velocity for different damping ratio values. Similar to the notations employed in Fig. 6.9, filled and empty symbols refer to synchronous and non-synchronous cases. It can be seen in Fig. 6.12 that for relatively high cylinder displacements, time-averaged phase differences, especially $\overline{\Phi}_y$, do depend on structural damping. Similar to undamped vibrations, $\overline{\Phi}_V$ increases gradually at the initial↔upper branch transition range, while $\overline{\Phi}_y$ transitions at the boundary separating the upper and lower branches.

It is also seen in Fig. 6.12 that the change of $\overline{\Phi}_V$ through the initial↔upper branch transition range is a weak function of damping ratio. For instance, for $\zeta = 0.1\%$ $\overline{\Phi}_V$ changes by 175.08°, and for $\zeta = 1\%$ by 159.77°. However, the increment observed in $\overline{\Phi}_y$ depends strongly on ζ; for $\zeta = 0.1\%$ $\overline{\Phi}_y$ jumps roughly by $\Delta\overline{\Phi}_y \cong 158.1°$ and for $\zeta = 1\%$ only by $\Delta\overline{\Phi}_y \cong 43.4°$. Moreover, in high structural damping cases (at $\zeta = 3\%$ or 5%) jumps in $\overline{\Phi}$ disappear, resulting in an almost continuous increase of the time-averaged

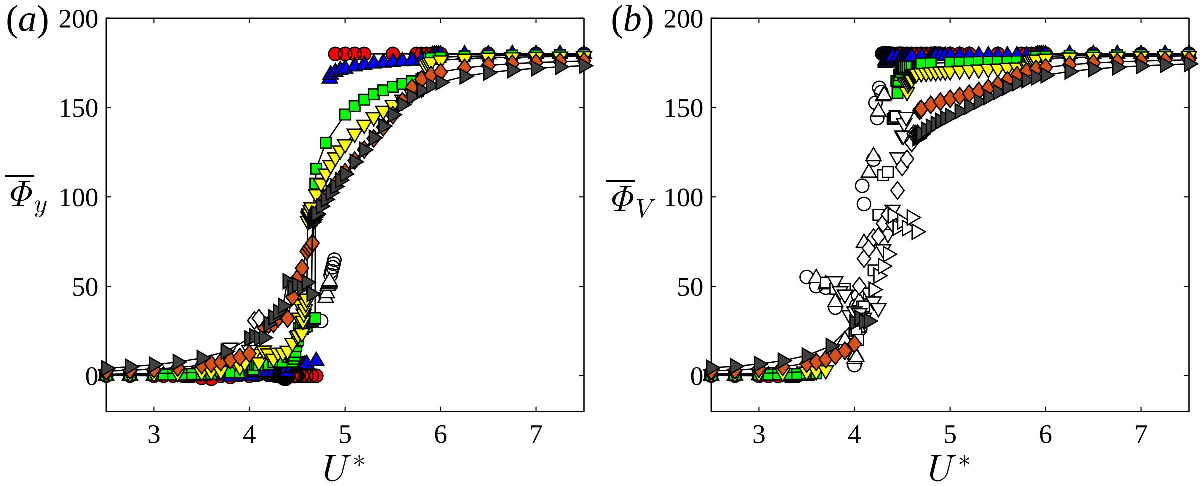

Figure 6.12: Time-mean values of transverse (a) and vortex phases (b) against reduced velocity for $\zeta = 0\%$ (●), 0.1% (▲), 0.5% (■), 1% (▼), 3% (◆) and 5% (◀). Filled and empty symbols refer to synchronous and non-synchronous cases, respectively.

phase angles. This finding compares qualitatively well with the experimental results of Soti et al. [63].

The lower limits of the upper and lower branches U^*_{UB} and U^*_{LB} and the widths of the upper branch $\varDelta U^* = U^*_{UB} - U^*_{LB}$ are summarized in Table 6.2. It can be seen that similarly to experimental results obtained at high Reynolds numbers [62, 63], the branching behavior is strongly influenced by the damping ratio. As we increase ζ, the width of the upper branch diminishes, and for $\zeta = 3\%$ and 5% it completely disappears, only the initial and lower branches remain. In other words, for low-damping cases ($\zeta \leq 1\%$) a three-branch response is identified, and for high-damping cases (at $\zeta = 3\%$ and 5%) a two-branch response is found. Klamo et al. [62] and Soti et al. [63] found a similar phenomenon in their experimental studies.

Table 6.2: Effect of damping ratio on cylinder response. Here U^*_{UB} and U^*_{LB} are the reduced velocity values where cylinder response shift to upper and lower branches, respectively.

ζ	U^*_{UB}	U^*_{LB}	ΔU^*
0%	4.00	4.89	0.88
0.1%	4.03	4.84	0.80
0.5%	4.06	4.69	0.63
1%	4.30	4.61	0.31
3%	–	4.68	–
5%	–	4.66	–

6.4 Analysis of hydrodynamic features

In Section 6.2 the harmonic oscillation model, applied to confirm the existence of the upper branch is shown. Rearranging Eq. (6.8), the following expression is obtained:

$$\hat{C}_y \sin \varPhi_y = 4\pi^3 \frac{f^*_y \hat{y}_0}{U^*} m^* \zeta. \tag{6.11}$$

This formula shows that $\hat{C}_y \sin \varPhi_y$ (responsible for the mechanical energy transfer) varies linearly with $f^*_y \hat{y}_0 / U^*$, where the proportionality factor is proportional to the mass-damping parameter $m^*\zeta$. Figure 6.13 shows $\hat{C}_y \sin \varPhi_y$ against $4\pi^3 f^*_y \hat{y}_0 / U^*$ for different damping values between $\zeta = 0\%$ and 5% and constant $m^* = 10$. Empty and filled symbols refer to data points belonging to the upper and lower branches, respectively. Dashed lines represent the results from the harmonic oscillator model [described by Eq. (6.11)], and the numbers (belonging to the dashed lines) show structural damping ratio values. It can be seen in Fig. 6.13 that harmonic approximation seems to be very accurate in the lower branch and at the beginning of the upper branch. However, at the remaining part of the upper branch the results are very far from the harmonic solutions, which suggests that in these domains the transverse fluid force is not harmonic function of time. The results presented earlier are consistent with this proposal. For undamped vibrations I found very high detuning values (around $f^*_y - f^*_{C_y} = -0.2$) in the range of $4.7 < U^* \leq 4.89$, which may refer to that the most remarkable frequency in the spectra of C_y equals to the double of the vibration frequency. Besides, in the domain of $4.36 < U^* \leq 4.7$ the time-dependent transverse phase shows unreasonably high fluctuations, which may also indicate the occurrence of higher order harmonics in the spectra of transverse fluid force. In order to confirm the non-harmonic nature of C_y (in some ranges), time histories and frequency spectra of cylinder displacement and transverse fluid force are further analyzed.

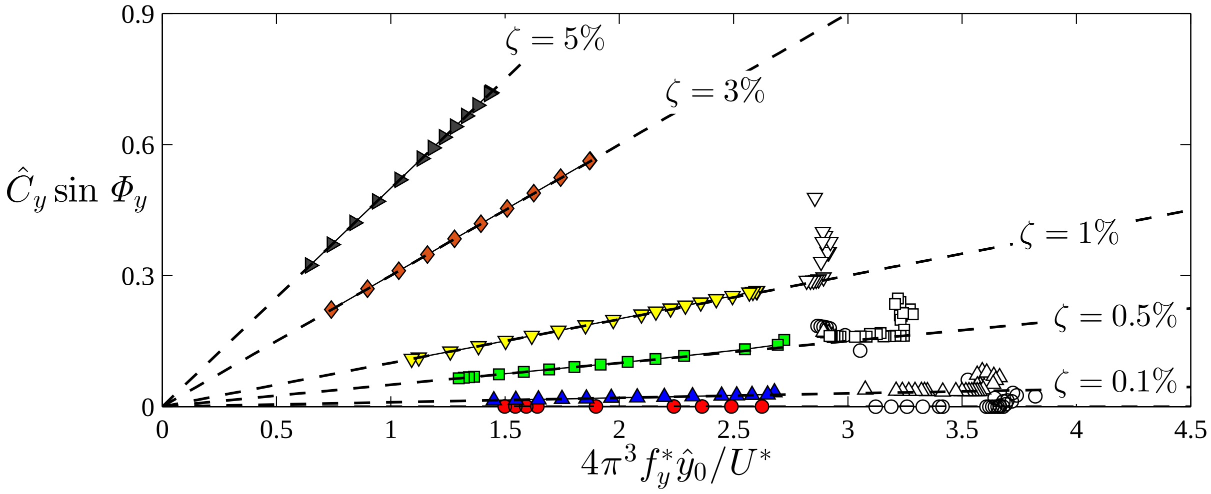

Figure 6.13: $\hat{C}_y \sin \Phi$ against $4\pi^3 f^* \hat{y}_0 / U^*$ in the upper branch (empty symbols) and in the lower branch (filled symbols) for $\zeta = 0\%$ (-●-), 0.1% (-▲-), 0.5% (-■-), 1% (-▼-), 3% (-◆-) and 5% (-◀-). The dashed lines represent solutions obtained from the harmonic oscillator model given by Eq. (6.11)

The analyses are carried out first for undamped cylinder vibrations, and than for non-zero damping ratio values.

6.4.1 Undamped cylinder vibration

Figure 6.14 shows the time histories of non-dimensional cylinder displacement (left-hand side of the figure) and transverse fluid force (middle) at different U^* values in the initial (see Fig. 6.14a), upper (Figs. 6.14b-6.14e), and lower branches (Fig. 6.14f) for $\zeta = 0\%$. Frequency spectra of the signals (displacement and transverse fluid force) normalized by the cylinder's natural frequency in vacuum obtained using Fast Fourier Transform (FFT) are shown in the right plots of the figures. Here PSD denotes *Power Spectral Density*, and vertical axis has logarithmic scale.

It can be seen in Fig. 6.14a that the signals show quasi-periodic nature in the initial branch ($3.45 < U^* \leq 4$); y_0 and C_y contain multiple frequency components. This is the reason why the time-dependent transverse phase shows random fluctuations in the same reduced velocity range (see Fig. 6.3c). At $U^* = 4$ high jumps are observed in $y_{0'}$ and f_y/f_N (Fig. 6.1), at the location where the cylinder response shifts from the initial to the upper branch. The high cylinder displacement in the upper branch can observed in Fig. 6.14b. This figure shows also that in the domain of $4 < U^* \leq 4.28$, the cylinder motion and the transverse fluid force are quasi-periodic signals. These effects are expected, because in this range the time-dependent transverse phase shows random variation (see Fig. 6.5). Due to the quasi-periodic behavior, the frequency spectra of y_0 and C_y contain multiple frequency components from which $f/f_N \cong 1$ and 3 have the highest PSD values. Note that $f/f_N \cong i$ frequency peak is usually referred to as the i^{th} harmonic frequency component. Between the reduced velocity values of $U^* = 4.29$ and 4.35 the time-dependent phase differences show periodic variations (see Fig. 6.7a), which refers to periodic cylinder vibrations. It can be seen in Fig. 6.14c that both y_0 and C_y are periodic signals; transverse fluid force contains relevant frequency components at $f/f_N \cong 1$ (highest intensity) and 3 (relatively low intensity), while in the spectrum of cylinder displacement only $f/f_N \cong 1$ is identified.

Increasing the reduced velocity from $U^* = 4.36$ to 4.48, slightly above the jumps found in $C_{y'}$ and $C_{V'}$ (see Fig. 6.2), the transverse fluid force and the cylinder displacement become quasi-periodic again (Fig. 6.14d). These signals show similar behaviors to the time-dependent phases, in the same U^* domain random oscillations have been found in

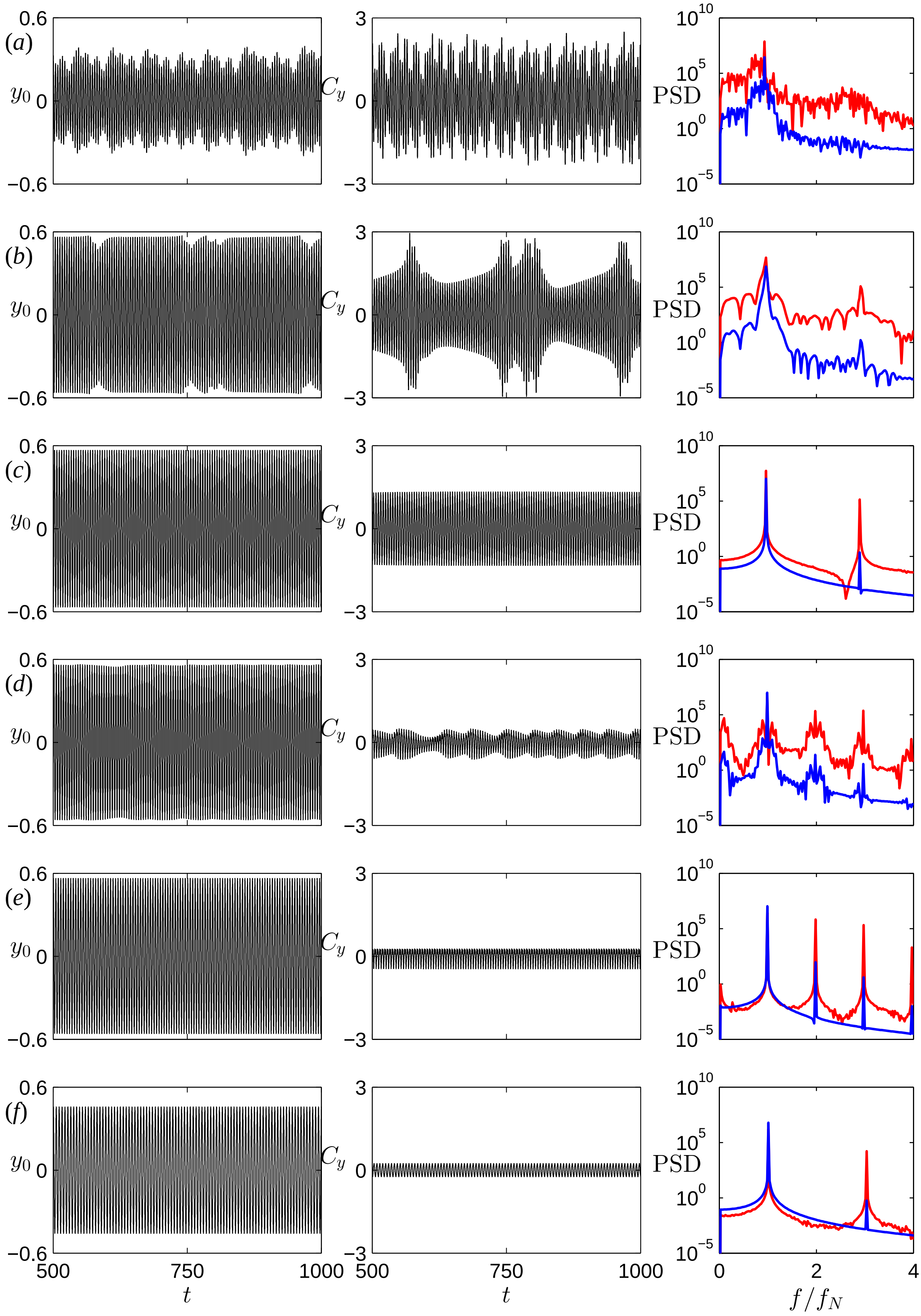

Figure 6.14: Time histories (left and middle) and Fourier spectra (right) of cylinder displacement and transverse fluid force at $U^* = 4$ (a), 4.2 (b), 4.3 (c), 4.4 (d), 4.6 (e) and 5.5 (f) for $\zeta = 0$. In the FFT spectra red and blue colors indicate the frequency spectra of transverse fluid force and cylinder displacement, respectively.

Φ_y and Φ_V. Besides, in the frequency spectra of C_y the first, the second and the third harmonic components are identified as high-intensity peaks. Varying the reduced velocity in the range of $4.48 < U^* \leq 4.89$, C_y is found to be periodic again and the $f/f_N \cong 2$ frequency component is found to play very significant role in its spectra (see Fig. 6.14e). This finding, which we expected, explains why the computational results do not agree with the harmonic solutions represented by Eq. (6.11) at some parts of the upper branch (see Fig. 6.13), and implies why the transverse phase shows unreasonably high fluctuations between $U^* = 4.36$ and 4.7 (Fig. 6.7c).

Many studies have been dealing with the frequency components occurring in the spectra of transverse fluid force. Without aiming to give an exhaustive list, Jauvtis and Williamson [85], Dahl et al. [81], Dahl et al. [82], Dahl et al. [41], Wang et al. [84] have discussed the relevance of the first and the third harmonic components in C_y for two-degree-of-freedom vortex-induced vibrations. However, the second harmonic component is not so typical in VIV. Bao et al. [83] investigated also two degrees of freedom VIV and they identified the $f/f_N \cong 2$ frequency peak in the spectra of C_y. In Chapter 4 I showed that the second harmonic frequency component has a fundamental effect on the path of the cylinder; asymmetric raindrop-shaped cylinder paths occur in these cases. These results have been published in Dorogi and Baranyi [J3].

In the lower branch (from $U^* = 4.9$ to 5.9) both y_0 and C_y are periodic signals. As seen in Fig. 6.14f, the second harmonic component completely disappears, only $f/f_N \cong 1$ and 3 peaks remain (see Fig. 6.14f). Since the intensity of $f/f_N \cong 3$ is much lower than the PSD of the first harmonic component, the $f/f_N \cong 3$ peak influences the vibration very slightly. This is why the data points corresponding to the lower branch fit very well on the model results based on the harmonic approximations (see Fig. 6.13).

As can be seen in Fig. 6.4, high detuning value of $f_y^* - f_{C_y}^* \cong -0.2$ occurs in the range of $4.7 < U^* < 4.89$ for zero structural damping ratio, which value agrees approximately with the Strouhal number at Re = 300. Since the vibration frequency in this range is also close to the Strouhal number, this detuning value can only be reached when the second harmonic frequency component is the most dominant in the spectra of C_y. Although I showed that $f/f_N \cong 2$ occurs in the upper branch, it was not confirmed whether it is the most relevant harmonic in the domain of $4.7 < U^* \leq 4.89$. Figure 6.15 shows the frequency spectra of transverse fluid force at different U^* values, where Power Spectral Density normalized by the maximum PSD in the spectra $\mathrm{PSD_{norm}} = \mathrm{PSD}/\mathrm{PSD_{max}}$ is plotted against f/f_N. Note that vertical axis is scaled linearly. It can be seen that at $U^* = 4.5$ (see Fig. 6.15a) $f/f_N \cong 1$ is the most intensive peak, while the normalized PSD at $f/f_N \cong 2$ is low. As expected, in the range of $4.7 < U^* \leq 4.89$ the roles of the first and second harmonic components are switched; $f/f_N \cong 2$ is the most dominant, while the normalized PSD of $f/f_N \cong 1$ is relatively low (see Figs. 6.15b and 6.15c). However, switching to the lower branch causes a dramatic change in the FFT of C_y. As shown in Fig. 6.15d, the second harmonic component completely disappears and the first and third harmonic components remain in the spectra ($f/f_N \cong 1$ is the most relevant component).

Singh and Mittal [72], Prasanth and Mittal [88] and Bahmani and Akbari [70] found that the formation of vortices shedding from the body is very sensitive to the value of the reduced velocity. Figure 6.16 shows the vortex structures at the same U^* values where the time histories and the FFT spectra of the cylinder displacement and transverse fluid force were previously analyzed (see Fig. 6.14). As shown in Fig. 6.14a, y_0 and C_y are quasi-periodic signals in the initial branch, that is, the vortex structures at the corresponding reduced velocity values change dynamically with time (see Fig. 6.16a).

Shifting to the upper branch, in the range of $4 < U^* \leq 4.28$ the cylinder motion and the fluid force coefficients are still quasi-periodic signals, that is, the vortex structure is also highly time-dependent in this domain (see Fig. 6.16b). It was found that the time histories of y_0 and C_y are periodic between $U^* = 4.29$ and 4.35, and the FFT spectra of C_y contain relevant frequency peaks at $f/f_N = 1$ and 3 (Fig. 6.14c). It can be seen in Fig. 6.16c that in the corresponding range $2P_O$ wake mode seems to develop, which means that two pairs of vortices are shed from the cylinder in each motion period, but the secondary vortex in each pair is much weaker than the primary vortex [106]. Morse and Williamson [106] found that when the vortex pair is moving downstream from the cylinder, the secondary vortex decays, which is also seen in Fig. 6.16c. Khalak and Williamson [107] and Khalak and Williamson [59] identified 2P vortex shedding mode in the upper branch, where the strengths of the primary and the secondary vortex are approximately identical. It has to be noted that $2P_O$ vortex structure has not been found for such low Reynolds number cases.

At the closing part of the upper branch ($4.35 < U^* \leq 4.89$), the $f/f_N \cong 2$ peak was found to occur, which strongly influences the vortex structure. Although the structure of vortices changes in time between $U^* = 4.35$ and 4.48, due to the modulations in the aerodynamic force coefficients, the wake modes are very similar to the P+S vortex shedding mode (Fig. 6.16d). Here P+S denotes that a pair of vortices and a single vortex are shed from the cylinder. In the domain of $4.48 < U^* \leq 4.89$ (still belongs to the upper branch) the time traces of y_0 and C_y return back to periodic. In this range the second harmonic frequency component plays an important role in C_y (see Fig. 6.15), which seems to make the vortex structure asymmetric: stable P+S modes are found in the domain of $4.48 < U^* \leq 4.89$ (see Fig. 6.16e). Such effect of $f/f_N \cong 2$ on the vortex shedding was shown earlier in Chapter 4.

As shown in Figs. 6.14 and 6.15, in the lower branch the $f/f_N \cong 2$ frequency peak

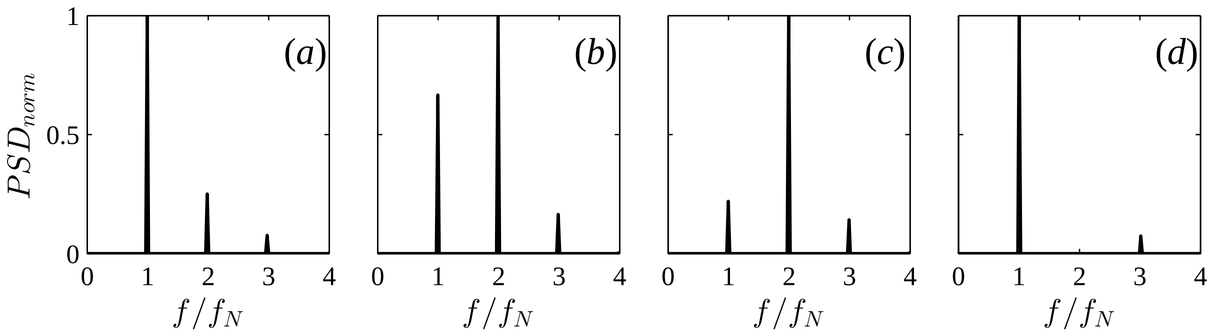

Figure 6.15: Frequency spectra of transverse fluid force at $U^* = 4.5$ (a), 4.8 (b), 4.89 (c) and 4.9 (d) for $\zeta = 0\%$

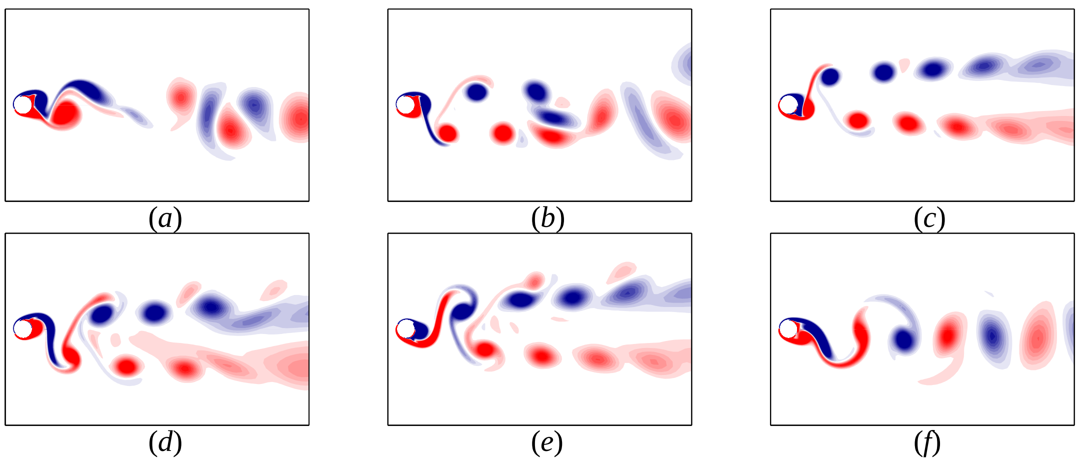

Figure 6.16: Vortex structures (red: positive vorticity, blue: negative) at $U^* = 4$ (a), 4.2 (b), 4.3 (c), 4.4 (d), 4.6 (e) and 5.5 (f) for $\zeta = 0$. Each vortex contours are recorded at random phases of the cylinder oscillation

completely disappears from the spectra of C_y. For this reason the vortex structure becomes symmetric; 2S wake modes (two single vortices) are found in this domain ($4.89 < U^* \leq 5.9$, see Fig. 6.16f).

6.4.2 Damped cylinder vibrations

It was shown in Section 6.3 that increasing the structural damping leads to the transition from three-branch to two-branch response. While initial, upper and lower branches are found for $\zeta \leq 1\%$ at Re = 300, only initial and lower branches are observed for $\zeta = 3\%$ and 5%. It can be seen in Fig. 6.11c that no unbounded increase appears in the transverse phase at the boundary separating the upper and lower branches for $\zeta = 0.5\%$. This finding is in contrast to what I found for undamped vibrations (see Fig. 6.7d).

It was confirmed in Section 6.4.1 that the unbounded increase of the transverse phase is caused by the fact that the second harmonic frequency component is the most dominant in the spectrum of C_y. For this reason, the lack of unbounded variation in Φ_y for $\zeta = 0.5\%$ suggests that the intensity of $f/f_N \cong 2$ is not the highest in the upper↔lower branch transition range. Figure 6.17 shows the normalized spectra of transverse fluid force at different reduced velocity values in the upper branch for $\zeta = 0.5\%$. This figure corroborates the former assumption; the role of $f/f_N \cong 2$ increases with U^* but at the boundary between the upper and lower branches (at $U^* = 4.688$, see Fig. 6.17d) the first harmonic component dominates all over the spectra, and $f/f_N \cong 2$ occurs only with low intensity. The additional findings related to e.g. the vortex formation downstream from the cylinder hold true in the range of $\zeta \leq 1\%$, where three-branch responses are found.

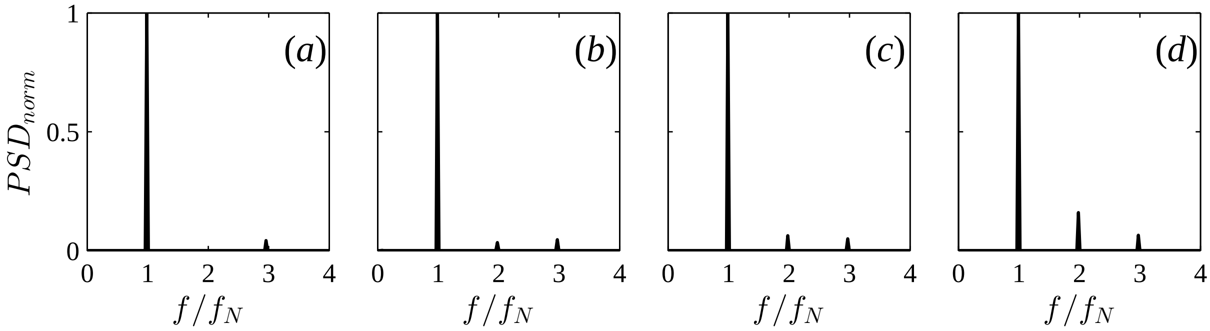

Figure 6.17: Frequency spectra of transverse fluid force at $U^* = 4.5$ (a), 4.56 (b), 4.6 (c) and 4.688 (d)

As mentioned earlier, increasing the structural damping ratio over $\zeta = 1\%$, only the initial and lower branches are found, the upper branch disappears from the response. The question arises what the difference is between three and two-branch responses in terms of frequency spectra and vortex structures. Figure 6.18 shows the frequency spectra of cylinder displacement and transverse fluid force (top row), and vortex contours (bottom row) at different reduced velocity values for $\zeta = 3\%$. As can be seen in Fig. 6.18a, the FFT spectra of the transverse fluid force and cylinder displacement for $U^* = 4.2$ contains several frequency components, that is, y_0 and C_y are quasi-periodic signals. Due to the same reason, the vortex structure is highly time dependent at this point, but very similar to the regular 2S vortex shedding mode. The above mentioned flow and vibration characteristics between the reduced velocity values of $U^* = 4$ and 4.66 are similar to those of the initial branch in the $\zeta \leq 1\%$ domain. Increasing reduced velocity up to $U^* = 4.68$, the cylinder response reaches the lower branch where both y_0 and C_y return back to periodic. In contrast to the results reported in the low-damping domain, the vibration frequency does not lock exactly to the natural frequency of the system in vacuum (see also Fig. 6.10). Figures 6.18b and 6.18c show the spectra of y_0 and C_y in the range where the oscillation amplitude is relatively high. As seen, the first and the third harmonic frequency components can be found in the spectra of C_y. Since the peak of $f/f_N \cong 2$ is not present in the spectra, 2S vortex structures are found in these computational points.

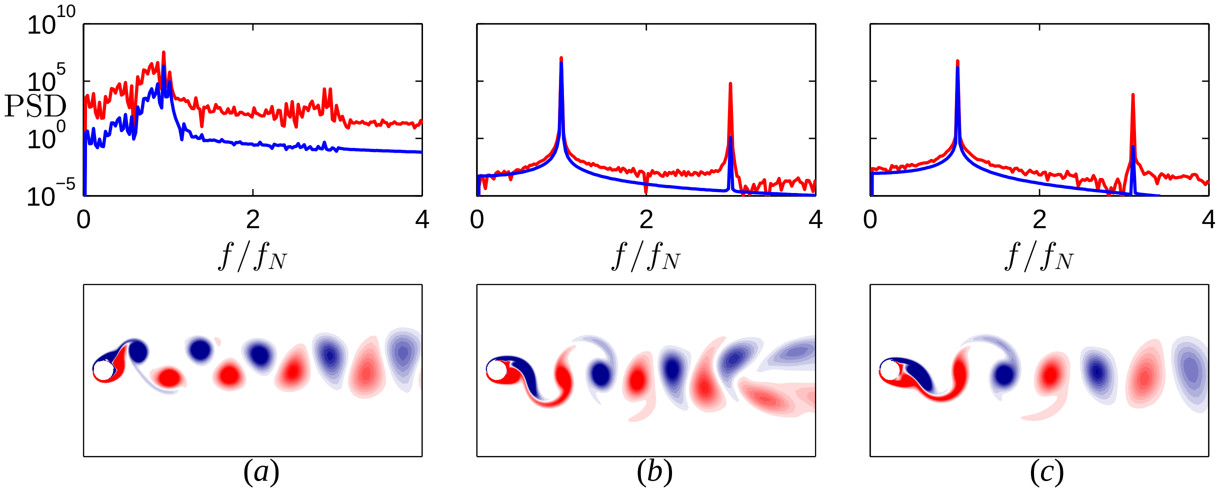

Figure 6.18: Frequency spectra of cylinder displacement (blue curves) and transverse fluid force (red curves), and the vorticity contours at $U^* = 4.2$ (a), 4.68 (b) and 5.4 (c) for $\zeta = 3\%$. Each snapshots are recorded at random phases of the cylinder oscillation

6.5 New scientific contributions

Contribution V

Up until now an upper branch (i.e. a three-branch cylinder response) has been reported only for high-Reynolds number flows (Re $= 10^3$–10^4). Using two-dimensional CFD simulations I showed that the cylinder response (oscillation amplitude and frequency) plotted against the reduced velocity U^* displays a three-branch behavior at the Reynolds number of Re $= 300$, and mass and structural damping ratio values of $m^* = 10$ and $\zeta = 0\%$, respectively. The initial branch takes place in the range of $3.45 < U^* \leq 4$, the upper branch is observed between $U^* = 4$ and 4.89, and the lower branch occurs in the domain of $4.89 < U^* \leq 5.9$. I found that the time-averaged phase differences of the vortex force and the transverse fluid force relative to the cylinder displacement show gradual variations between approximately 0° and 180° at the upper and lower boundaries of the upper branch, respectively. I observed unbounded variations and phase slips in the time-dependent phase angle values, which explains the gradual changes in their time-mean values.

I found that increasing the structural damping ratio leads to the transition from three-branch to two-branch response. This finding is comparable to the experimental results (available in the literature) at high Reynolds numbers. In the domain of $\zeta \leq 1\%$ the upper branch is found to occur whose reduced velocity range ΔU^*_{UB} decreases with the damping ratio (e.g. $\Delta U^*_{UB} = 0.88$ for $\zeta = 0\%$, while $\Delta U^*_{UB} = 0.31$ for $\zeta = 1\%$). For $\zeta = 3\%$ and 5%, the upper branch completely disappears from the response, only the initial and lower branches remain.

Related publications: Dorogi and Baranyi [J4], Dorogi and Baranyi [C10] and Dorogi and Baranyi [C9]

Contribution VI

I showed that the phase difference of the transverse fluid force relative to the cylinder displacement (i.e. the transverse phase) increases roughly uniformly with time at the end of the upper branch ($4.7 < U^* \leq 4.89$) for $\mathrm{Re} = 300, m^* = 10$ and $\zeta = 0\%$. This effect is caused by the large detuning value between the frequencies of cylinder vibration f_y^* and transverse fluid force $f_{C_y}^*$; $f_y^* - f_{C_y}^* \cong -0.2$, which in absolute value is close to the Strouhal number St at $\mathrm{Re} = 300$. Since $f_y^* \cong \mathrm{St}$ between $U^* = 4.7$ and 4.89, the detuning value $f_y^* - f_{C_y}^* \cong -\mathrm{St}$ can only be achieved when $f_{C_y}^* = 2f_y^* \cong 2\mathrm{St}$. The frequency spectra of the transverse fluid force confirms the non-harmonic nature of the transverse fluid force. I found that the second harmonic frequency component is the most intensive peak in the range of $4.7 < U^* \leq 4.89$ for $\zeta = 0\%$.

Increasing the structural damping ratio value up to $\zeta = 0.5\%$, I showed that the detuning value is zero $f_y^* - f_{C_y}^* = 0$ in the entire reduced velocity domain, hence the time-dependent transverse phase no longer shows unbounded increase at the higher end of the upper branch. This effect implies that the role of the second harmonic frequency component decreases with the structural damping ratio. The spectral analyses of the transverse fluid force showed that the intensity of the second harmonic component was negligible.

The currently obtained CFD data belonging to various structural damping ratio values (between $\zeta = 0\%$ and 5%) have been compared to the results using the harmonic oscillator model. I showed that the computational and the harmonic model results compare very well at the beginning of the upper branch and in the lower branch. However, at the end of the upper branch the CFD data and and the harmonic model results are far from each other. This finding confirms my previous statement concerning the non-harmonic nature of the transverse fluid force at the end of the upper branch.

Related publications: Dorogi and Baranyi [J4], Dorogi and Baranyi [C10] and Dorogi and Baranyi [C9]

Chapter 7

Possible future works

In this PhD dissertation various types of vortex-induced vibrations are investigated, including the single-degree-of-freedom motions, where the cylinder is allowed to move only in streamwise or transverse directions, and two-degree-of-freedom vibration cases. Although several analyses have been performed in the dissertation, there are still a lot of unanswered questions, which can lead to further investigations. These topics related directly to my researches are summarized in the following points:

- In Chapter 4 computational results have been presented for the cases, when the natural frequencies in streamwise and transverse directions f_{Nx} and f_{Ny} are identical. The question arises what the effect of the natural frequency ratio $\mathrm{FR} = f_{Nx}/f_{Ny}$ is on the cylinder response. Preliminary results are available in this topic [J2] (indicating that FR highly influences the cylinder path), but additional computations are required.

- As discussed in Chapter 5, a single excitation region occurs for streamwise-only vortex-induced vibrations in the low-Reynolds number domain. However, at moderately high Reynolds numbers two response branches have been identified. In order to investigate how the response switches between one-branch and two-branch responses, three-dimensional computations are needed. This can be carried out using either commercial softwares (e.g. ANSYS FLuent or ANSYS CFX) or open-source CFD codes (e.g. OpenFOAM, Nektar++ or Nek5000).

- It was shown that a separate upper branch occurs at the Reynolds number of 300 (see Chapter 6). However, at lower Re values (e.g. at $\mathrm{Re} = 100$) two response branches (i.e. the initial and lower branches) have been reported in the literature. I aim to perform CFD computations at different Reynolds numbers ranging between $\mathrm{Re} = 50 - 300$ to find the critical Reynolds number value Re_c, above which three-branch response occurs, but at $\mathrm{Re} < \mathrm{Re}_c$ only the initial and lower branches can be identified.

During the literature review I realized that vortex-induced vibrations of a circular cylinder placed into an oscillatory flow received less attention. However, it appears in many engineering fields, for example the wave motions are commonly modeled with oscillatory flows. To my best knowledge, very few paper examine this problem numerically. For this reason, systematic CFD computations are planned in this field in the near future.

Bibliography

Journal papers

[J1] Dorogi, D. and Baranyi, L., 2018. Numerical simulation of a freely vibrating circular cylinder with different natural frequencies. *Ocean Engineering* **158**, 196–207. DOI: 10.1016/j.oceaneng.2018.03.079.

[J2] Dorogi, D. and Baranyi, L., 2019. Effects of natural frequency ratio on fluid flow around a freely vibrating circular cylinder (in Hungarian). *Jelenkori Társadalmi és Gazdasági Folyamatok* **14**(1), 19–27.

[J3] Dorogi, D. and Baranyi, L., 2019. Occurrence of orbital cylinder motion for flow around freely vibrating circular cylinder in uniform stream. *Journal of Fluids and Structures* **87**, 228–246. DOI: 10.1016/j.jfluidstructs.2019.03.004.

[J4] Dorogi, D. and Baranyi, L., Identification of upper branch for vortex-induced vibration of a circular cylinder at Re=300. *Submitted to Journal of Fluids and Structures.*

[J5] Konstantinidis, E., Dorogi, D., and Baranyi, L., Resonance in vortex-induced in-line vibration at low Reynolds numbers. *Submitted to Journal of Fluid Mechanics.*

Conference Papers

[C1] Baranyi, L. and Dorogi, D., 2016. Effect of frequency ratio on flow around a cylinder oscillated in-line at $Re = 80-200$. In: *Proceedings of the MultiScience - XXX. microCAD International Multidisciplinary Scientific Conference.* Miskolc, Hungary, on CD-ROM, pp. 1–8.

[C2] Dorogi, D. and Baranyi, L., 2016. Effect of gradual amplitude increase on flow around a cylinder oscillated in line. In: *Proceedings of the* 4^{th} *International Scientific Conference on Advances in Mechanical Engineering (ISCAME 2016).* Debrecen, Hungary, pp. 151–156.

[C3] Dorogi, D. and Baranyi, L., 2016. Richardson extrapolation for simulation of laminar flow past a circular cylinder. In: *Proceedings of the MultiScience – XXX. microCAD International Multidisciplinary Scientific Conference (microCAD).* Miskolc, Hungary, on CD-ROM, pp. 1–8.

[C4] Dorogi, D. and Baranyi, L., 2017. Elastically supported cylinder in two-degree-of-freedom motion: a numerical study. In: *Proceedings of the MultiScience – XXXI. microCAD International Multidisciplinary Scientific Conference (microCAD).* Miskolc, Hungary, pp. 93–100.

[C5] Dorogi, D. and Baranyi, L., 2017. Numerical simulation of flow and heat transfer for a cylinder in free vibration. In: *Proceedings of the MultiScience – XXXI. microCAD International Multidisciplinary Scientific Conference (microCAD).* Miskolc, Hungary, pp. 101–108.

[C6] Dorogi, D. and Baranyi, L., 2018. Effect of streamwise and transverse damping on flow around an elastically supported cylinder. In: *Proceedings of the Conference on Modelling Fluid Flow (CMFF'18).* Budapest, Paper number: 21, pp. 1–8.

[C7] Dorogi, D. and Baranyi, L., 2018. Natural frequency effect on the path of an elastically supported circular cylinder. In: *Proceedings of the Conference on Modelling Fluid Flow (CMFF'18)*. Budapest, Paper number: 89, pp. 1–8.

[C8] Dorogi, D. and Baranyi, L., 2018. Numerical investigation of the path of a freely vibrating circular cylinder at high reduced frequency value. In: *Proceedings of the* 7^{th} *Conference on Bluff Body Wakes and Vortex-Induced Vibrations (BBVIV7)*. Carry-le-Rouet, France, pp. 121–124.

[C9] Dorogi, D. and Baranyi, L., 2019. Damping effects for a freely vibrating cylinder in transverse direction: a CFD study. In: *Proceedings of the* 27^{th} *International Conference on Mechanical Engineering (OGĚT2019)*. Oradea, Romania, pp. 99–102.

[C10] Dorogi, D. and Baranyi, L., 2019. Investigation of the branching behavior of a freely vibrating circular cylinder at low Reynolds numbers. In: *Proceedings of the* 4^{th} *International Conference on Multi-scale Computational Methods for Solids and Fluids (ECCOMAS MSF 2019)*. Sarajevo, Bosnia-Herzegovina, pp. 108–111.

[C11] Dorogi, D., Baranyi, L., and Konstantinidis, E., 2019. Effect of mass ratio on inline vortex induced vibrations at a low Reynolds number. In: *Proceedings of the Flow-Structure Sound Interactions and Control (FSSIC2019)*. Chania, Crete Island, Greece, Paper number: 90, pp. 1–5.

[C12] Dorogi, D., Konstantinidis, E., and Baranyi, L., 2019. Numerical investigation of streamwise vortex-induced vibration at low Reynolds numbers: mass ratio effects. In: *Proceedings of the* 4^{th} *International Conference on Multi-scale Computational Methods for Solids and Fluids (ECCOMAS MSF 2019)*. Sarajevo, Bosnia-Herzegovina, pp. 112–115.

Papers not related to the dissertation

[O1] Dorogi, D. and Bencs, P., 2015. Measurement of velocity distribution in a subsonic wind tunnel using LDA measurement technique (in Hungarian). In: *Proceedings of* 20^{th} *International Scientific Conference of Young Engineers*. Cluj Napoca, Romania, pp. 127–130.

[O2] Szaszák, N., Dorogi, D., Roloff, C., Thévenin, D., and Szabó, S., 2015. Investigation of the moving trajectories in an active turbulence generator (in Hungarian). *Multidiszciplináris Tudományok* **4**, 103–114.

[O3] Dorogi, D., Bolló, B., and Szabó, S., 2019. Effects of external disturbances on the performance of an axial cooling fan. *Analecta Technica Szegedinensia* **13**(1), 48–55. DOI: 10.14232/analecta.2019.1.48-55.

References

[1] Nishihara, T., Kaneko, S., and Watanabe, T., 2005. Characteristics of fluid dynamic forces acting on a circular cylinder oscillated in the streamwise direction and its wake patterns. *Journal of Fluids and Structures* **20**(4), 505–518. DOI: 10.1016/j.jfluidstructs.2005.02.003.

[2] Bernitsas, M., Raghavan, K., Ben-Simon, Y., and Garcia, E., 2008. VIVACE (Vortex Induced Vibration Aquatic Clean Energy): a new concept in generation of clean and renewable energy from fluid flow. *Journal of Offshore Mechanics and Arctic Engineering* **130**(4), 041101 (15 pages). DOI: 10.1115/1.2957913.

[3] Bernitsas, M., Ben-Simon, Y., Raghavan, K., and Garcia, E., 2009. The VIVACE converter: model tests at high damping and Reynolds number around 10^5. *Journal of Offshore Mechanics and Arctic Engineering* **131**(1), 011102 (12 pages). DOI: 10.1115/1.2979796.

[4] Mehmood, A., Abdelkefi, A., Hajj, M., Nayfeh, A., Akhtar, I., and Nuhait, A., 2013. Piezoelectric energy harvesting from vortex-induced vibrations of a circular cylinder. *Journal of Sound and Vibration* **332**(19), 4656–4667. DOI: 10.1016/j.jsv.2013.03.033.

[5] Strouhal, V., 1878. ´Uber eine besondere Urt der Tonerregung. *Annalen der Physik und Chemie (Liepzig)* **Bd.5**(10), 216–251.

[6] Rayleigh, L. The Theory of Sound. 2nd Edition, Vol. II, Section 372. New York: Dover (1945), 1896.

[7] Rayleigh, L., 1915. Aeolian Tones. *Philosophical Magasine* **XXIX**, 433–453.

[8] Roshko, A., 1954. On the Development of Turbulent Wakes from Vortex Streets. *National Advisory Committee for Aeronautics*, 1191.

[9] Tritton, D., 1959. Experiments on the flow past a circular cylinder at low Reynolds numbers. *Journal of Fluid Mechanics* **6**, 547–567. DOI: 10.1017/S0022112059000829.

[10] Williamson, C., 1989. Oblique and parallel modes of vortex shedding in the wake of a circular cylinder a low Reynolds numbers. *Journal of Fluid Mechanics* **206**, 579–627. DOI: 10.1017/S0022112089002429.

[11] Williamson, C. and Brown, G., 1998. A series in $1/\sqrt{(}\mathrm{Re})$ to represent the Strouhal-Reynolds number relationship of the cylinder wake. *Journal of Fluids and Structures* **12**(8), 1073–1085. DOI: 10.1016/S0889-9746(88)90058-8.

[12] Henderson, R., 1997. Nonlinear dynamics and pattern formation in turbulent wake transition. *Journal of Fluid Mechanics* **352**, 65–112. DOI: 10.1017/S0022112097007465.

[13] Kovásznay, L., 1949. Hot-wire investigation of the wake behind cylinders at low Reynolds numbers. *Proceedings of the Royal Society of London, Series A* **198**(1053), 174–190. DOI: 10.1098/rspa.1949.0093.

[14] Thompson, M. and Le Gal, P., 2004. The Stuart-Landau model applied to wake transition revisited. *European Journal of Mechanics – B/Fluids* **23**(1), 219–228. DOI: 10.1016/j.euromechflu.2003.09.012.

[15] Baranyi, L. and Lewis, R., 2006. Comparison of grid-based CFD method and vortex dynamics predictions of low Reynolds number cylinder flows. *The Aeronautical Journal* **110**, 63–71. DOI: 10.1017/S0001924000004371.

[16] Barkley, D. and Henderson, R., 1996. Three dimensional Floquet stability analysis of the wake of a circular cylinder. *Journal of Fluid Mechanics* **322**, 215–241. DOI: 10.1017/S0022112096002777.

[17] Posdziech, P. and Grundmann, R., 2007. A systematic approach to the numerical calculation of fundamental quantities of the two-dimensional flow over a circular cylinder. *Journal of Fluids and Structures* **23**(3), 479–499. DOI: 10.1016/j.jfluidstructs.2006.09.004.

[18] Ye, T., Mittal, R., Udaykumar, H., and Shyy, W., 1999. An accurate Cartesian grid method for viscous incompressible flows with complex immersed boundaries. *Journal of Computational Physics* **156**, 209–240.

[19] Lai, M. and Peskin, C., 2000. An immersed boundary method with formal second-order accuracy and reduced numerical viscosity. *Journal of Computational Physics* **160**, 705–719.

[20] Baranyi, L. and Shirakashi, M., 1999. Numerical solution for laminar unsteady flow about fixed and oscillating cylinders. *Comuter Assisted Mechanics and Engineering Sciences* **6**, 263–277.

[21] Lima E Silva, A., Silveira-Neto, A., and Damasceno, J., 2003. Numerical simulation of two-dimensional flows over a circular cylinder using the immersed boundary method. *Journal of Computational Physics* **189**(2), 351–370. DOI: 10.1016/S0021-9991(03)00214-6.

[22] Bolló, B. Numerical investigation of flow around and heat transfer from a heated circular cylinder (in Hungarian). PhD dissertation. University of Miskolc, 2013.

[23] Norberg, C., 2003. Fluctuating lift on a circular cylinder: review and new measurements. *Journal of Fluids and Structures* **17**(1), 57–96. DOI: 10.1016/S0889-9746(02)00099-3.

[24] Sumer, B. and Fredsoe, J. Hydrodynamics around cylindrical structures. World Scientific, Singapore, 1997.

[25] Bearman, P. and Obasaju, E., 1982. An experimental study of pressure fluctuations fixed and oscillating square-section cylinders. *Journal of Fluid Mechanics* **119**, 297–321. DOI: 10.1017/S0022112082001360.

[26] Koide, M., Tomida, S., Takahashi, T., Baranyi, L., and Shirakashi, M., 2002. Influence of cross-sectional configuration on the synchronization of Kármán vortex shedding with the cylinder oscillation. *JSME International Journal, Series B* **45**(2), 249–258. DOI: 10.1299/jsmeb.45.249.

[27] Poncet, P., 2002. Vanishing of mode B in the wake behind a rotationally oscillating circular cylinder. *Physics of Fluids* **14**(6), 2021–2023. DOI: 10.1063/1.1479344.

[28] Williamson, C. and Roshko, A., 1988. Vortex formation in the wake of an oscillating cylinder. *Journal of Fluids and Structures* **2**(4), 355–381. DOI: 10.1016/S0889-9746(88)90058-8.

[29] Meneghini, J. and Bearman, P., 1995. Numerical simulation of high amplitude oscillatory flow about a circular cylinder. *Journal of Fluids and Structures* **9**, 435–455. DOI: doi.org/10.1006/jfls.1995.1025.

[30] Blackburn, H. and Henderson, R., 1999. A study of two-dimensional flow past an oscillating cylinder. *Journal of Fluid Mechanics* **385**, 255–286. DOI: 10.1017/S0022112099004309.

[31] Leontini, J., Stewart, B., Thompson, M., and Hourigan, K., 2006. Wake state and energy transitions of an oscillating cylinder at low Reynolds number. *Physics of Fluids* **18**, 067101 (9 pages). DOI: 10.1063/1.2204632.

[32] Baranyi, L. and Daróczy, L., 2013. Mechanical energy transfer and flow parameter effects for a cylinder in transverse oscillation. *International Journal of Heat and Fluid Flow* **43**, 251–258. DOI: 10.1016/j.ijheatfluidflow.2013.05.009.

[33] Al-Mdallal, Q., Lawrence, K., and Kocabiyik, S., 2007. Forced streamwise oscillations of a circular cylinder: locked-on modes and resulting fluid forces. *Journal of Fluids and Structures* **23**(5), 681–701. DOI: 10.1016/j.jfluidstructs.2006.11.001.

[34] Mureithi, N., Huynh, K., Rodriguez, M., and Pham, A., 2010. A simple low order model of forced Karman wake. *International Journal of Mechanical Sciences* **52**(11), 1522–1534. DOI: 10.1016/j.ijmecsci.2010.06.012.

[35] Tanida, Y., Okajima, A., and Watanabe, Y., 1973. Stability of a circular cylinder oscillating in uniform flow or in a wake. *Journal of Fluid Mechanics* **61**(4), 769–784. DOI: 10.1017/S0022112073000935.

[36] Konstantinidis, E. and Bouris, D., 2017. Drag and inertia coefficients for a circular cylinder in steady plus low-amplitude oscillatory flows. *Applied Ocean Research* **65**, 219–228. DOI: 10.1016/j.apor.2017.04.010.

[37] Kim, K.-H. and Choi, J.-I., 2019. Lock-in regions of laminar flows over a streamwise oscillating circular cylinder. *Journal of Fluid Mechanics* **858**, 315–351. DOI: 10.1017/jfm.2018.787.

[38] Mittal, S. and Kumar, V., 1999. Finite element study of vortex-induced cross-flow and in-line oscillations of a circular cylinder at low Reynolds numbers. *International Journal for Numerical Methods in Fluids* **31**, 1087–1120. DOI: 10.1002/(SICI)1097-0363(19991215)31:7<1087::AID-FLD911>3.3.CO;2-3.

[39] Williamson, C. and Govardhan, R., 2004. Vortex-induced vibration. *Annual Review of Fluid Mechanics* **36**, 413–455. DOI: 10.1146/annurev.fluid.36.050802.122128.

[40] Blevins, R. and Coughran, C., 2009. Experimental investigation of vortex-induced vibration in one and two dimensions with variable mass, damping, and Reynolds number. *Journal of Fluids Engineering* **131**, 101202 (7 pages). DOI: 10.1115/1.3222904.

[41] Dahl, J. M., Hover, F. S., Triantafyllou, M. S., and Oakley, O. H., 2010. Dual resonance in vortex-induced vibrations at subcritical and supercritical Reynolds numbers. *Journal of Fluid Mechanics* **643**, 395–424. DOI: 10.1017/S0022112009992060.

[42] Kheirkhah, S., Yarusevych, S., and Narasimhan, S., 2012. Orbiting response in vortex-induced vibrations of a two-degree-of-freedom pivoted circular cylinder. *Journal of Fluids and Structures* **28**, 343–358. DOI: 10.1016/j.jfluidstructs.2011.08.014.

[43] Tu, J., Zhou, D., Bao, Y., Fang, C., Zhang, K., Li, C., and Han, Z., 2014. Flow-induced vibration on a circular cylinder in planar shear flow. *Computers and Fluids* **105**, 138–154. DOI: 10.1016/j.compfluid.2014.08.007.

[44] Gsell, S., Bourguet, R., and Braza, M., 2017. Vortex-induced vibrations of a cylinder in planar shear flow. *Journal of Fluid Mechanics* **825**, 353–384. DOI: 10.1017/jfm.2017.386.

[45] Jeon, D. and Gharib, M., 2001. On circular cylinders undergoing two-degree-of-freedom forced motions. *Journal of Fluids and Structures* **15**(3-4), 533–541. DOI: 10.1006/jfls.2000.0365.

[46] Baranyi, L., 2012. Simulation of a low-Reynolds number flow around a cylinder following a figure-8-path. *International Review of Applied Sciences and Engineering* **3**, 133–146. DOI: 10.1556/IRASE.3.2012.2.7.

[47] Peppa, S., Kaiksis, L., and Triantafyllou, G., 2016. Hydrodynamic forces and flow structures in flow past a cylinder forced to vibrate transversely and inline to a steady flow. *Journal of Offshore Mechanics and Arctic Engineering* **138**(1), Paper No: OMAE-14–1134. DOI: 10.1115/1.4032031.

[48] Stansby, P. and Rainey, R., 2001. A CFD study of the dynamic response of a rotating cylinder in a current. *Journal of Fluids and Structures* **15**(3-4), 513–521. DOI: 10.1006/jfls.2000.0357.

[49] Didier, E. and Borges, A., 2007. Numerical predictions of low Reynolds number flow over an oscillating circular cylinder. *Journal of Computational and Applied Mechanics* **8**(1), 39–55.

[50] Baranyi, L., 2008. Numerical simulation of flow around an orbiting cylinder at different ellipticity values. *Journal of Fluids and Structures* **24**(6), 883–906. DOI: 10.1016/j.jfluidstructs.2007.12.006.

[51] Bishop, R. and Hassan, A., 1964. The lift and drag forces on a circular cylinder oscillating in a flowing fluid. *Proc. Royal Society of London, Series A.* **277**(1368), 51–75. DOI: 10.1098/rspa.1964.0005.

[52] Bearman, P., 1984. Vortex shedding from oscillating bluff bodies. *Annual Review of Fluid Mechanics* **16**, 195–222. DOI: 10.1146/annurev.fl.16.010184.001211.

[53] Bearman, P., 2011. Circular cylinder wakes and vortex-induced vibrations. *Journal of Fluids and Structures* **27**(5-6), 648–658. DOI: 10.1016/j.jfluidstructs.2011.03.021.

[54] Sarpkaya, T., 1995. Hydrodynamic damping, flow-induced oscillations, and biharmonic response. *Journal of Offshore Mechanics and Arctic Engineering* **117**(4), 232–238. DOI: 10.1115/1.2827228.

[55] Sarpkaya, T., 2004. A critical review of the intrinsic nature of the vortex-induced vibrations. *Journal of Fluids and Structures* **19**(4), 389–447. DOI: 10.1016/j.jfluidstructs.2004.02.005.

[56] Blevins, R. Flow-Induced Vibration. Van Nostrand Reinhold Co., Inc., New York, 1990.

[57] Feng, C. The measurement of vortex induced effects in flow past stationary and oscillating circular and D-section cylinders. MA thesis. University of British Columbia, 1968. DOI: 10.14288/1.0104049.

[58] Brika, D. and Laneville, A., 1993. Vortex-induced vibration of a long flexible circular cylinder. *Journal of Fluid Mechanics* **250**, 481–508. DOI: 10.1017/S0022112093001533.

[59] Khalak, A. and Williamson, C., 1999. Motions, forces and mode transitions in vortex-induced vibrations at low mass-damping. *Journal of Fluids and Structures* **13**(7-8), 813–851. DOI: 10.1006/jfls.1999.0236.

[60] Govardhan, R. and Williamson, C., 2000. Modes of vortex formation and frequency response for a freely-vibrating cylinder. *Journal of Fluid Mechanics* **420**, 85–110. DOI: 10.1017/S0022112000001233.

[61] Lighthill, J., 1986. Fundamentals concerning wave loading on offshore structures. *Journal of Fluid Mechanics* **173**, 667–681. DOI: 10.1017/S0022112086001313.

[62] Klamo, J., Leonard, A., and Roshko, A., 2006. The effect of damping on the amplitude and frequency response of a freely vibrating cylinder in cross-flow. *Journal of Fluids and Structures* **22**(6-7), 845–856. DOI: 10.1016/j.jfluidstructs.2006.04.009.

[63] Soti, A., Zhao, J., Thompson, M., Sheridan, J., and Bhardwaj, R., 2018. Damping effects on vortex-induced vibration of a circular cylinder and implications for power extraction. *Journal of Fluids and Structures* **81**, 289–308. DOI: 10.1016/j.jfluidstructs.2018.04.013.

[64] Lee, J. H. and Bernitsas, M. M., 2011. High-damping, high-Reynolds VIV tests for energy harnessing using the VIVACE converter. *Ocean Engineering* **38**(16), 1697–1712. DOI: 10.1016/j.oceaneng.2011.06.007.

[65] Govardhan, R. and Williamson, C., 2006. Defining the 'modified Griffin plot' in vortex-induced vibration: revealing the effect of Reynolds number using controlled damping. *Journal of Fluid Mechanics* **561**, 147–180. DOI: 10.1017/S0022112006000310.

[66] Navrose and Mittal, S., 2017. A new regime of multiple states in free vibration of a cylinder at low Re. *Journal of Fluids and Structures* **68**, 310–321. DOI: 10.1016/j.jfluidstructs.2016.11.003.

[67] Anagnostopoulos, P. and Bearman, P., 1992. Response characteristics of a vortex-excited cylinder at low Reynolds numbers. *Journal of Fluids and Structures* **6**, 39–50. DOI: 10.1016/0889-9746(92)90054-7.

[68] Leontini, J., Thompson, M., and Hourigan, K., 2006. The beginning of branching behavior of vortex-induced vibration during two-dimensional flow. *Journal of Fluids and Structures* **22**(6-7), 857–864. DOI: 10.1016/j.jfluidstructs.2006.04.003.

[69] Willden, R. and Graham, J., 2006. Three distinct response regimes for transverse vortex-induced vibrations of circular cylinders at low Reynolds numbers. *Journal of Fluids and Structures* **22**(6-7), 885–895. DOI: 10.1016/j.jfluidstructs.2006.04.005.

[70] Bahmani, M. and Akbari, H., 2010. Effects of mass and damping ratios on VIV of a circular cylinder. *Ocean Engineering* **37**, 511–519. DOI: 10.1016/j.oceaneng.2010.01.004.

[71] Evangelinos, C. and Karniadakis, G. E., 1999. Dynamics and flow structures in the turbulent wake of rigid and flexible cylinders subject to vortex-induced vibrations. *Journal of Fluid Mechanics* **400**, 91–124. DOI: 10.1017/S0022112099006606.

[72] Singh, S. and Mittal, S., 2005. Vortex-induced oscillations at low Reynolds numbers: hysteresis and vortex-shedding modes. *Journal of Fluids and Structures* **20**(8), 1085–1104. DOI: 10.1016/j.jfluidstructs.2005.05.011.

[73] King, R., 1977. A review of vortex shedding research and its application. *Ocean Engineering* **4**(3), 141–171. DOI: https://doi.org/10.1016/0029-8018(77)90002-6.

[74] Naudascher, E., 1987. Flow-induced streamwise vibrations of structures. *Journal of Fluids and Structures* **1**(3), 265–298. DOI: https://doi.org/10.1016/0889-9746(87)90243-X.

[75] Aguirre, J. Flow-induced in-line vibrations of a circular cylinder. PhD dissertation. Imperial College of Science and Technology, 1977.

[76] Okajima, A., Nakamura, A., Kosugi, T., Uchida, H., and Tamaki, R., 2004. Flow-induced in-line oscillation of a circular cylinder. *European Journal of Mechanics – B/Fluids* **23**(1), 115–125. DOI: 10.1016/j.euromechflu.2003.09.009.

[77] Cagney, N. and Balabani, S., 2013. Wake modes of a cylinder undergoing free streamwise vortex-induced vibrations. *Journal of Fluids and Structures* **38**, 127–145. DOI: 10.1016/j.jfluidstructs.2012.12.004.

[78] Gurian, T., Currier, T., and Modarres-Sadeghi, Y., 2019. Flow force measurements and the wake transition in purely inline vortex-induced vibration of a circular cylinder. *Physical Review Fluids* **4**(3), 034701 (17 pages). DOI: 10.1103/PhysRevFluids.4.034701.

[79] Bourguet, R. and Lo Jacono, D., 2015. In-line fow-induced vibrations of a rotating cylinder. *Journal of Fluid Mechanics* **781**, 127–165. DOI: 10.1017/jfm.2015.477.

[80] Moe, G. and Wu, Z.-J., 1990. The lift force on a cylinder vibrating in a current. *Journal of Offshore Mechanics and Arctic Engineering* **112**(4), 297–303. DOI: 10.1115/1.2919870.

[81] Dahl, J., Hover, F., and Triantafyllou, M., 2006. Two-degree-of-freedom vortex-induced vibrations using a force assisted apparatus. *Journal of Fluids and Structures* **22**(6-7), 807–818. DOI: 10.1016/j.jfluidstructs.2006.04.019.

[82] Dahl, J., Hover, F., Triantafyllou, M., Dong, S., and Karniadakis, G., 2007. Resonant vibrations of bluff bodies cause multivortex shedding and high frequency forces. *Physical Review Letters* **99**, 144503 (4 pages). DOI: 10.1103/PhysRevLett.99.144503.

[83] Bao, Y., Huang, C., Zhou, D., Tu, J., and Han, Z., 2012. Two-degree-of-freedom flow-induced vibrations on isolated and tandem cylinders with varying natural frequency ratios. *Journal of Fluids and Structures* **35**, 50–75. DOI: 10.1016/j.jfluidstructs.2012.08.002.

[84] Wang, E., Xiao, Q., and Incecik, A., 2017. Three-dimensional numerical simulation of two-degree-of-freedom VIV of a circular cylinder with varying natural frequency ratios at $Re = 500$. *Journal of Fluids and Structures* **73**, 162–182. DOI: 10.1016/j.jfluidstructs.2017.06.001.

[85] Jauvtis, N. and Williamson, C. H. K., 2004. The effect of two degrees of freedom on vortex-induced vibration at low mass and damping. *Journal of Fluid Mechanics* **509**, 23–62. DOI: 10.1017/S0022112004008778.

[86] Sanchis, A., 2009. Two degrees of freedom vortex-induced vibrations of a rigid circular cylinder with varying natural frequencies in the x and y directions. In: *Proc. ASME 2009 28th International Conference on Ocean, Offshore and Arctic Engineering*. pp. 889–894.

[87] Prasanth, T., Behara, S., Singh, S., Kumar, R., and Mittal, S., 2006. Effect of blockage on vortex-induced vibrations at low Reynolds numbers. *Journal of Fluids and Structures* **22**(6-7), 865–876. DOI: 10.1016/j.jfluidstructs.2006.04.011.

[88] Prasanth, T. and Mittal, S., 2008. Vortex-induced vibrations of a circular cylinder at low Reynolds numbers. *Journal of Fluid Mechanics* **594**, 463–491. DOI: 10.1017/S0022112007009202.

[89] Mittal, S. and Singh, S., 2005. Vortex-induced vibrations at subcritical Re. *Journal of Fluid Mechanics* **534**, 185–194. DOI: 10.1017/S0022112005004635.

[90] Srinil, N., Zanganeh, H., and Day, A., 2013. Two-degree-of-freedom VIV of circular cylinder with variable natural frequency ratio: experimental and numerical investigations. *Ocean Engineering* **73**, 179–194. DOI: 10.1016/j.oceaneng.2013.07.024.

[91] Kang, Z., Ni, W., and Sun, L., 2016. An experimental investigation of two-degree-of-freedom VIV trajectories of a cylinder at different scales of natural frequency ratios. *Ocean Engineering* **126**, 187–202. DOI: 10.1016/j.oceaneng.2016.08.020.

[92] Oviedo-Tolentino, F., Pérez-Gutiérrez, F., Romero-Méndez, R., and Hernández-Guerrero, A., 2014. Vortex-induced vibration of a bottom fixed flexible circular beam. *Ocean Engineering* **88**, 463–471. DOI: 10.1016/j.oceaneng.2014.07.012.

[93] Marble, E., Morton, C., and Yarusevych, S., 2018. Vortex dynamics in the wake of a pivoted cylinder undergoing vortex-induced vibrations with elliptic trajectories. *Experiments in Fluids* **59**, 78 (16 pages). DOI: 10.1007/s00348-018-2530-3.

[94] Prasanth, T. and Mittal, S., 2009. Vortex-induced vibration of two circular cylinders at low Reynolds number. *Journal of Fluids and Structures* **25**, 731–741. DOI: 10.1016/j.jfluidstructs.2008.12.002.

[95] Baranyi, L. Investigation of low Reynolds number flow around a moving cylinder (in Hungarian). Habilitation thesis. University of Miskolc, 2007.

[96] Harlow, F. and Welch, J., 1965. Numerical calculation of time-dependent viscous incompressible flow of fluid with free surface. *Physics of Fluids* **8**(12), 2182–2189. DOI: 10.1063/1.1761178.

[97] Kawamura, T., Takami, H., and Kuwahara, K., 1986. Computation of high Reynolds number flow around a circular cylinder with surface roughness. *Fluid Dynamics Research* **1**(2), 145–162. DOI: 10.1016/0169-5983(86)90014-6.

[98] He, T. and Zhang, K., 2017. An overview of the combined interface boundary condition method for fluid-structure interaction. *Archives of Computational Methods in Engineering* **24**(4), 891–934. DOI: 10.1007/s11831-016-9193-0.

[99] Strogatz, S. Nonlinear Dynamics and Chaos: with Applications to Physics, Biology, Chemistry, and Engineering. Westview Press, 1994.

[100] Konstantinidis, E. and Liang, C., 2011. Dynamic response of a turbulent cylinder wake to sinusoidal inflow perturbations across the vortex lock-on range. *Physics of Fluids* **23**(7), 075102. DOI: 10.1063/1.3592330.

[101] Konstantinidis, E., Balabani, S., and Yianneskis, M., 2005. The timing of vortex shedding in a cylinder wake imposed by periodic inflow perturbations. *Journal of Fluid Mechanics* **543**, 45–55. DOI: 10.1017/S0022112005006786.

[102] Konstantinidis, E., Zhao, J., Leontini, J., Lo Jacono, D., and Sheridan, J., 2019. Excitation and Damping Fluid Forces on a Cylinder Undergoing Vortex-Induced Vibration. *Frontiers in Physics* **7**, 185 (10pages). DOI: 10.3389/fphy.2019.00185.

[103] Pikovsky, A., Rosenblum, M., and Kurths, J. Synchronization: A Universal Concept in Nonlinear Sciences. Cambridge University Press, 2001.

[104] Konstantinidis, E., Zhao, J., Lo Jacono, D., Leontini, J., and Sheridan, J., 2019. Phase dynamics of effective drag and lift in vortex-induced vibration at low mass-damping. arxiv:1906.07375.

[105] Prasanth, T., Premchandran, V., and Mittal, S., 2011. Hysteresis in vortex-induced vibrations: critical blockage and effect of m^*. *Journal of Fluid Mechanics* **671**, 207–225. DOI: 10.1017/S0022112010005537.

[106] Morse, T. and Williamson, C., 2009. Prediction of vortex-induced vibration response by employing controlled motion. *Journal of Fluid Mechanics* **634**, 5–39. DOI: 10.1017/S0022112009990516.

[107] Khalak, A. and Williamson, C., 1997. Fluid forces and dynamics of a hydroelastic structure with very low mass and damping. *Journal of Fluids and Structures* **11**, 973–982. DOI: 10.1006/jfls.1997.0110.

Appendix A

Evaluation of CFD data

The data sets obtained from the CFD computations (e.g. the cylinder displacement or the aerodynamic force coefficients) are mostly time-varying signals, which include a few million elements. For this reason, the proper evaluation of these data sets are required. The evaluation process covers the calculation of the time-mean and root-mean-square values, the frequencies of the signals (see Appendix A.1) and the phase differences (or phase angles) between two distinct signals (Appendix A.2).

A.1 Statistical properties of periodic signals

Figure A.1a shows the time history of the dimensionless transverse cylinder displacement. In this test case the cylinder is allowed to move only in the transverse direction, and the following parameter combination is used: Re $= 300$, $m^* = 10$, $\zeta = 0\%$ and $U^* = 4.9$. It can be seen in Fig. A.1a that the body is initially at rest, corresponding to the initial conditions [see Eq. (2.20)]. In the approximate non-dimensional time interval of $0 < t < 150$ the amplitude of cylinder vibration increases, beyond the transitional domain the body oscillates with a constant amplitude value. In order to get the most accurate statistical parameters [the root-mean-square (rms), the time-mean and the frequency values], the transitional part of the signal has to be omitted. In this study the statistical quantities are calculated based on the last N_c periods of cylinder oscillation, which takes place in the time domain of $t_{start} < t < t_{finish}$. The root-mean-square and the time-mean values are defined as follows:

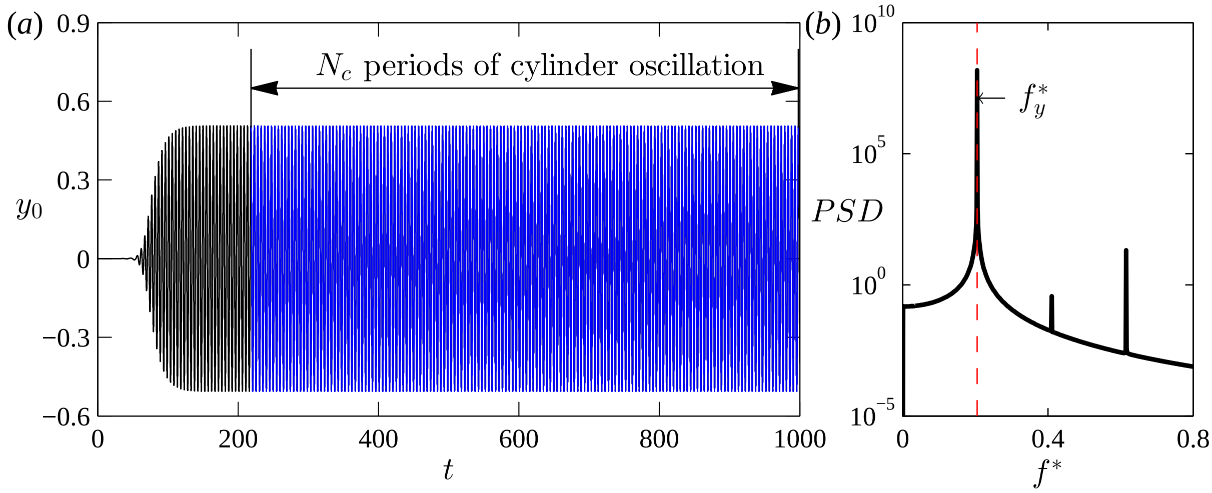

Figure A.1: The time history (a) and the frequency spectra of the cylinder displacement for Re $= 300$, $m^* = 10$, $\zeta = 0\%$ and $U^* = 4.9$

$$y_{0'} = \sqrt{\frac{1}{n-1}\sum_{i=1}^{n}(y_{0,i}-\overline{y}_0)^2}, \quad \text{(A.1)}$$

$$\overline{y}_0 = \frac{1}{n}\sum_{i=1}^{n} y_{0,i}. \quad \text{(A.2)}$$

Here $n = (t_{finish} - t_{start})/\Delta t$, where Δt is the dimensionless time step and $y_{0,i}$ is the i^{th} element of the data set.

The Fast Fourier Transform (FFT) algorithm is used to represent the signal (e.g. displacement(s) or force coefficient(s)) in the frequency domain. Figure A.1b shows the frequency spectrum of the cylinder displacement, i.e. the Power Spectral Density PSD against the non-dimensional frequency f^*. In this test case the vertical axes are shown in a logarithmic scale. However, in Chapters 5 and 6 the normalized spectrum of the signal is also used, which means that the Power Spectral Density is normalized by the maximum PSD value in the spectrum. In these cases the vertical axis is scaled linearly. The frequency of the signal (f_y^* for y_0) is considered to be the frequency value belonging to the highest intensity peak in the spectra, which is denoted by a red dashed line in Fig. A.1b. Note that although the calculation of these statistical parameters are shown here for the cylinder displacement, the methodologies are valid for other quantities, for example for x_0, C_x, C_y, C_V, etc..

A.2 Determination of phase difference

In this study the phase difference (or phase angle) of a force coefficient (in either streamwise or transverse direction) relative to the cylinder displacement in the corresponding direction is frequently computed. In this section two distinct methods are shown to obtain this phase difference value.

A.2.1 Harmonic signals

In case the fluid force coefficient and the cylinder displacement are periodic signals, the phase difference value can be easily calculated. This condition satisfies in streamwise-only vortex-induced vibrations (see the results in Chapter 5) for all the investigated cases; thus the method is introduced via the computation of phase difference between streamwise fluid force coefficient $C_x(t)$ and streamwise cylinder displacement $x_0(t)$.

Let us assume that the streamwise fluid force coefficient can be represented as:

$$C_x(t) \cong \sum_{i=1}^{N} C_x^i \cos(2\pi i f_x^* t + \Phi_x^i), \quad \text{(A.3)}$$

where C_x^i is the magnitude of the i^{th} harmonic component of the streamwise fluid force coefficent, f_x^* is the dimensionless vibration frequency and Φ_x^i is the phase difference of the i^{th} harmonic component relative to the cylinder displacement. Multiplying $C_x(t)$ by $\sin 2\pi f_x^* t$, and integrating it over one period of cylinder oscillation $T = 1/f_x^*$, the following simple expression can be obtained:

$$\begin{aligned} I_1 = \int_0^T C_x(t)\sin 2\pi f_x^* t\mathrm{d}t = \int_0^T \left[\sum_{i=1}^{N} C_x^i \cos(2\pi i f_x^* t + \Phi_x^i)\right] \sin 2\pi f_x^* t\mathrm{d}t = \\ = -\frac{1}{2} f_x^{*-1} C_x^1 \sin \Phi_x^1. \end{aligned} \quad \text{(A.4)}$$

Although Φ_x^1 is an unknown quantity, I_1 can be calculated by integrating $\int_0^T C_x(t)\sin 2\pi f_x^* t\mathrm{d}t$ numerically using the trapezoidal rule or some other numerical quadrature. Besides, multiplying $C_x(t)$ by $\cos 2\pi f_x^* t$ and integrating the expression over one oscillation cycle, the following formula can be obtained:

$$I_2 = \int_0^T C_x(t)\cos 2\pi f_x^* t\mathrm{d}t = \int_0^T \left[\sum_{i=1}^{N} C_x^i \cos(2\pi i f_x^* t + \Phi_x^i)\right]\cos 2\pi f_x^* t\mathrm{d}t = \\ = \frac{1}{2} f_x^{*-1} C_x^1 \cos\Phi_x^1. \tag{A.5}$$

Similarly to Eq. (A.4), I_2 can be solved numerically. Dividing Eq. (A.4) by Eq. (A.5), the following formula can be obtained for the phase difference value:

$$\Phi_x = \Phi_x^1 = \tan^{-1}\left(-\frac{I_1}{I_2}\right). \tag{A.6}$$

A.2.2 Application of Hilbert transform

In case Eq. (A.3) does not hold true, the calculation methodology of the phase difference, detailed in Appendix A.2.1 is not applicable. In these cases the analytical signal approach based on Hilbert transform can be used [103, 104]. This methodology is applied in Chapter 4 to compute the phase difference between the streamwise fluid force and the streamwise cylinder displacement, and in Chapter 6 to obtain the phase difference of the transverse fluid force and vortex force relative to the transverse cylinder displacement.

In order to introduce this approach, let us consider a vortex-induced vibration problem, where the cylinder is restricted to oscillate only in transverse direction. The analytical signal of the cylinder displacement $y_0(t)$ can be expressed as [104]:

$$y_{0a}(t) = y_0(t) + \mathrm{i}y_{0h}(t) = A_{y_0}(t)e^{i\Phi_{y_0}(t)}, \tag{A.7}$$

where i is the imaginary unit, $y_{0h}(t)$ is the Hilbert transform of $y_0(t)$, and $A_{y_0}(t)$ is the time-dependent amplitude of the signal and $\Phi_{y_0}(t)$ is the time-varying phase of the cylinder

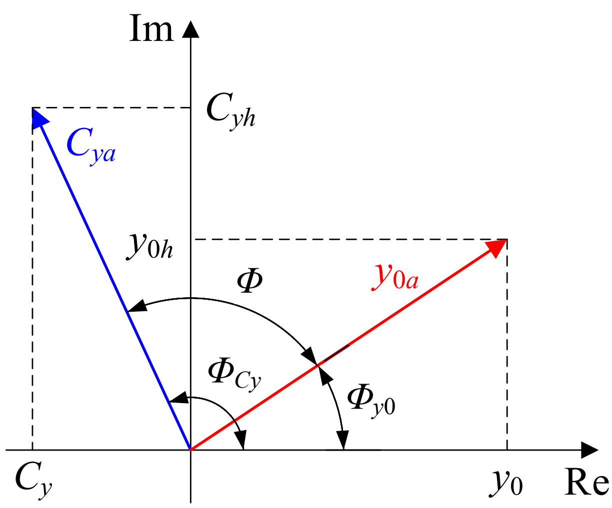

Figure A.2: The arrangement of the analytical signals y_{0a} and C_{ya} at an arbitrary time instant. Here Im and Re denote the imaginary and the real axes, respectively displacement:

$$A_{y_0}(t) = \sqrt{y_0(t)^2 + y_{0h}(t)^2}, \qquad \Phi_{y_0}(t) = \tan^{-1}\left[\frac{y_{0h}(t)}{y_0(t)}\right]. \qquad (A.8a, b)$$

Figure A.2 shows the analytical signals of the cylinder displacement and the transverse fluid force y_{0a} and C_{ya} on the complex number plane at an arbitrary time instant. Similarly to Φ_{y_0}, the time-varying phase of the transverse fluid force can be determined as

$$\Phi_{C_y}(t) = \tan^{-1}\left[\frac{C_{yh}(t)}{C_y(t)}\right], \qquad (A.10)$$

where $C_{yh}(t)$ is the Hilbert transform of the transverse fluid force coefficient. As can be seen in Fig. A.2, the phase difference of the transverse fluid force relative to the cylinder displacement, i.e. the transverse phase, can be obtained as

$$\Phi(t) = \Phi_{C_y}(t) - \Phi_{y_0}(t). \qquad (A.11)$$

It should be noted that Pikovsky et al. [103] defined the phase difference value as the difference of the displacement with respect to the force. For the sake of comparison, we applied Eq. A.11 to obtain the phase angle value. The same methodology can be used to obtain the vortex phase, i.e. the phase difference of the vortex force relative to the cylinder displacement:

$$\Phi_V(t) = \Phi_{C_V}(t) - \Phi_{y_0}(t), \qquad (A.12)$$

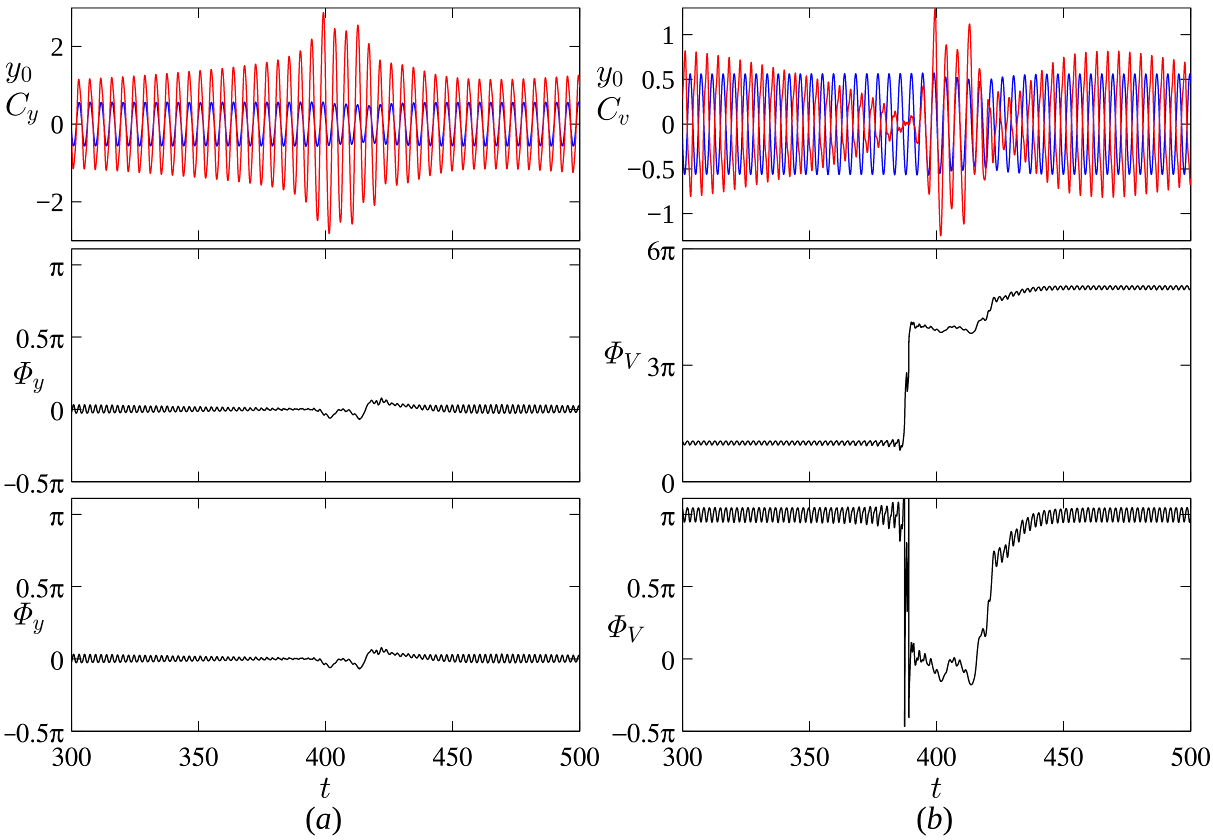

Figure A.3: Time histories of y_0, C_y and C_V (top row), and the time-varying unwrapped (middle row) and wrapped (bottom row) transverse and vortex phases for transverse-only VIV. In the top row the displacement and force coefficient curves are shown in blue and red, respectively. The following computational parameters are used: $\mathrm{Re} = 300$, $m^* = 10$, $\zeta = 0\%$ and $U^* = 4.2$

where $\Phi_{C_V}(t)$ is the phase of the vortex force coefficient.

When the two investigated signals have the same frequency values (i.e. the signals are synchronized), the phase difference between them is constant in time. However, there are some special cases, when the frequencies of the signals are different, which causes increasing/decreasing effects in the corresponding phase difference (see Chapter 6). In terms of time-averaged phase differences, the phase angle value between 0° and 360° is meaningful. In order to calculate an accurate time-mean value, the phase difference signal has to be *wrapped* in a 2π-long interval; in this dissertation between $-\pi/2$ and $3\pi/2$.

Figure A.3 helps to understand the difference between unwrapped and wrapped phase angles. Figure A.3a shows the time histories of y_0 and C_y (top row), the time-varying transverse phase Φ_y as an unwrapped signal (middle row), and the time history of Φ_y wrapped between $-\pi/2$ and $3\pi/2$ (bottom row). The structures of Figs. A.3a and A.3b are similar, but in Fig. A.3b the time histories of C_V and Φ_V are shown instead of the C_y and Φ_y. It can be seen that, since the frequencies of the cylinder displacement and the transverse fluid force are identical, the unwrapped and wrapped transverse phases show the same characteristics (Fig. A.3a). In contrast, a small detuning[1] occurs between C_V and y_0, hence, the unwrapped vortex phase shows an increasing effect (Fig. A.3b). As mentioned earlier, to obtain the time-averaged vortex phase, Φ_V has to be wrapped between $-\pi/2$ and $3\pi/2$, which is show in the bottom row of Fig. A.3b.

[1]The difference between the frequencies of force coefficient and the cylinder displacement